DISSERTATION

A COMPLEX OF INTERACTIONS IN RARE-EARTH BASED QUANTUM HONEYCOMB MAGNETS

Submitted by

Andrew Treglia

Department of Physics

In partial fulfillment of the requirements

For the Degree of Doctor of Philosophy

Colorado State University

Fort Collins, Colorado

Spring 2025

Doctoral Committee:

Advisor: Martin Gelfand
Co-Advisor: James Neilson

Hua Chen
Amy Prieto

ABSTRACT

A COMPLEX OF INTERACTIONS IN RARE-EARTH BASED
QUANTUM HONEYCOMB MAGNETS

Quantum spin liquids (QSLs) represent an exotic state of matter characterized by long-range quantum entanglement and fractionalized excitations. Although predicted theoretically by models such as the Kitaev honeycomb model, experimentally verifying these states in real materials remains a significant challenge in condensed matter physics. This dissertation investigates the magnetic interactions in rare-earth honeycomb materials as potential candidates for realizing QSLs, with a focus on the exchange mechanisms governing their magnetic properties.

Through a combination of magnetization, heat capacity, and inelastic neutron scattering experiments, this work systematically explores the magnetic phase behavior of $Yb_2Si_2O_7$ and $ErCl_3$, two rare-earth compounds with effective spin-1/2 degrees of freedom on geometrically frustrated lattices. The first part of this dissertation examines $Yb_2Si_2O_7$, which exhibits field-induced quantum phase transitions. Magnetization measurements reveal strong anisotropy consistent with spin-orbit coupled physics, while neutron diffraction and inelastic spectroscopy provide insight into the formation of a Bose-Einstein condensate (BEC) of triplons. However, the absence of staggered magnetization in field-dependent neutron scattering data challenges prior theoretical models and suggests a more complex underlying exchange mechanism.

The second part of this work focuses on $ErCl_3$, a material whose honeycomb lattice structure and strong single-ion anisotropy make it a promising candidate for realizing bond-dependent exchange interactions. Single-crystal neutron scattering experiments, performed in a controlled air-free environment, reveal deviations from conventional isotropic exchange,

indicating the presence of anisotropic interactions. A systematic analysis of spin wave excitations enables the extraction of exchange parameters, offering experimental constraints for theoretical models describing Kitaev-like interactions in this system.

By integrating experimental results with theoretical models, this dissertation advances the understanding of rare-earth-based quantum magnets. The findings underscore the importance of strong spin-orbit coupling and crystal field effects in stabilizing anisotropic exchange, while highlighting key challenges in the experimental verification of QSL behavior. These results provide critical insights for the ongoing search for materials that host quantum spin liquid states and topological excitations, paving the way for future investigations into the realization of quantum matter in real materials.

ACKNOWLEDGEMENTS

The completion of my PhD would not have been possible if it weren't for many good friends, family, colleagues, and mentors along the way. I would like to begin by expressing my deepest gratitude to my parents, Ed and Melinda Treglia, whose immeasurable support over the past 13 years of school has been the foundation of my journey. From childhood, they instilled in me the belief that I could achieve anything if I put my mind to it. Through their unwavering dedication and hard work, they ensured that I had every opportunity to succeed and pursue a life where I can truly live. For that, I will be forever grateful, and I can only hope to provide the same encouragement and support to my own children one day. To my siblings—Wes, Emily, and Tonyyy—I thank you for being part of that foundation. Whether through support or distraction, you've been a constant presence that I truly appreciate. I'd like to thank my grandparents, Rex and Karen Hight, your hard work, support, and encouragement have created a foundation of love and strength that will carry through many generations. To my aunts and uncles—Clint, Laura, Julie, Nick, John, Linda, Bryan, and Jessica—and my cousins—Taylor, Adam, Katie, Stefan, Trent, Lindsey, Aaron, Courtney, Sam, Rachel, Dillon, Cassie, Lexi, Tori, Zach—you've all played a memorable part in shaping me into who I am today. When it comes to shaping who I am, it's my friends who truly fine-tuned my personality—instilling in me a deep appreciation for happiness and adventure. I've been lucky to have many incredible friends over the years, far too many to list here. Though I haven't always been the best at keeping in touch, I deeply value the companionship we share.

I am greatly appreciative of the all the incredible people I've had the chance to work with. In my undergraduate years, my mentor, Minhyea Lee, and her graduate students at the time—Peter Siegfried, Ian Leahy, and Chris Pocs—all taught me so much. You started me on my journey to be a research scientist and endlessly fueled my curiosity. I am deeply

grateful. Of course none of this work would have been possible without the support of the Ross Lab, specifically Gavin Hester, Danielle Yahne, Colin Sarkis, Steffen Säubert, John Ringler, Daniel Shaw, Tim DeLazzer, Andrew Sexton, James Shaddix, and Theo Wecker. Thank you for all the comraderie and great discussions. I'd like to particularly thank Gavin Hester and Danielle Yahne for being an exemplary model of a graduate student and helping me break into the field of neutron scattering. To my cohort friends—Byron, Lane, Evan, Tarkan—you guys have made my time in graduate school so much fun. The party office made the long nights of miserable homework quite memorable and our adventures in the mountains gave me something to look forward to nearly every weekend. I would like to specifically acknowledge my original advisor Kate Ross, whose legendary status brought me here in the first place. You were truly a pleasure to work with, and I've always admired your ability to make even the most complex topics feel simple and intuitive—it speaks volumes about your mastery. I hope you enjoy your new career outside of academia—I have no doubt you'll excel at whatever you do. Of course, I would also like to thank Jamie Neilson, who took me on and made it possible for me to continue my research. Your support has been unwavering, and you exemplify what it means to be a model academic. You and Kate make an incredible team, and I feel truly fortunate to have had both of you as advisors. I would also like to thank the rest of my committee—Marty Gelfand (thank you for taking me on), Hua Chen, and Amy Prieto.

I also acknowledge all the individuals and organizations who contributed to this research. This work was supported by the National Science Foundation under Agreement Nos. DMR-1611217 and DMR-2005143. I would like to thank the Analytical Resources Core (ARC) at Colorado State University for instrument access and training—particularly Indrani Bhowmick. I am also grateful to Jeff Breitschopf for his expertise and invaluable assistance in the Colorado State University Department of Physics Machine Shop. Special thanks to Adam Aczel for his assistance with our elastic neutron scattering experiment on $Yb_2Si_2O_7$ using the HB-1A instrument at Oak Ridge National Laboratory, and to Daniel

Mazzone for his support during the inelastic neutron scattering experiments on $ErCl_3$ using the CAMEA instrument at Paul Scherrer Institute. I also extend my gratitude to the technical support team at Quantum Design for their assistance in rebuilding and repairing our MPMS and PPMS systems. Additionally, I sincerely thank the administrative teams in both the Physics and Chemistry Departments at Colorado State University for their support.

Finally, I would like to thank my girlfriend, Natalie Berko. You've been so supportive throughout this PhD, and I am beyond grateful to come home to you and Mr. Nimbus every night. I look forward to our future together—wherever life takes us, I'm glad I get to share it with you.

DEDICATION

To the simple act of putting one foot in front of the other—it's amazing how far it can take you.

Nobody ever figures out what life is all about, and it doesn't matter. Explore the world. Nearly everything is really interesting if you go into it deeply enough.

$\sim$ *Richard P. Feynman*

TABLE OF CONTENTS

LIST OF TABLES

LIST OF FIGURES

Chapter 1

Introduction

The pursuit of new materials that could serve as platforms for topological quantum computing remains one of the most ambitious goals in modern condensed matter physics. Among the various exotic states of matter that have been proposed as potential candidates, quantum spin liquids stand out due to their intrinsic long-range quantum entanglement and fractionalized excitations. These properties make them ideal for hosting non-Abelian anyons, which could, in principle, be used to perform fault-tolerant quantum computations. While theoretical models, such as the Kitaev model, predict that certain materials with bond-dependent anisotropic interactions could realize this state, experimental verification has remained elusive. This dissertation contributes to the search for quantum spin liquid candidates by investigating the complex interactions present in rare-earth honeycomb magnets, with a particular focus on the exchange mechanisms that govern their magnetic behavior.

The study of quantum magnetism has undergone significant advancements in recent decades, driven by the desire to understand unconventional magnetic states that defy classical descriptions. Rare-earth-based quantum materials have emerged as particularly promising candidates due to their strong spin-orbit coupling, crystal field effects, and bond-dependent anisotropic exchange interactions. These features create the conditions necessary for realizing highly anisotropic magnetic interactions, which in turn stabilize exotic ground states such as quantum spin liquids. Recent studies on rare-earth honeycomb systems, particularly those involving $ErCl_3$ and $Yb_2Si_2O_7$, suggest that these materials may provide a viable platform for exploring such physics. Understanding the fundamental exchange interactions in these materials is critical for determining their suitability as quantum spin liquid candidates

and, more broadly, for uncovering new forms of quantum magnetism.

A key objective of this dissertation is to identify and characterize the dominant exchange interactions in rare-earth honeycomb magnets. By combining neutron scattering, magnetization, and heat capacity measurements, this work explores the role of spin-orbit coupling and crystal field effects in shaping the low-temperature magnetic properties of these systems. A particular focus is given to the search for signatures of spin fractionalization, dynamic correlations, and bond-dependent anisotropic interactions—hallmarks of quantum spin liquid behavior. Additionally, the study investigates how these interactions influence the formation of ordered or disordered magnetic states, providing insights into the underlying mechanisms that drive quantum magnetism in these materials.

This dissertation follows a structured approach, beginning with an extensive background on rare-earth magnetism, including spin-orbit coupling, crystal field effects, and exchange interactions. The theoretical framework surrounding bond-dependent anisotropic exchange is discussed, with emphasis on the Kitaev model and its implications for quantum spin liquids. The subsequent chapters focus on experimental investigations, including the study of $Yb_2Si_2O_7$ as a potential quantum dimer magnet, followed by the synthesis, preparation, and characterization of $ErCl_3$. Experimental methodologies, including neutron scattering and magnetization measurements, are detailed to provide a comprehensive understanding of the physical properties of these materials. The concluding chapters analyze the exchange interactions governing $ErCl_3$ and explore its deviations from conventional magnetic order. These findings contribute to the broader understanding of rare-earth quantum materials and their potential realization of exotic quantum phases.

By combining advanced neutron scattering techniques with thermodynamic and magnetization measurements, this work establishes a detailed understanding of the microscopic interactions governing rare-earth honeycomb materials. The methodologies developed here provide a foundation for future studies on similar quantum materials, guiding the search for novel quantum phases. Ultimately, this research advances the field of quantum magnetism

by elucidating the complex interplay of exchange interactions in rare-earth-based systems, paving the way for further exploration of exotic quantum states and their potential applications in next-generation quantum technologies. While the realization of a practical material for topological quantum computing remains a distant goal, this work contributes to the fundamental understanding necessary to move one step closer to that possibility.

Chapter 2

Background

Long before science provided explanations, humans believed magnets to be magical stones, imbued with mysterious forces that could move iron and guide travelers across vast oceans. This fascination with lodestones, first documented in the 6^{th} century BC, sparked an enduring curiosity that would evolve over millennia. By the 19^{th} century, this wonder transformed into rigorous scientific inquiry, as Faraday and Maxwell uncovered the principles of electromagnetism, revealing that these "magic rocks" were windows into fundamental forces of nature. Today, this journey has led us to the frontier of condensed matter physics, where we seek to uncover exotic quantum states of matter. Chief among these is the elusive Quantum Spin Liquid (QSL), a state where magnetic moments evade conventional order through entanglement and quantum fluctuations—a modern manifestation of the mystery that magnets once inspired.

In modern condensed matter physics, magnetism serves as a cornerstone for studying intricate interactions at the atomic and electronic levels. Among the most intriguing classes of materials are those containing rare-earth elements, whose unique electronic configurations give rise to an extraordinary diversity of magnetic behaviors. This chapter explores the theoretical and experimental underpinnings of the magnetism in a selection of rare-earth-based systems. This chapter establishes the necessary theoretical background to understand the exotic magnetism observed in certain rare-earth-based materials.

We begin by outlining the fundamental principles of rare-earth magnetism, including the role of $4f$ electrons, crystal field effects, and spin-orbit coupling. These ingredients give rise to highly anisotropic interactions that, when combined with geometric frustration, can stabilize

unconventional quantum states such as spin liquids. Building upon these foundations, we examine how bond-dependent exchange interactions emerge in specific lattice geometries, culminating in a discussion of the Kitaev model, a paradigmatic example of a quantum spin liquid.

The second half of this chapter transitions to experimental techniques used to investigate these theoretical models in real materials. The methodologies covered include neutron scattering, heat capacity, and magnetometry, which are essential for probing the presence of bond-dependent anisotropic interactions and fractionalized excitations in quantum magnets. These tools provide a means of distinguishing quantum spin liquids from more conventional magnetic states and guide the search for materials that exhibit these novel behaviors.

By bridging theoretical models with experimental methodologies, this chapter lays the groundwork for the investigations presented in subsequent chapters, where we apply these concepts to specific rare-earth-based materials in pursuit of realizing and characterizing exotic quantum states.

2.1 Rare-earth Magnetism

Rare-earth magnetism arises from the unique electronic structure of rare-earth elements, characterized by partially filled $4f$ orbitals. These orbitals are spatially compact and shielded by the filled $5s$ and $5p$ orbitals, leading to weak overlap with neighboring atoms. This shielding can be quantified through calculations of the radial expectation (squared) value, $\langle r \rangle^2$, which shows that $4f$ orbitals are significantly more localized compared to $3d$ or $5d$ orbitals. Fig. 2.1 illustrates $\langle r \rangle^2$ for different electronic configurations highlights the compactness of the $4f$ orbitals and their limited spatial extent, emphasizing their role in the localized nature of rare-earth magnetism.

This localized nature has profound implications for the magnetic behavior of rare-earth ions, which is governed by localized electronic interactions such as spin-orbit coupling (SOC)

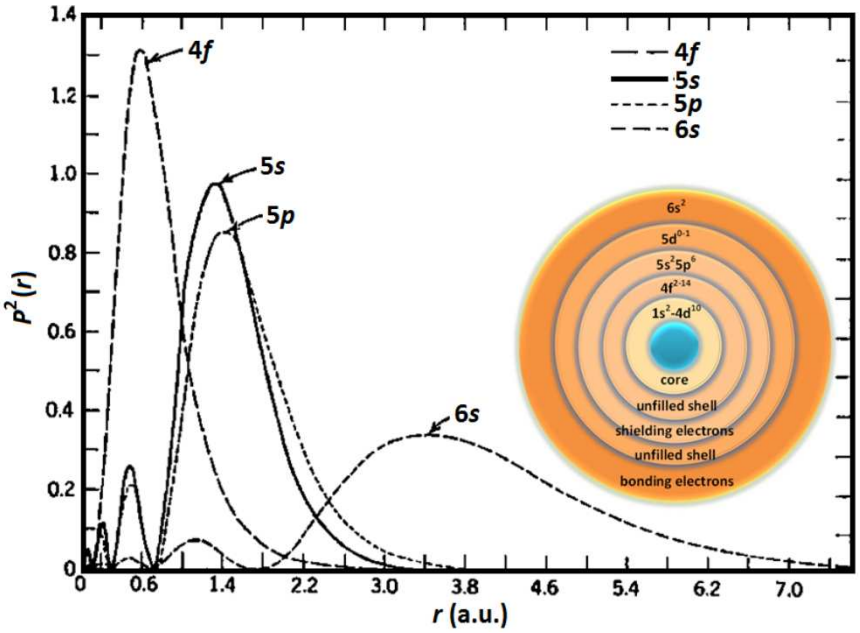

Figure 2.1: Square of the radial wavefunctions for the $4f$, $5s$, $5p$ and $6s$ orbitals of Gd^+, calculated using the Hartree-Fock method (adapted from Refs.[1, 2]). The inset schematic illustrates how the compact $4f$ orbital is spatially shielded by outer orbitals.

and crystal field effects. These interactions dominate over the itinerant mechanisms often seen in transition metals, leading to large magnetic moments determined by Hund's rules. The compactness of $4f$ orbitals also enables rare-earth ions to adopt a nearly universal trivalent oxidation state (R^{3+}), generally achieved by losing two $6s$ electrons and one $4f$ electron. This trivalent oxidation state ensures consistent bonding across different rare-earth ions, making them interchangeable within a given host material. Such versatility is a boon for studying magnetism, as one can systematically substitute different rare-earth ions while maintaining the structural integrity of the material. However, the lanthanide contraction—progressive reduction in atomic radii from La (2.50 Å) to Lu (2.27 Å)—limits this interchangeability in some cases due to changes in lattice strain, which can distort the crystal field environment and alter magnetic interactions—which can be interesting in its own right.

The strong SOC inherent to heavy rare-earth elements couples spin ($\boldsymbol{S}$) and orbital angular momentum ($\boldsymbol{L}$) into a total angular momentum ($\boldsymbol{J}$), yielding well-defined multiplets

that dictate magnetic behavior. In systems with an odd number of electrons, Kramers degeneracy ensures the ground state is at least doubly degenerate [18]. Spin-orbit coupling (SOC) produces degenerate multiplets, which are further split into doubly degenerate states by the crystal electric field (CEF). At temperatures lower than the energy gap between the ground doublet and the first excited doublet—typically tens to hundreds of Kelvin—the system can be effectively described as a spin-$\frac{1}{2}$ system, as only the ground state doublet is thermally populated. This effective spin-$\frac{1}{2}$ description not only captures the low-energy magnetic properties but also simplifies theoretical modeling of these systems. A widely studied example of this behavior is Yb^{3+} ions in $YbMgGaO_4$, where the $4f^{11}$ electrons exhibit a ground state Kramers doublet arising from CEF splitting of the $J = 7/2$ multiplet, with the energy gap to the first excited state of $\Delta \sim 420$K. Thus, for $T \ll \Delta$ where excited doublets are thermally inaccessible, the system can be effectively described as spin-$\frac{1}{2}$.

Interactions between rare-earth ions in a crystal lattice are mediated by superexchange mechanisms, which depend sensitively on lattice geometry and bonding. Combined with spin-orbit coupling (SOC) and crystal field effects, these interactions result in highly anisotropic exchange interactions. Such anisotropy plays a pivotal role in defining the magnetic ground state and the dynamics of excitations, particularly in low-symmetry systems like rare-earth chlorides. A hallmark of rare-earth magnetism is frustration, often arising from competing interactions in geometrically constrained lattices such as honeycomb or triangular geometries. This frustration can suppress conventional magnetic ordering, paving the way for the emergence of exotic quantum states like spin liquids.

The interchangeability of rare-earth ions and their effective spin-$\frac{1}{2}$ descriptions, coupled with their strong SOC and intrinsic anisotropy, make these systems prime candidates for studying fundamental quantum phenomena. By investigating the interplay of SOC, crystal field effects, and exchange interactions, we gain a deeper understanding of the mechanisms driving their complex behavior and their potential for realizing novel quantum states like quantum spin liquids. Rare-earth materials thus serve as a rich platform for exploring the

frontiers of quantum magnetism.

2.1.1 Magnetic interactions

Magnetic interactions in rare-earth systems are governed by the coupling of magnetic moments, which arise from the quantum mechanical properties of electrons, including their spin and orbital angular momentum. In this class of insulators, unpaired electrons primarily interact through two mechanisms: the exchange interaction and the magnetic dipole-dipole interaction. The magnetic dipole-dipole interaction is a long-range force resulting from the magnetic fields generated by the motion of charged particles, where the energy depends on the relative alignment of the magnetic moments and their spatial separation. In contrast, the exchange interaction originates from the quantum mechanical principles of Coulomb repulsion and the Pauli Exclusion Principle (PEP), which collectively dictate the symmetry of the electronic wavefunctions. In non-insulating systems, additional interactions, such as the RKKY interaction mediated by conduction electrons, could play a significant role. However, in the insulating rare-earth systems under consideration, magnetic interactions are primarily governed by effects arising from the localized nature of the magnetic moments, beginning with the long-range magnetic dipole-dipole interaction.

Dipole-Dipole Interaction: Magnetic dipole-dipole interactions in crystalline systems arise from the semi-classical[1] magnetic fields generated by the intrinsic spin of unpaired electrons. For two magnetic dipoles, the interaction energy is described by:

$$E_{dipole-dipole} = \frac{\mu_0}{4\pi} \frac{\boldsymbol{\mu}_i \cdot \boldsymbol{\mu}_j - 3(\boldsymbol{\mu}_i \cdot \hat{\boldsymbol{r}})(\boldsymbol{\mu}_j \cdot \hat{\boldsymbol{r}})}{r^3} \tag{2.1}$$

where $\boldsymbol{\mu}_i$ and $\boldsymbol{\mu}_j$ are the magnetic moments and $\boldsymbol{r}$ is the distance vector from moment i to j, as illustrated in Fig. 2.2a. For a system of N moments, we can naturally expand Eq. 2.1 to the many body Hamiltonian

[1] Although the dipole-dipole interaction originates from classical electromagnetic theory, in rare-earth systems, the magnetic moments are quantum operators, making this interaction fundamentally semi-classical in nature.

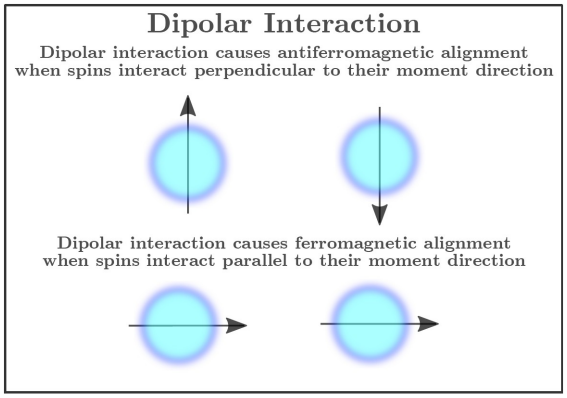

(a)

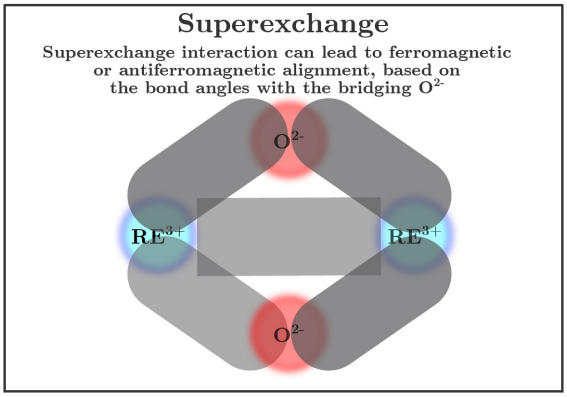

(b)

Figure 2.2: Illustrations of two distinct magnetic interactions [3]. (a) The dipole-dipole interaction, which arises from the magnetic fields produced by localized moments. This interaction is long-ranged and strongly dependent on the relative orientation and distance between dipoles. (b) The superexchange interaction, an indirect exchange mechanism mediated by an intermediate nonmagnetic ion. Superexchange can lead to either ferromagnetic or antiferromagnetic coupling depending on orbital overlap and electronic configuration, and it plays a crucial role in transition metal and rare-earth systems.

$$\mathcal{H}_{dipole-dipole} = \sum_{i<j} \frac{\mu_0}{4\pi} \frac{\boldsymbol{\mu}_i \cdot \boldsymbol{\mu}_j - 3(\boldsymbol{\mu}_i \cdot \hat{\boldsymbol{r}}_{ij})(\boldsymbol{\mu}_j \cdot \hat{\boldsymbol{r}}_{ij})}{r_{ij}^3} \tag{2.2}$$

where $\boldsymbol{\mu}_i$ and $\boldsymbol{\mu}_j$ are the magnetic moment operators of the i-th and j-th spins, r_{ij} is the distance between them, and $\hat{\boldsymbol{r}}_{ij}$ is the unit vector pointing from moment i to moment j.

From the $1/r^3$ dependence, it is evident that this interaction is relatively long-ranged. The magnetic moment operator is related to the angular momentum operators of the system and is expressed as:

$$\boldsymbol{\mu}_i = -g_J \mu_B \hat{\boldsymbol{J}}_i \tag{2.3}$$

where g_J is the Landé g-factor, μ_B is the Bohr magneton (equivalent to $\frac{e\hbar}{2m_e}$), and $\hat{\boldsymbol{J}}_i$ represents the total angular momentum operator for the i-th spin. In rare-earth systems, the compact nature of the $4f$ orbitals shields the magnetic moments, reducing overlap with neighboring electrons. As a result, the dipole-dipole interaction may become significant over long distances, particularly in materials with sparse magnetic ions or extended lattice

structures. While its strength is generally weaker than exchange interactions, it can play an essential role in stabilizing certain magnetic configurations and contributing to collective behaviors such as long-range order or frustration in low-dimensional systems. For rare-earth compounds with low symmetry, the dipole-dipole interaction can also introduce subtle anisotropic effects, influencing the orientation of magnetic moments relative to the crystal lattice. While the dipole-dipole interaction is often the most significant semi-classical magnetic interaction, higher-order multipole terms, such as quadrupole and octopole interactions, can also emerge in systems with localized $4f$ electrons. These higher-order contributions, though generally weaker, introduce additional layers of complexity, influencing anisotropic coupling, field-dependent phenomena, and potentially altering the favored magnetic order under specific conditions. This is exemplified in the recent work by Yahne et al., where dipolar and octupolar contributions in pyrochloric $Ce_2Sn_2O_7$ are shown to be responsible for its All-In-All-Out Néel ground state, as well as its finite-temperature quantum spin ice states [19].

While these magneto-polar interactions provide a foundational understanding of long-range magnetic coupling from a semi-classical perspective, they are often relatively weak compared to the *exchange interactions*, which have a deeper quantum mechanical origin. In rare-earth systems, exchange interactions arise from the interplay of Coulomb repulsion, which sets the energetic scale of the interactions, and the Pauli Exclusion Principle, which imposes symmetry constraints on electronic wavefunctions. These principles collectively govern a broad spectrum of magnetic phenomena, from localized ordering in conventional magnets to exotic states such as quantum spin liquids (QSLs), and arise through mechanisms ranging from direct orbital overlap to indirect mediation by intermediary particles or fields.

To reiterate—at their core, exchange interactions emerge as a consequence of the requirement that electrons, as fermions, must occupy antisymmetric total wavefunctions. This symmetry requirement energetically favors certain spin configurations, leading to magnetic order. To see how these fundamental principles give rise to magnetic ordering, we consider

the archetypal two-electron system. This idealized model consists of two electrons, each primarily localized around a distinct lattice site, such as two adjacent atoms or ions in a crystalline material.

The behavior of this system is governed by the time-independent Schrödinger equation

$$\mathcal{H}\Psi_{total} = E\Psi_{total} \tag{2.4}$$

where $\mathcal{H}$ is the Hamiltonian of the system, Ψ_{total} is the total wavefunction, and E is the total energy. For two electrons, the Hamiltonian can be expressed as

$$\mathcal{H} = -\frac{\hbar^2}{2m_e}(\nabla_1^2 + \nabla_2^2) + \frac{e^2}{|\boldsymbol{r}_1 - \boldsymbol{r}_2|} + V_{en}(\boldsymbol{r}_1, \boldsymbol{r}_2) \tag{2.5}$$

where the first two terms are the kinetic energy of each electron, the third term is the Coulomb repulsion between them, and the last term $V_{en}(\boldsymbol{r}_1, \boldsymbol{r}_2)$ serves as the interaction between the electrons and nuclei/lattice[2]. The total wavefunction for this system can be written as

$$\Psi_{total} = \psi(\boldsymbol{r}_1, \boldsymbol{r}_2)\chi(s_1, s_2) \tag{2.6}$$

where ψ is the spatial component and χ is the spin component. Since the electrons are spin-1/2 particles, we can write their basis states as

$$|\uparrow\uparrow\rangle, |\uparrow\downarrow\rangle, |\downarrow\uparrow\rangle, |\downarrow\downarrow\rangle \tag{2.7}$$

where we can then tabulate the appropriate linear combinations of these states (by solving for the common eigenvectors of the S^2 and S_Z operators) in the $|Sm_S\rangle$ basis with total spin S and spin quantum number m_S [20, 21], as shown in Table 2.1. The PEP requires that the total wavefunction be antisymmetric under particle exchange, i.e.,

[2]It can be noted here that this Hamiltonian does not explicitly depend on the electrons spin s_1 and s_2.

Table 2.1: Spin states of a two-electron system represented in the $|Sm_S\rangle$ basis, with their expansions in the individual spin state basis $|s_1 s_2\rangle$. Each state is identified by its singlet or triplet nature and its symmetry properties.

$\boldsymbol{\|Sm_S\rangle}$	**Spin State**	**Description**
$\|11\rangle$	$\|\uparrow\uparrow\rangle$	Triplet, Symmetric
$\|10\rangle$	$\frac{1}{\sqrt{2}}(\|\uparrow\downarrow\rangle + \|\downarrow\uparrow\rangle)$	Triplet, Symmetric
$\|1\text{-}1\rangle$	$\|\downarrow\downarrow\rangle$	Triplet, Symmetric
$\|00\rangle$	$\frac{1}{\sqrt{2}}(\|\uparrow\downarrow\rangle - \|\downarrow\uparrow\rangle)$	Singlet, Antisymmetric

$$\Psi(\boldsymbol{r}_1, \boldsymbol{r}_2) = -\Psi(\boldsymbol{r}_2, \boldsymbol{r}_1) \tag{2.8}$$

This constraint imposes a symmetry relationship between the spatial and spin wavefunctions: if the spatial wavefunction $\psi(\boldsymbol{r}_1, \boldsymbol{r}_2)$ is symmetric, the spin wavefunction $\chi(s_1, s_2)$ must be antistymmetric (a singlet state). Conversely, if the spatial wavefunction is antisymmetric, the spin wavefunction must be symmetric (a triplet state). From this point, we can already start to see how the spatial arrangement of the two moments can lead to different magnetic states (singlet vs. triplet)—owed directly to this fermionic principle. To understand how Coulomb repulsion influences magnetic states, we consider the energy contribution from electron-electron repulsion, which can be expressed as

$$U_C = \int \psi^*(\boldsymbol{r}_1, \boldsymbol{r}_2) \frac{e^2}{|\boldsymbol{r}_1 - \boldsymbol{r_2}|} \psi(\boldsymbol{r}_1, \boldsymbol{r}_2) d\boldsymbol{r}_1 d\boldsymbol{r}_2 \tag{2.9}$$

This integral depends on the symmetry of the spatial wavefunction, $\psi(\boldsymbol{r}_1, \boldsymbol{r}_2)$, and the distance between the two electrons $|\boldsymbol{r}_1 - \boldsymbol{r_2}|$. Symmetric wavefunctions lead to higher probabilities of electron overlap due to constructive interference, while antisymmetric wavefunctions suppress overlap via destructive interference[3]. This difference directly impacts the

[3]For example, one can expand the probability densities $|\psi|^2$ of the wavefunctions $\psi_S = \frac{1}{\sqrt{2}}[\phi_a(x_1)\phi_b(x_2) + \phi_a(x_2)\phi_b(x_1)]$ and $\psi_{AS} = \frac{1}{\sqrt{2}}[\phi_a(x_1)\phi_b(x_2) - \phi_a(x_2)\phi_b(x_1)]$ in order to see the explicit difference in how the interference terms contribute.

Coulomb energy, U_C, as regions with greater overlap will contribute significantly more to the repulsion term. Consequently, the symmetry of the spatial wavefunction, enforced by the Pauli Exclusion Principle, dictates the energy differences between the singlet and triplet states, thereby determining the magnetic state of the system. In this way, we see that the exchange interaction—arising fundamentally from the symmetry constraints and energetic considerations of electron wavefunctions—is the driving force behind the magnetic coupling. This is one of the more simple cases of exchange interactions known as *direct exchange*, where electron orbitals spatially overlap, and demonstrates how this quantum mechanical principle governs the alignment of spins through the overlap of electronic orbitals, establishing the foundation for the more complex exchange mechanisms encountered in rare-earth materials.

The exchange interaction can be formally described using the Heisenberg model. In this framework, the interaction between neighboring spins $\boldsymbol{S}_i$ and $\boldsymbol{S}_j$ is expressed as

$$\mathcal{H} = -J \sum_{i,j} \boldsymbol{S}_i \cdot \boldsymbol{S}_j \tag{2.10}$$

Here, J represents the exchange interaction strength, determining whether the coupling is ferromagnetic ($J > 0$) or antiferromagnetic ($J < 0$). Typically, this sum is taken over all pairs of nearest-neighbor spins, meaning the interaction depends only on the relative orientations of the two spins. While J is often treated as isotropic, more complex anisotropic interactions can be incorporated by modifying the J term. In this context, J functions similarly to the Coulomb energy integral discussed earlier, encoding the strength of the magnetic coupling by quantifying the overlap between the spatial wavefunctions of neighboring electrons. A larger overlap corresponds to a stronger exchange interaction, as it enhances the probability of finding paired electrons in favorable spin configurations, thereby lowering the system's total energy. Conversely, smaller overlaps result in weaker coupling.

While direct exchange provides a straightforward mechanism for spin coupling, it is limited in systems where electronic wavefunction overlap is negligible. In such cases, the interaction between magnetic ions can be mediated by an intermediate ion, such as O^{-2}. This

mechanism, known as *superexchange*, depends on the bond angle and orbital overlap between the magnetic ions and the intermediate ion, which determine whether the interaction is ferromagnetic or antiferromagnetic, as outlined by the Goodenough-Kanamori rules [22, 23] and illustrated in Fig. 2.2b. In the case of superexchange, the effective exchange interaction strength J can be calculated based on the orbital overlaps and the intermediary ion, following a perturbative treatment of the electronic interactions. Superexchange is particularly important for the rare-earth insulators in this work, where the localized nature of $4f$ electrons prevents direct orbital overlap but allows indirect coupling through intervening ligands.

For completeness, several other exchange mechanisms should be mentioned, although they are not central to the systems considered in this work. The anisotropic Dzyaloshinskii-Moriya (DM) interaction arises from spin-orbit coupling in systems lacking inversion symmetry, leading to asymmetric exchange and often resulting in noncollinear or chiral spin structures. However, the materials in this study retain inversion symmetry at relevant interaction sites, rendering the DM interaction negligible. The Ruderman-Kittel-Kasuya-Yosida (RKKY) interaction, which operates in metals through conduction electrons, leads to oscillatory spin coupling. As this mechanism relies on a metallic conduction electron sea, it is irrelevant in the insulating rare-earth systems under consideration. Finally, itinerant exchange, where magnetic ordering arises from the collective behavior of delocalized electrons, is prominent in systems with high electronic mobility, such as transition metals. However, in rare-earth insulators with localized $4f$ electrons, this mechanism is similarly insignificant. These alternative interactions, while critical in other contexts, do not significantly influence the magnetic properties of the rare-earth systems discussed here.

At high temperatures, where the thermal energy k_BT exceeds the interaction energies J between magnetic moments, thermal fluctuations dominate, leading to random orientations of magnetic moments and a paramagnetic state. As the system cools and $k_BT < J$, magnetic interactions begin to dominate. At sufficiently low temperatures, these interactions, shaped by the crystal structure and the nature of the coupling mechanisms, drive the system toward

an equilibrium magnetic configuration. This equilibrium can result in a well-defined ground state magnetic order, such as ferromagnetic, antiferromagnetic, or more exotic arrangements. In some cases, however, competing interactions or geometric constraints lead to frustration, preventing the system from reaching a unique ground state. This phenomenon, and its implications for magnetic order, will be discussed in the next section.

2.1.2 Frustrated magnets

Frustration in magnetic systems occurs when competing interactions prevent the system from simultaneously minimizing all interaction energies, leading to a complex energy landscape with many nearly-degenerate low-energy states. This phenomenon, known as magnetic frustration, often suppresses magnetic ordering or drives ordering transitions to extremely low temperatures. As a result, frustrated materials frequently exhibit unconventional phases and exotic physical properties, making them a rich area of study.

The origins of frustration can be broadly classified into two categories: exchange frustration and geometric frustration. Exchange frustration arises when competing interactions between spins occur at comparable energy scales, such as those between nearest and further neighbors or anisotropic differences. Geometric frustration, on the other hand, stems from the spatial arrangement of spins in a lattice, where the geometry inherently prevents all interactions from being simultaneously satisfied.

A classic example of geometric frustration involves antiferromagnetically (AFM) coupled Ising spins on a triangular lattice Fig. 2.3a. In this system, three spins on a triangular plaquette cannot simultaneously achieve AFM alignment, resulting in a frustrated configuration. When extended to a full lattice, this frustration creates an infinitely degenerate ground state manifold. Other prominent examples of geometrically frustrated lattices include the kagome, pyrochlore, perovskite, and honeycomb lattices.

Exchange frustration is demonstrated in Fig. 2.3b, where AFM spins are arranged on a square plaquette. Without frustration, the system adopts a simple Néel configuration, as

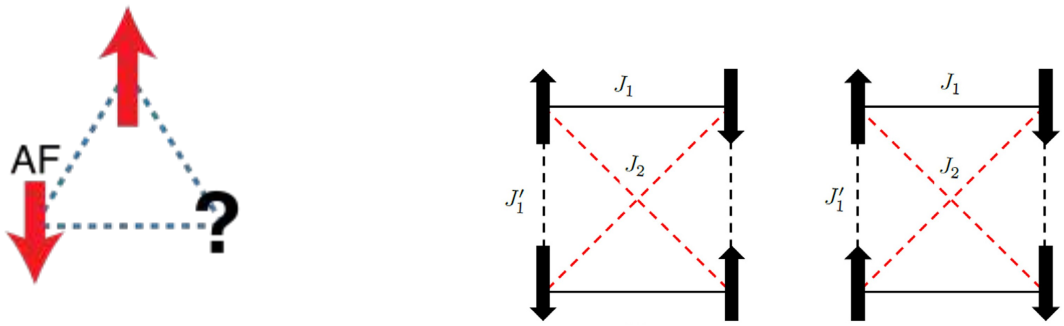

(a) (b)

Figure 2.3: Examples of frustration in magnetic systems on a portion of a lattice. (a) Canonical example of geometric frustration of Ising spings on a triangular lattice. (b) Exchange frustration on the square lattice due to competing interactions between anisotropic nearest neighbors (J_1, J_1') and next-nearest neighbors (J_2) leading to different configurations based on the relative strength of each interaction [4].

shown on the left. However, introducing competing interactions with varying strengths (J_1, J_1', J_2) creates frustration, potentially leading to complex configurations or even the absence of a unique ground state, depending on the relative strengths of these interactions.

In real materials, both exchange and geometric frustration often coexist, leading to rich and complex behavior. Despite frustration, many systems eventually achieve magnetic ordering at temperatures below T_N, often facilitated by weaker interactions that can eventually tip the balance into a local minimum. The degree of frustration in a system can be quantified by the frustration parameter:

$$f = \frac{|\theta_{CW}|}{T_N} \tag{2.11}$$

where θ_{CW} is the Curie-Weiss temperature (discussed later in Section 2.2.4). Essentially, this is a ratio between the average interaction strength and the suppressed critical temperature, so a higher f value generally corresponds to strong frustration within a magnetic material.

The suppression of magnetic order to ultra-low temperatures creates opportunities to study quantum effects, including the potential emergence of Quantum Spin Liquids (QSLs) [24]. Even in materials that do not host a true QSL ground state, proximity to these

exotic states often stabilizes unconventional phases or leads to emergent behaviors. Studying frustrated materials thus offers a unique opportunity to explore the boundaries of quantum physics and discover new avenues for theoretical and experimental research.

2.1.3 Spin-orbit coupling and crystal field effects

The heavy rare earth ions forming the set of lanthanides are characterized by their $4f$ electron orbitals. Due to the large orbital angular momentum L of these orbitals and the inherently relativistic nature of spin-orbit coupling (SOC) in heavy elements, the total angular momentum $J = L + S$ becomes the good quantum number[4], leaving the effects of spin-orbit coupling (SOC) impossible to ignore. Under this effect, the single ion ground states form $(2J + 1)$ degenerate energy levels which are then further split by additional perturbations. In the crystalline structure of rare earth insulators, the most prominent of these perturbations is the Stark splitting of these states due to the crystalline electric field (CEF), where surrounding ligand ions of negative charge create an electric field seen by the rare earth ions. The energy scale of these CEF interactions is typically small compared to the spin-orbit coupling, thus allowing the use of standard perturbation theory in order to understand its effects [5].

Starting with SOC as the dominant interaction, we use Hund's rules to determine the degenerate manifold of $(2J + 1)$ states that form the ground state multiplet. These rules describe how electrons in the $4f$ orbitals arrange themselves to minimize the total energy of the ion, as illustrated with the example of the Yb^{3+} ion in Fig. 2.4. The first rule dictates that the total spin angular momentum S is maximized, as anti-parallel spins grouped pairwise reduce electron-electron repulsion according to the Pauli exclusion principle. Next, the

[4]Note that when the orbital angular momentum L=0, the total angular momentum J equals the spin angular momentum S, making S and m_S the relevant quantum numbers. In such cases, explicitly using J and m_J becomes redundant.

[5]This is in stark contrast to magnetic materials utilizing transition metal elements, as those d orbitals contain less orbital angular momentum. In this case, CEF <SOC, so we can tabulate states in the LS basis and apply SOC as the small perturbation. This distinction is further amplified in lanthanide ions due to the $5s$ and $5p$ shielding of the $4f$ orbitals.

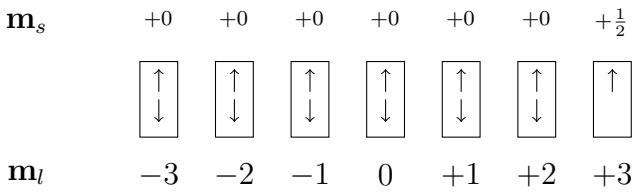

Figure 2.4: Hund's rules filling of $4f^{13}$ electrons in an isolated Yb^{3+} ion. First, we maximize $S = \sum m_S = 1/2$. Then we maximize $L = \sum m_L = 3$. And finally, since this is a more-than-half- filled subshell, we obtain $J = S + L = 7/2$. This can be compactly notated with the spectroscopic term symbol ${}^2F_{7/2}$ (written in the form ${}^{2S+1}L_J$).

total orbital angular momentum L is maximized within the constraints of the first rule, as electrons preferentially occupy orbitals that extend further apart in space, reducing Coulomb repulsion. Finally, the total angular momentum J is determined by coupling L and S based on the relative strength of spin-orbit coupling: for less-than-half-filled orbitals, $J = |L - S|$, while for more-than-half-filled orbitals, $J = L + S$. These rules define the ground state multiplet of the free ion, consisting of $(2J+1)$ degenerate states in the absence of additional interactions, such as those arising from the CEF.

Since the CEF arises from the electrostatic potential created by surrounding ligand ions, its effect on the rare-earth ion is determined by the local symmetry of the crystal environment. The CEF Hamiltonian, $\mathcal{H}_{\text{CEF}}$, must respect the point group symmetry of the ion's site, meaning it can be expressed as a sum of terms that transform according to the irreducible representations of the group. A convenient way to construct such a Hamiltonian is by expanding it in terms of Stevens operators, which are tesseral tensor operators adapted to the symmetry of the crystal field. This expansion takes the general form

$$\mathcal{H}_{\text{CEF}} = \sum_{l,m} B_l^m \hat{O}_l^m \tag{2.12}$$

where B_l^m are material-dependent coefficients that parameterize the strength of the CEF interaction for a given symmetry environment[6], and $\hat{O}_l^m$ are the Stevens operators, which

[6]These are known as Stevens parameters or Crystal Field (CF) parameters. Additionally, depending on the particular source/convention, the rank/order of the operator tensor l and component m may be instead

are the tensor operators constructed to reflect the point group symmetry at the rare earth site. Just as electronic orbitals in a central potential can be expanded in terms of spherical harmonics—since the potential exhibits full rotational symmetry—the electrostatic potential of a crystal, which conforms to the discrete symmetry of a lattice, must instead be expanded in terms of tesseral harmonics, which themselves are the real-valued expansions of the spherical harmonics. In other words, while spherical harmonics provide a natural basis for spherically symmetric systems, the crystal environment lacks full rotational symmetry due to the periodic arrangement of ions. This requires a harmonic expansion that reflects the lower, discrete symmetry of the lattice.

Stevens formalized this approach by demonstrating that the mathematical formulation of tesseral harmonics—originally expressed in terms of Cartesian coordinates x, y, z—could be systematically rewritten in terms of the noncommuting angular momentum operators $\hat{J}_x$, $\hat{J}_y$, $\hat{J}_z$. This substitution allows the Hamiltonian to be expressed in a basis of atomic states labeled by J, m_J, rather than spatial coordinates. The Wigner-Eckart theorem then provides a systematic method for computing matrix elements of these operators, significantly reducing the complexity of solving the crystal field problem compared to the tedious nature of keeping everything in Cartesian coordinates [25, 26, 27, 28, 29].

From a purely mathematical sense, Eq. 2.12 would suggest an infinite number of Stevens parameters and operators. However, physically relevant symmetries require certain coefficients go to zero, drastically reducing the number of coefficients to be calculated or fit. Time reversal symmetry restricts l to be even, while the allowed values of m are constrained within $-l \leq m \leq l$ [30]. Furthermore, since l is limited by $l \leq 2L$, where L is the orbital quantum number, $4f$ rare earth ions where $L = 3$ restricts the expansion to terms up to sixth order at most. This leaves a potential of 27 possible non-zero coefficients. This set of coefficients is then further reduced depending on the spatial symmetry of the crystalline lattice being investigated. The lowest triclinic symmetries will retain all 27 parameters, while a higher

indexed with (k, q) or (n, m). These should be seen as equivalent.

Table 2.2: Possible local symmetries and corresponding non-zero CEF parameters. The sign ± indicates that both B_l^m and B_l^{-m} can be nonzero, but one of these B_l^m can be set to zero by a proper choice of coordinate system.

Symmetry	**Point Group**	B_2^0	$B_2^{\pm1}$	$B_2^{\pm2}$	B_4^0	$B_4^{\pm1}$	$B_4^{\pm2}$	$B_4^{\pm3}$	$B_4^{\pm4}$	B_6^0	$B_6^{\pm1}$	$B_6^{\pm2}$	$B_6^{\pm3}$	$B_6^{\pm4}$	$B_6^{\pm5}$	$B_6^{\pm6}$
Triclinic	C_i, C_1	+	±	±	+	±	±	±	±	+	±	±	±	±	±	±
Monoclinic	C_2, C_s, C_{2h}	+		±	+		±		±	+		±		±		±
Rhombic	C_{2v}, D_2, D_{2h}	+		+	+		+		+	+		+		+		+
Tetragonal	C_4, S_4, C_{4h}	+			+				±	+				±		
Tetragonal	$D_4, C_{4v}, D_{2d}, D_{4h}$	+			+				+	+				+		
Trigonal	C_3, S_6	+			+			±		+			±			±
Trigonal	D_3, C_{3v}, D_{3d}	+			+			+		+			+			+
Hexagonal	C_6, C_{3h}, C_{6h}	+			+					+						±
Hexagonal	$D_6, C_{6v}, D_{3h}, D_{6h}$	+			+					+						+
Cubic	T, T_d, T_h, O, O_h				+				+	+				+		
Icosahedral	I_h									+					+	

symmetry—such as cubic—will reduce the complete description of the electrostatic potential down to 4 parameters[7]. In a few situations, a proper choice of coordinate system or mathematical similarites in the tesseral harmonics can further simplify the number of terms [31, 32, 33]. For example, for cubic symmetry $B_4^4 = \frac{5}{2}B_4^0$ and $B_6^4 = -\frac{21}{2}B_6^0$. A complete table of crystallographic point-group symmetries and their corresponding non-zero CF parameters is given in Table 2.2.

Determining the CF parameters in real materials is significantly more challenging than the mathematical formalism suggests. As a starting point, point charge calculations provide an initial estimate of CF energy levels by treating the ligand ions as fixed electrostatic charges surrounding the rare-earth ion. This approach, while simplistic, is often useful in the early stages of experimental planning, particularly for techniques such as neutron scattering, where estimating expected CF excitation energies can guide instrument setup and data interpretation. The primary limitation of point charge models is their assumption of static ligand charges, neglecting covalency effects and hybridization, which can strongly influence the CF potential in real materials.

Extracting CF parameters directly from experimental data is difficult for several reasons. First, not all CF levels are necessarily resolvable within the energy resolution of the instrument, especially in neutron and optical spectroscopies where closely spaced levels may merge. Second, some CF excitations may exhibit low intensity, making them difficult to detect even when they fall within the accessible energy range. A further complication arises when CF levels overlap with phonon modes, as both can exist on similar energy scales. However, these contributions can often be distinguished by their momentum transfer (Q) dependence. Phonon scattering intensities generally scale as Q^2 at low Q due to their coupling to nuclear displacements, whereas CF excitations follow the magnetic form factor $|F(Q)|^2$, which decreases gradually with increasing Q. This difference provides an experimental means of

[7]In theory, systems with icosahedral symmetry will further reduce the number of CF coefficients to 2 parameters, though this case is not compatible with translational symmetry and is typically only relevant to a class of isolated molecules.

separating phonon and CF contributions in neutron scattering data. Even when CF transitions are unambiguously identified, fitting them to an appropriate Hamiltonian often results in multiple degenerate parameter sets, making a unique determination of CF coefficients challenging.

A refinement of the point charge approach is the effective point charge model, in which the ligand charges are treated as adjustable parameters rather than fixed values. This significantly reduces the number of free parameters in the fitting process, making it easier to constrain the CF potential. However, this method remains an approximation, and in some cases, the fitted ligand charges may deviate significantly from physically reasonable values. As noted by Lea et al. [34], effective point charge models sometimes yield empirical success, but they do not always provide a robust or universally applicable description of the CF environment.

For rare-earth ions with an odd number of electrons, an additional symmetry constraint emerges from Kramers' theorem, which states that in the absence of time-reversal symmetry breaking, all energy levels remain at least twofold degenerate. This degeneracy is a direct consequence of time-reversal symmetry, which ensures that all states in a system with an odd number of electrons remain at least twofold degenerate. In the absence of external perturbations, such as a magnetic field, these Kramers doublets cannot be lifted. Consequently, in many Kramers ions, the lowest energy CF doublet can be accurately mapped onto an effective spin-1/2 system, allowing the interactions between moments to be described using a simplified spin Hamiltonian instead of the full J-multiplet formalism.

This effective spin-1/2 picture is particularly useful in modeling quantum magnetism, as it allows for simplified descriptions of exchange interactions and collective phenomena in rare-earth-based materials. However, the validity of this approximation depends on the energy separation between the ground doublet and excited CF states. If excited CF states lie at sufficiently high energies, then at low temperatures, the physics of the system is well captured by the effective spin-1/2 representation. Conversely, if the CF excitations are

on a similar energy scale to thermal fluctuations, higher-order multiplet contributions may become significant, requiring a more complete treatment of the full J-manifold.

2.1.4 Bond-Dependent Anisotropy

Magnetic interactions in condensed matter systems are typically categorized based on their symmetry properties. Conventional spin models, such as the Heisenberg and Ising models, rely on general symmetry arguments, where exchange interactions are typically classified by spatial or spin rotational symmetries. These models assume that interactions are uniform or, when anisotropic, vary in a manner dictated by global symmetries rather than local bond-dependent rules. However, in systems with strong spin-orbit coupling and specific lattice geometries, theoretical studies suggest that exchange interactions may become bond-dependent, leading to distinct anisotropic magnetic behaviors [35]. This phenomenon, known as bond-dependent anisotropy, is considered a potential mechanism for realizing exotic magnetic states, such as QSL's, though its direct experimental confirmation remains an ongoing challenge in condensed matter research [36].

The concept of bond-dependent anisotropy emerged from early studies on spin-orbit coupling and exchange anisotropies. Initially, magnetic interactions were largely understood within the framework of isotropic Heisenberg exchange (Eq. 2.10), but the inclusion of relativistic spin-orbit coupling led to a broader perspective on anisotropic exchange. The Dzyaloshinskii-Moriya (DM) interaction was one of the first widely recognized anisotropic terms, arising in non-centrosymmetric environments due to spin-orbit coupling [37, 38]. However, even in centrosymmetric systems, researchers realized that spin-orbit interactions could generate exchange terms that are explicitly dependent on the direction of the bond between interacting spins [39]. This realization led to the development of compass models, which are characterized by interactions that act selectively on different spin components depending on the bond direction. That is, along one bond, one spin component dictates the interaction, while along another, a different spin component is involved. This directional dependence

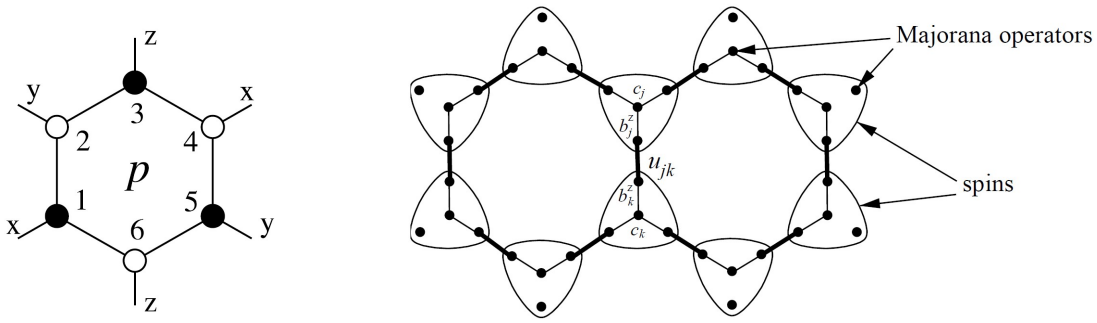

(a) (b)

Figure 2.5: (a) Diagram of a single plaquette p on the bipartite honeycomb lattice illustrating the three types of links: x, y, and z. (b) Illustration of the Majorana fermionization of each spin operator into four Majorana operators at each lattice site.

leads to highly anisotropic exchange interactions, distinguishing compass models from conventional isotropic or globally anisotropic spin models. Examples include the 90° compass model, the Kitaev model on the honeycomb lattice, and the 120° compass model, each of which exhibits unique magnetic properties and quantum effects [40, 41].

Among the various compass models, each with its own intriguing properties, the Kitaev model is particularly notable for its exact solvability, its quantum spin liquid ground state, and the presence of anyonic excitations that have been proposed as a platform for topological quantum computation. Additionally, the Kitaev model provides a clear example of bond-dependent anisotropic exchange interactions, and its experimental realization is a central objective of this work. Therefore, we will outline the key aspects of this model here.

The Kitaev model is a quantum field theory (QFT) defined for spin-1/2 particles on a honeycomb lattice, where spin interactions are bond-dependent in a unique manner. Unlike conventional Heisenberg or Ising interactions, which are either isotropic or globally anisotropic, the Kitaev model enforces interactions that depend explicitly on the bond direction. The Hamiltonian governing this system is given by:

$$\begin{aligned}\mathcal{H}_{\text{Kitaev}} &= -J_\alpha \sum_{\langle ij\rangle_\alpha} \sigma_i^\alpha \sigma_j^\alpha \\ &= -J_x \sum_{x-links} \sigma_i^x \sigma_j^x - J_y \sum_{y-links} \sigma_i^y \sigma_j^y - J_z \sum_{z-links} \sigma_i^z \sigma_j^z\end{aligned} \tag{2.13}$$

where J_α is the interaction strength along the α ($\alpha = x, y, z$) bond (depicted in Fig. 2.5a), σ_i^α are spin-1/2 operators at lattice site i, acting along the bond direction α and coupling to the corresponding spin component of its nearest-neighbor site j, denoted as σ_j^α. The sum runs over all pairs of nearest neighbors for each α bond. By applying a Majorana fermionization procedure, where each spin operator is decomposed into four Majorana fermion operators $\{c, b_i^\alpha, b_j^\alpha, b_k^\alpha\}$, Kitaev showed that the first term in Eq. 2.13 can be rewritten as a quadratic Hamiltonian of the form

$$\tilde{\mathcal{H}} = \frac{i}{4}\sum_{j,k}\hat{A}_{jk}c_j c_k, \quad \hat{A}_{jk} = \begin{cases} 2J_\alpha \hat{u}_{jk}, & \text{if } j \text{ and } k \text{ are connected,} \\ 0, & \text{otherwise.} \end{cases} \tag{2.14}$$

$$\hat{u}_{jk} = i b_j^\alpha b_k^\alpha$$

where the link operator $\hat{u}_{jk}$ acts as a $\mathbb{Z}_2$ gauge field, encoding the bond-dependent interaction, and corresponds to the transfer of a Majorana fermion between sites j and k. The structure of this Hamiltonian is shown in Fig. 2.5b. Its quadratic form is reminiscent of the many-body quantum harmonic oscillator $\mathcal{H}_{\text{QHO}} = \sum_k \hbar\omega_k(a_k^\dagger a_k + \frac{1}{2})$ [42]. Similar to how $\mathcal{H}_{\text{QHO}}$ can be diagonalized using normal bosonic modes, leading to a sum of non-interacting harmonic modes, $\mathcal{H}_{\text{Kitaev}}$ can be exactly solved by diagonalizing the system into non-interacting fermionic modes. The key differences in this theory is the use of Majorana fermions[8], which obey anticommutation relations (as opposed to commutation relations for bosons), and the underlying static $\mathbb{Z}_2$ gauge field[9] represented by $\hat{u}_{jk}$. Thus, while $\mathcal{H}_{\text{Kitaev}}$

[8]Majorana fermions are defined as fermionic particles that are also their own antiparticles. In QFT, this is mathematically expressed by requiring that the charge conjugation of a fermionic operator returns the same operator, e.g., $C^{-1}c_{\boldsymbol{p}}^\dagger C = c_{\boldsymbol{p}}^\dagger$.

[9]A gauge field is a mathematical construct that describes how symmetries, typically local in nature, govern interactions in a physical system. In classical physics, the electromagnetic field is an example of a U(1) gauge field, where the phase of the wavefunction can change locally without affecting physical observables. In QFT, gauge fields are associated with conserved charges via Noether's theorem and can be classified by the structure of their symmetry group. A $\mathbb{Z}_2$ gauge field is a discrete version, where the relevant symmetry only takes values ± 1, and is commonly associated with systems where fermions interact through background constraints rather than continuous forces. Unlike U(1) or SU(2) gauge fields in electromagnetism or the Standard Model, a $\mathbb{Z}_2$ gauge field typically emerges in condensed matter systems and lattice gauge theories, where it can describe topological order, fractionalized excitations, and constrained degrees of freedom.

is formally quadratic, the presence of the fixed $\mathbb{Z}_2$ gauge field fundamentally distinguishes it from a trivial free-fermion system, leading to rich emergent phenomena.

Having rewritten the Hamiltonian in terms of Majorana fermions and a static $\mathbb{Z}_2$ gauge field, we now examine the nature of its ground state, which takes the form

$$|\Psi\rangle = \prod_i (\frac{1+D_i}{2})|\Psi_0\rangle \tag{2.15}$$

Here, $D_i = b_i^x b_i^y b_i^z c_i$ is a local $\mathbb{Z}_2$ gauge transformation acting at site i, and $|\Psi_0\rangle$ is the state for a fixed gauge field configuration. Unlike many other QSL's, where the ground state is a sum over configurations of singlet bonds [43, 44, 36], the Kitaev QSL is instead expressed as a product of projection operators acting on a reference state. This structure ensures that the wavefunction remains within the physical Hilbert space, enforcing gauge constraints at every site.

Expanding this expression explicitly yields

$$|\Psi\rangle = (\frac{1+D_1}{2})(\frac{1+D_2}{2})(\frac{1+D_3}{2})\cdots|\Psi_0\rangle \tag{2.16}$$

This product form means that every site is correlated with every other site indirectly through the gauge field, rather than forming simple spin-spin entanglement. Unlike conventional spin liquids, where the degrees of freedom are fluctuating spin singlets, the Kitaev QSL is best understood as a fluctuating quantum liquid of $\mathbb{Z}_2$ gauge fluxes, with itinerant Majorana fermions propagating in this background. This structure not only leads to long-range entanglement without symmetry-breaking order but is also a hallmark of topologically ordered phases. The presence of a static $\mathbb{Z}_2$ gauge field enables the emergence of fractionalized excitations, where spin degrees of freedom decompose into itinerant Majorana fermions and localized gauge fluxes, distinguishing the Kitaev QSL from more conventional magnetically ordered states [45].

While the Kitaev model provides an analytically solvable framework for understanding

bond-dependent anisotropy, real materials inevitably introduce additional interactions, such as residual Heisenberg exchange and lattice distortions, that complicate the realization of an ideal QSL. As a result, directly verifying the presence of Kitaev-like interactions requires identifying unique experimental signatures that distinguish bond-dependent exchange from conventional magnetic interactions. The challenge lies in determining whether observed excitations truly reflect fractionalization or stem from competing interactions that disrupt the idealized Kitaev picture.

In this regard, rare-earth materials provide a promising platform for realizing bond-dependent anisotropic interactions. Unlike d^5 transition metal compounds such as α-$RuCl_3$, which rely on strong spin-orbit coupling within t_{2g} orbitals, rare-earth systems exhibit even stronger spin-orbit coupling due to their unquenched orbital angular momentum. This naturally leads to highly anisotropic exchange interactions, making rare-earth magnets a compelling alternative for exploring Kitaev-like physics. The combination of strong spin-orbit coupling and crystalline electric field effects in rare-earth systems provides an ideal setting for stabilizing effective pseudospin-1/2 moments, which are essential for realizing compass-like exchange interactions.

Bond-dependent anisotropy fundamentally alters the nature of magnetic interactions and are proposed to lead to unconventional quantum states such as the Kitaev quantum spin liquid. The presence of such interactions in real materials can often be inferred through characteristic experimental signatures. Inelastic neutron scattering, for example, can reveal a continuum of fractionalized excitations rather than the sharp magnon modes expected in conventional magnets, making it a crucial tool for identifying bond-dependent exchange interactions [46, 47, 48, 45]. Heat capacity and magnetic susceptibility measurements, while not directly resolving these excitations, provide valuable thermodynamic insights and can guide neutron scattering experiments by identifying phase transitions or anomalies linked to anisotropic exchange [49, 50, 51]. Other techniques, such as Raman spectroscopy and thermal transport, have been proposed as additional probes of emergent Majorana fermions

and high-energy excitations in candidate materials [52, 53, 54, 55]. In the next section, we turn to the methodologies used to probe these effects and assess the experimental realization of bond-dependent anisotropic interactions.

2.2 Experimental Techniques

2.2.1 Instrumentation

This work relied extensively on the use of commercial instrumentation, as well as home-built solutions, to probe the magnetic and structural properties of materials. In many cases, standard experimental procedures required modification to accommodate specific material constraints. In particular, some samples exhibited strong air sensitivity, necessitating the development of air-free handling techniques to ensure accurate measurements. The specialized methodologies developed for this project are discussed later in Section 4.3.

As an experimentalist, careful consideration of the instruments used is integral to producing reliable data. Even with commercialized setups, each experiment requires attention to how measurements are performed and how instrumental parameters—such as temperatures stability, addenda properties, and calibration—may influence the data.

This section is structured to reflect the typical workflow in the experimental investigation of magnetic phenomena. We begin with an overview of the synthesis techniques employed to produce rare-earth-based crystals, emphasizing the level of precision required to achieve high-quality samples. Next, we examine characterization techniques used for structural analysis, with a focus on x-ray diffraction as a tool for determining crystallographic properties. We then discuss thermodynamic measurements—including magnetometry and specific heat—which provide insights into the fundamental magnetic and thermal behaviors of the materials. Finally, we describe neutron scattering experiments, a powerful technique uniquely sensitive to magnetic correlations and capable of directly probing spin dynamics, which played a central role in this work.

2.2.2 Single Crystal Synthesis

The ability to grow high-quality single crystals was central to this work, as the fundamental magnetic properties of rare-earth materials can only be fully understood in well-ordered structures with minimal defects. These crystals enable precise measurements of anisotropic interactions, collective excitations, and exotic magnetic states. Over the course of this research, a range of synthesis techniques — including chemical vapor transport (CVT), the Bridgman method, and optical float zone (OFZ)—were employed, with the choice of method dictated by the material's physical and chemical properties as well as the specific experimental requirements.

For all of the materials investigated, maintaining a contamination-free synthesis environment was essential, as unintended impurities could significantly alter their magnetic behavior. In some cases, such as $ErCl_3$, high-purity powder could be directly crystallized. However, for others, such as $Yb_2Si_2O_7$, synthesis began with commercial precursors that required stoichiometric mixing and high-temperature sintering to form a polycrystalline phase before crystallization.

The required crystal size depended on the intended experiment. For bulk measurements like magnetometry, high-quality single crystals as small as 10 mg were sufficient. However, neutron scattering experiments demanded much larger samples—up to 5 g—due to the inherently weak interaction between neutrons and matter. This weak scattering cross-section necessitates large crystal volumes to achieve adequate signal intensity, particularly for inelastic measurements where scattering events are further constrained by energy and momentum transfer conditions. As a result, refining growth conditions to maximize crystal yield while maintaining targeted crystallinity was critical to ensuring reliable neutron scattering data.

Achieving structurally well-ordered single crystals was essential, as even minor impurities or structural imperfections could obscure the magnetic phenomena under investigation. While no real crystal is entirely free of defects, minimizing disorder is crucial for accurately interpreting experimental results. By systematically refining synthesis conditions—guided

Figure 2.6: Optical float zone furnace (MODEL FZ-T-4000-H-VII-VPO-PC, Crystal Systems Corp.) used for large single-crystal growth of rare-earth silicates.

by insights from prior growths, experimental feedback, and comparison with literature—we developed procedures capable of reliably producing crystals with the necessary crystallinity and phase purity.

The optical float-zone (OFZ) technique was employed for the synthesis of rare-earth silicates ($R_2Si_2O_7$) due to its ability to produce large, structurally ordered single crystals without contamination from crucible materials. Success in this method depended heavily on the quality of the precursor materials and the precise control of thermal conditions during growth [56].

The optical float-zone furnace (MODEL FZ-T-4000-H-VII-VPO-PC, Crystal Systems Corp.; Fig. 2.6) provided a controlled, crucible-free environment for single-crystal growth. This technique relies on focused halogen lamps to generate a high-temperature molten zone that traverses a polycrystalline feed rod. A pre-oriented seed crystal was used to initiate growth, guiding the structural development of the boule. The process involved counter-rotation of the feed and seed rods at approximately 20 rpm to maintain uniformity and

prevent asymmetries in the growth interface. The stability of the molten zone was influenced by surface tension and precise control of the growth rate, typically maintained between 1-5 mm/hr to balance crystal quality and yield.

Precursor powders of rare-earth oxides (R_2O_3) and silica (SiO_2) were mixed stoichiometrically to ensure proper phase formation. The homogenization process was critical, as the uniformity of the starting material influenced both the sintering efficiency and the subsequent crystal growth. Initial grinding was performed manually with a mortar and pestle to break down large agglomerates, while ball-milling was used in cases where finer grain sizes were necessary to promote better diffusion during sintering. To form a suitable feed rod for the OFZ process, the mixed powder was compacted using hydrostatic pressing at pressures up to 75 MPa, ensuring high density and mechanical stability.

Sintering of the pressed rods was conducted in a high-temperature box furnace at approximately 1300°C for several days, facilitating the reaction between rare-earth oxides and silica to form the desired polycrystalline phase. The progress of the reaction was evaluated by performing powder X-ray diffraction (PXRD) on the sintered product, determining whether additional sintering cycles were necessary to eliminate residual precursor phases. Iterative refinement of these conditions ensured high phase purity and structural integrity in the feed rods, both of which were essential for stable melting in the OFZ furnace.

A crucial aspect of this method was the refinement of crystallographic quality during growth. The initially formed boule often contained multiple competing domains, as evident from Laue X-ray diffraction images taken along its length (Fig. 2.7). As growth proceeded, domain selection naturally occurred, leading to a progressive reduction in structural disorder. Iterative seeding techniques were employed to enhance this effect; using a well-oriented segment of a previous growth as a seed minimized domain competition and improved crystallinity in subsequent runs. While complete elimination of domain boundaries is rarely achievable, this approach significantly improved the overall crystal quality, making it suitable for neutron scattering and other precision measurements.

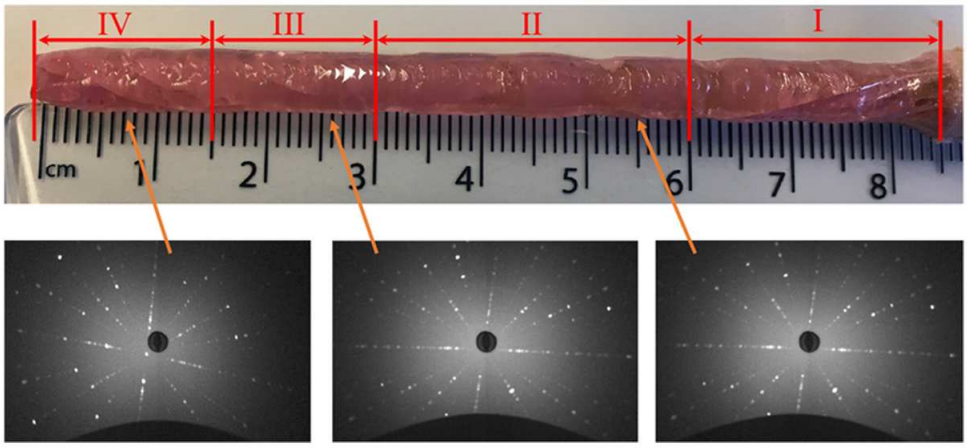

Figure 2.7: Top: Annotated image of a multicrystalline $Er_2Si_2O_7$ rod synthesized via the OFZ technique, with sections labeled I-IV corresponding to different positions along the length of the boule. Bottom: Laue X-ray images from selected regions of the rod, demonstrating the evolution of crystallinity during growth. The early portion of the boule (right, section I) exhibits multiple competing crystallographic domains, as evidenced by the presence of multiple diffraction spots with varying orientations. As growth progresses (moving left toward section IV), certain domains outcompete others, resulting in a more well-defined and singular crystalline orientation. This supports the natural selection process described in the text, where progressive refinement leads to a higher degree of crystallinity in the latter portions of the boule.

Atmospheric control played a significant role in optimizing the final crystal structure. The OFZ furnace was equipped with a gas flow system that allowed precise regulation of the surrounding environment. For the growth of rare-earth silicates, an oxygen flow of approximately 1 L/min was maintained to stabilize the silicate structure and minimize the incorporation of defects. Controlled cooling after growth was also essential; a gradual reduction in lamp power ensured a smooth thermal gradient, preventing excessive internal stresses that could lead to cracking.

The final products of this growth process were high-quality single crystals, typically measuring 8 mm in diameter and up to 7 cm in length. Due to thermal stress at grain boundaries, the boule often exhibited natural fracturing along single-crystal domains, which facilitated the isolation of structurally pristine regions for experimental use. Representative images of these OFZ-grown crystals, along with their evolution in crystallinity, are provided in Fig. 2.7.

To synthesize single crystals of the rare-earth trichlorides (RCl_3), both chemical vapor transport (CVT) and the Bridgman method were investigated. CVT is a widely used technique for the growth of high-purity single crystals, particularly for materials that exhibit significant volatility at elevated temperatures. The process involves the sublimation of a solid-phase source material in a high-temperature region, followed by its deposition in a lower-temperature zone under a controlled temperature gradient (Fig. 2.8). This transport mechanism allows for purification of the material during crystal growth and can be tailored by adjusting variables such as temperature, pressure, and the choice of transport agents [57, 58].

A key advantage of CVT is its ability to produce faceted, well-ordered single crystals with minimal defects. By leveraging the differences in sublimation and condensation rates under controlled conditions, high-quality crystalline products can be obtained. The method is particularly effective for compounds that exhibit sufficient volatility, either intrinsically or through the use of transport agents. In some cases, the material itself can act as its own transport agent, eliminating the need for additional chemical reactants.

The success of CVT relies heavily on ampoule preparation and stability. To ensure a contamination-free environment, quartz ampoules must be meticulously cleaned, dried, and sealed to prevent unwanted reactions that could interfere with transport. Sealing the ampoules under vacuum while carefully shaping their ends into smooth hemispheres minimizes the risk of trapped gases, unintended nucleation sites, and weak points in the quartz that could lead to ampoule failure under thermal stress. Additionally, charge amounts must be carefully controlled, as excessive volatilization can generate internal pressures beyond the structural limits of the ampoule. Assuming complete volatilization, the internal pressure can be estimated using the ideal gas law

$$P = \frac{nRT}{V} \tag{2.17}$$

where P is the internal pressure, n is the number of moles of volatilized charge, R is the

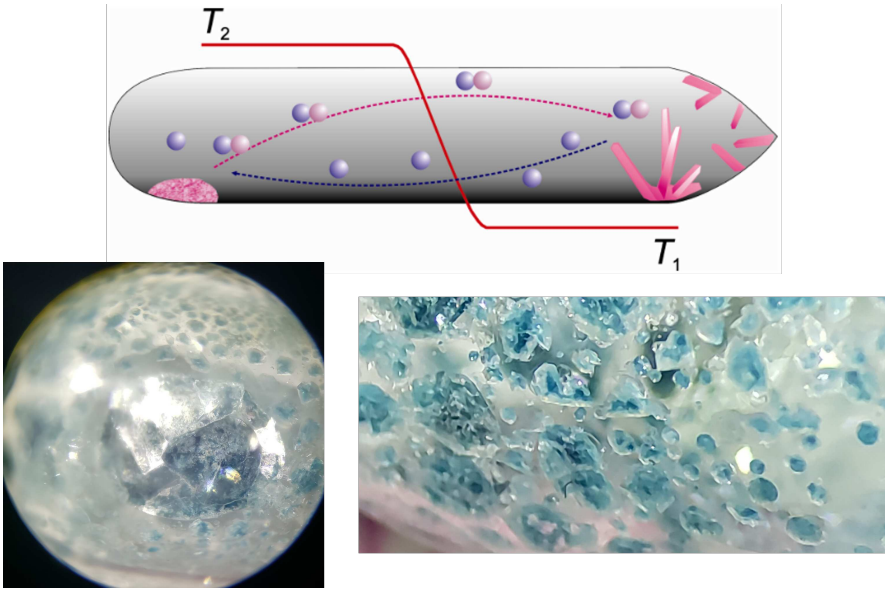

Figure 2.8: Top: Schematic illustration of the chemical vapor transport (CVT) process, depicting the sublimation of the source material in the high-temperature region (T_2) and its subsequent deposition in the lower-temperature zone (T_1). Bottom: Optical images of $YbCl_3$ crystals synthesized via CVT, highlighting their faceted morphology and crystalline features.

universal gas constant, T is the temperature in Kelvin, and V is the internal volume of the sealed ampoule. By carefully calculating n based on the charge mass and molecular weight, the expected pressure can be kept within a safe range to prevent ampoule failure. These factors collectively contribute to the reproducibility and efficiency of the CVT process.

The effectiveness of CVT varies depending on the material and desired crystal size. While it can be an excellent method for growing small, high-purity single crystals (Fig. 2.8), its scalability is often limited. For larger bulk crystals, alternative techniques such as the Bridgman method may be more suitable, as it allows for controlled solidification and better control over crystal size. The choice of growth method ultimately depends on the material properties and experimental requirements, balancing considerations of purity, scalability, and structural quality.

The Bridgman method is a widely used technique for growing bulk single crystals. In its conventional form, the process involves slowly lowering a sealed ampoule through a controlled temperature gradient, typically within a tube or multi-zone furnace. This ensures that the

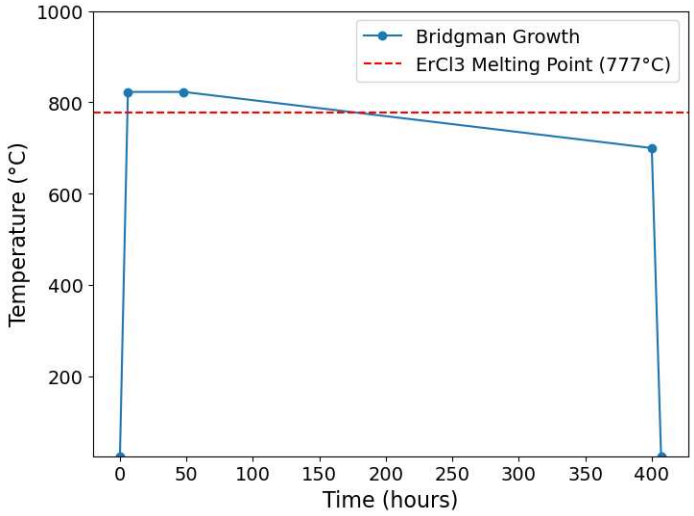

Figure 2.9: Temperature profile for $ErCl_3$ crystal growth using the modified Bridgman method. The schedule includes the initial heating phase above the melting point, an extended hold at 823°C, and a gradual cooling period over 1-2 weeks to promote high-quality crystallization. A final furnace-cooling step completes the process.

crystallization front moves at a steady rate, reducing the likelihood of grain boundaries and defects while promoting the growth of a single large crystal.

A key modification to this approach involves using a stationary ampoule positioned vertically inside a box furnace, where crystallization occurs as the furnace temperature is carefully controlled over time. First, the entire charge is heated to just above its melting point and held at this temperature to ensure complete liquefaction. Once fully molten, the furnace is gradually cooled, allowing solidification to begin at the base of the ampoule and progress upward. By carefully tuning the cooling rate and hold times, the solidification front advances steadily, reducing thermal stress and minimizing defect formation. An example of a modified thermal profile is shown in Fig. 2.9, where an extended hold above the melting point ensures full melting before gradual cooling promotes controlled crystallization.

During the solidification process, multiple crystallites may initially form before a dominant single-crystal domain emerges. This can result in polycrystalline outer layers that may need to be removed post-growth to isolate the high-quality single-crystal core (Fig. 2.10).

A major advantage of the Bridgman method, whether conventional or modified, is its

Figure 2.10: Single crystal of $ErCl_3$ grown using the modified Bridgman method. The translucent region represents the high-quality single-crystal core, while the outer polycrystalline regions were subsequently removed to isolate the crystal.

scalability. Unlike chemical vapor transport (CVT), which relies on gaseous intermediates and can be limited by transport kinetics, Bridgman growth allows for larger charge sizes primarily constrained by ampoule dimensions. Increasing the ampoule diameter enables the growth of larger single crystals without significantly altering other growth parameters. Additionally, because this method does not rely on gas-phase transport, internal ampoule pressures remain relatively low, reducing the risk of ampoule failure. These factors make Bridgman growth particularly well-suited for producing bulk single crystals for neutron scattering and other large-scale experimental applications.

2.2.3 X-Ray Diffraction

X-ray diffraction (XRD) is a fundamental technique for determining the crystallographic structure of synthesized materials, providing critical insights into phase purity, lattice parameters, and atomic arrangements. In this work, both powder X-ray diffraction (PXRD) and Laue diffraction were employed material characterization. PXRD enables phase identification and structural refinement by analyzing diffraction patterns from powdered samples, while Laue diffraction is used to assess single-crystal orientation and quality. Together, these techniques provide complementary structural information, ensuring the reliability of synthesized samples for further investigation.

Unlike neutron scattering, which primarily interacts with atomic nuclei (discussed later in Section 2.2.6), X-rays scatter predominantly from the electron density around atoms. As a result, XRD is particularly sensitive to elements with high atomic numbers, where greater electron densities produce stronger scattering. This makes XRD an excellent tool for structural characterization of rare-earth materials, but it also imposes limitations. In addition to being relatively insensitive to light elements such as hydrogen, X-rays have limited penetration depth in solids, making them less effective for probing deep bulk structures. Consequently, XRD primarily probes near-surface and subsurface regions, especially in high-Z materials where absorption effects are more significant.

At the core of X-ray diffraction is Bragg's Law, which describes the condition for constructive interference of X-rays scattered by periodic atomic planes within a crystal. This fundamental relationship is given by

$$n\lambda = 2d\sin(\theta) \tag{2.18}$$

where n is an integer representing the order of reflection, λ is the X-ray wavelength, d is the interplanar spacing between crystallographic planes, and θ is the Bragg angle—the angle of incidence at which diffraction occurs. When the path difference between X-rays scattered from adjacent atomic planes is an integer multiple of the wavelength, constructive interference amplifies the scattered intensity, producing distinct diffraction peaks (as illustrated in Fig. 2.11).

Bragg's Law provides the foundation for structural determination, as the positions and intensities of these diffraction peaks encode key information about the crystal lattice. By systematically varying the incident X-ray angle (θ) and measuring the resulting diffraction pattern, one can extract precise values for unit cell parameters, symmetry constraints, and atomic positions within the lattice. The unique set of diffraction peaks serves as a fingerprint of the material's structure, allowing for both phase identification and quantitative refinement of atomic coordinates. In practical applications, Bragg's Law is central to both powder X-ray

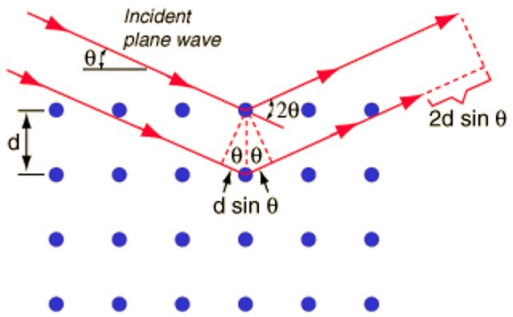

Figure 2.11: Illustration of Bragg's Law, showing the constructive interference of X-rays scattered from parallel atomic planes. The incident X-ray beam strikes the crystal at an angle θ, reflecting off atomic planes with an equivalent exit angle. The path difference between scattered rays from adjacent planes is $2d\sin(\theta)$, which must be an integer multiple of the wavelength (λ) to satisfy the Bragg condition: $n\lambda = 2d\sin(\theta)$.

diffraction (PXRD) and single-crystal diffraction.

In PXRD, a polycrystalline sample consists of randomly oriented crystallites, ensuring that all possible lattice planes contribute to the diffraction pattern. This results in a characteristic ring-like intensity distribution in reciprocal space, which is effectively captured as a one-dimensional diffraction profile (Fig. 2.12c).

For PXRD measurements, a finely ground sample is mounted on zero-diffraction silicon wafers[10] and exposed to a monochromatic X-ray beam using a Bruker D8 Discover diffractometer (Fig.2.12a). While the sample stage spins (to encourage all average orientations are being probed), the xray source and detector simultaneously move in order to sweep through the entire 2θ range, typically set to range from 20°–100°.

The resulting diffraction pattern is collected as a function of 2θ, effectively representing a radial slice through the full ring-like intensity distribution. The analysis of this pattern provides a wealth of structural information, including:

- **Peak positions**—Determine unit cell dimensions and phase identification.
- **Peak intensities**—Reveal phase fractions, site occupancies, and preferred orientation effects.

[10]Zero Diffraction Plates (ZDPs) are single-crystal silicon wafers precisely cut along a specific crystallographic orientation to minimize background scattering in the 2θ range of 20°– 100°.

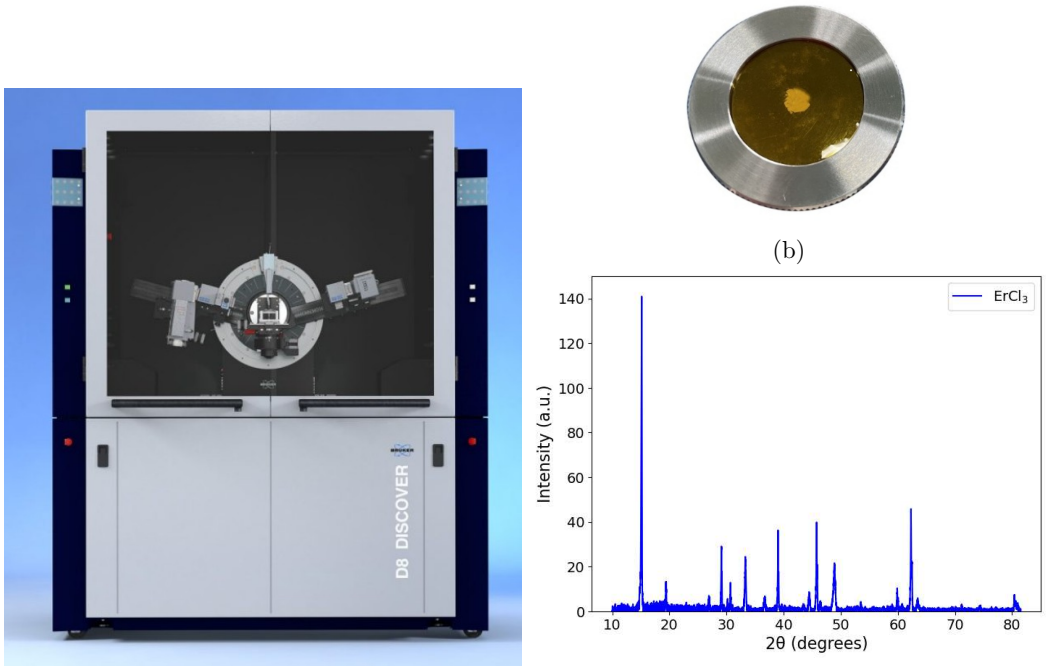

(a) (b) (c)

Figure 2.12: (a) Bruker D8 Discover used for PXRD measurements. (b) A powder sample sealed on a Si wafer with Kapton tape for diffraction of air-sensitive materials. (c) Example PXRD dataset showing a characteristic diffraction pattern of $ErCl_3$.

- **Peak widths**—Provide insight into crystallite size, microstrain, and defect concentration.

For simple phase identification, peak positions alone are sufficient, as they serve as a fingerprint of the material's crystal structure. In this work, Bruker EVA software was used to match experimental diffraction patterns against reference databases, enabling rapid phase identification. However, for a more detailed structural characterization, Rietveld refinement was performed using Bruker TOPAS, which quantitatively models the diffraction pattern. This method refines atomic positions, site occupancies, thermal factors, and lattice distortions by fitting the experimental data to a calculated diffraction profile, allowing for a highly precise determination of the material's structural parameters.

Unlike powder X-ray diffraction (PXRD), which provides structural information by averaging over randomly oriented crystallites, Laue X-ray diffraction enables rapid determination of a crystal's orientation, symmetry, and structural integrity in a single exposure.

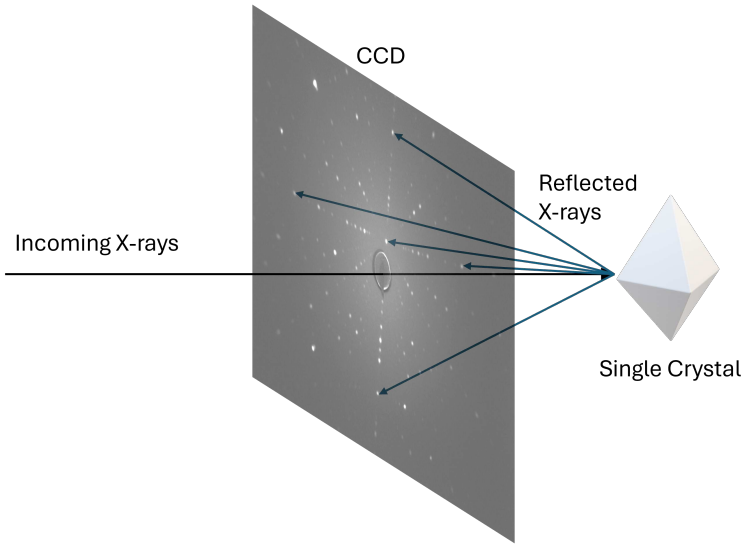

Figure 2.13: Schematic representation of single-crystal X-ray diffraction in the Laue geometry. Incoming X-rays are incident on a single crystal, generating a diffraction pattern that is captured by a charge-coupled device (CCD) detector. Each spot corresponds to a different crystallographic plane, enabling precise determination of the crystal's orientation.

This method relies on a broadband (polychromatic) X-ray beam, which allows multiple sets of crystallographic planes to satisfy the Bragg condition simultaneously, producing a characteristic pattern of discrete diffraction spots. Unlike conventional monochromatic X-ray diffraction, which requires scanning over different angles to capture diffraction peaks, Laue diffraction provides an instantaneous visualization of a crystal's structure without complex angular scans.

In this work, Laue diffraction was used both for crystal alignment and phase verification before further measurements. By comparing experimental diffraction patterns with calculated ones, we confirmed phase purity and ensured that only well-characterized, structurally consistent crystals were selected for subsequent experiments. The analysis of Laue patterns also provided insight into potential structural distortions, making it a valuable tool for sample alignment, quality control, and pre-characterization before neutron scattering or other experimental techniques.

Laue diffraction measurements were conducted using a Photonic Science Laue X-ray Camera, a backscattering system in which X-rays are generated by applying a set voltage

and current across a Cu source, producing a polychromatic spectrum. The beam is directed onto the sample, and backscattered diffraction patterns are captured by a high-resolution CCD camera (Fig. 2.13). Samples were mounted on a three-axis goniometer, which provided precise rotational control for alignment. For mechanically stable crystals, mounting was achieved using double-sided tape, putty, or CrystalBond wax. Once positioned, the sample was exposed to X-rays, and Laue images were collected to verify structural integrity and determine crystallographic orientation.

The diffraction images were analyzed using CLIP (Crystallographic Laue Indexing Program) [59], which indexed the observed diffraction peaks by assigning Miller indices and comparing the experimental pattern to simulated orientations. After an initial orientation determination, the crystal could be rotated toward the desired alignment. This process was iteratively refined, with successive diffraction images analyzed in real time, until the sample was aligned within 1-2 degrees (solid angle) of the target orientation.

The high sensitivity of Laue diffraction to crystalline perfection also enabled the identification of structural irregularities. Defects were readily apparent in the diffraction images and could be categorized based on distinct deviations from an ideal diffraction pattern. Twinning, in which multiple crystallographic domains coexist within a single sample, was observed as overlapping or multiple diffraction patterns in a single image. Impurities or structural distortions were identified by missing or extra diffraction peaks, indicating deviations from the expected crystal symmetry or the presence of a secondary phase. In cases of degradation or partial amorphization, peaks appeared broadened or diffuse, sometimes forming ring-like features, suggesting surface damage or loss of long-range crystalline order.

Once the crystal was properly aligned, it was transferred to the next experimental setup where precise orientation was required. This procedure ensured that samples used in further characterization techniques, such as neutron scattering or transport measurements, were aligned with high accuracy. The iterative refinement process enabled by Laue diffraction provided a straightforward yet powerful and rapid method for achieving high-precision crystal

alignment, which was critical for obtaining reliable data in subsequent experiments.

2.2.4 Magnetometry

Magnetometry is an essential experimental technique in magnetic condensed matter physics, providing a rapid and accurate means of characterizing magnetic properties. It encompasses a range of methods used to measure a sample's total magnetization (magnetic moment per unit volume), $\boldsymbol{M}$, and magnetic susceptibility (response function), χ. By systematically varying external parameters such as temperature, applied magnetic field, and crystallographic orientation, magnetometry reveals critical information about magnetic interactions, phase transitions, and collective phenomena. These measurements serve as a fundamental probe of a material's thermodynamic properties and can be fine-tuned to investigate the underlying magnetic Hamiltonian of a given system.

Theoretical Considerations

The total magnetization of a system with N magnetic moments, $\boldsymbol{\mu}_i$, is defined as

$$\mathbf{M} = \sum_{i=0}^{N} \boldsymbol{\mu}_i = N\langle \boldsymbol{\mu}_{\text{avg}} \rangle. \tag{2.19}$$

This quantity can be interpreted as the output of a system subjected to an applied magnetic field $\boldsymbol{H}$, governed by the response function χ, which can be written as

$$\boldsymbol{M} = \chi(T)\boldsymbol{H} \tag{2.20}$$

This relation holds in the linear response regime when the field energy is small compared to the magnetic interaction strength (e.g. $g\mu_B H \ll J$), otherwise we can write $\chi(T) = \partial \boldsymbol{M}/\partial \boldsymbol{H}$. While the linear response approximation provides a practical description of magnetization, a more fundamental approach derives M and χ from thermodynamic principles. In particular, these quantities are related to the Helmholtz free energy F as

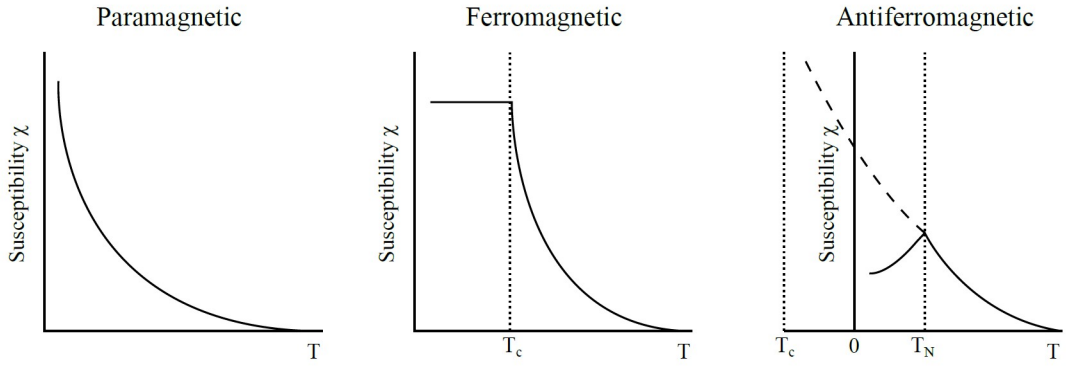

Figure 2.14: Adapted from Ref. [5], this figure illustrates the temperature dependence of magnetic susceptibility for paramagnetic, ferromagnetic, and antiferromagnetic materials. At high temperatures, all materials exhibit Curie-like paramagnetism ($\chi \propto 1/\mathrm{T}$), transitioning to different ordered states at lower temperatures.

$$M = -\left(\frac{\partial F}{\partial H}\right)_T, \tag{2.21}$$

$$\chi = -\left(\frac{\partial^2 F}{\partial H^2}\right)_T. \tag{2.22}$$

When moments respond to an applied field by aligning with that field, $\chi > 0$, we denote it as paramagnetic behavior. Conversely, when moments anti-align with the applied field, $\chi < 0$ and is denoted as diamagnetic behavior. When measured in a constant field, as a function of temperature, we can expect most magnetic materials to exhibit paramagnetic behavior at higher temperatures ($k_b T \gg J$), primarily because strong thermal fluctuations prevent effective interactions between magnetic moments. This is modelled by Curie's Law

$$\chi = \frac{C}{T}, \quad C = \frac{N g^2 \mu_B^2 J(J+1)}{3k_B} \tag{2.23}$$

where C here is known as the Curie constant, featuring the number of moments N, the Bohr magneton $\mu_B = \frac{e\hbar}{2m_e} \approx 0.0578$ meV/T, and the Boltzmann constant k_B. The Curie constant can often be fit to experimental paramagnetic data to extract information about the average g-value and angular momentum (J) attributed to each moment within the system. As the

temperature is lowered and thermal energy becomes comparable to the magnetic interaction energy ($k_BT \approx J$), non-interacting moments may become interacting and Curie's law is then shifted into the Curie-Weiss law, becoming

$$\chi = \frac{C}{T - Tc} \tag{2.24}$$

Below the transition temperature T_c (sometimes denoted as the Curie-Weiss temperature θ_{CW}), χ will diverge from Curie's law. Figure 2.14 shows the simplest cases of a system transitioning to either a ferromagnetic (FM) or antiferromagnetic (AF) state, where the moments spontaneously reconfigure to a favored alignment. In the FM case, all moments will become coaligned, thus saturating to a maximum total magnetization $M_{\mathrm{sat}} = Ng\mu_B J$. Within the Weiss mean-field theory, the transition temperature T_c is proportional to the effective exchange interaction strength J_{eff}, making it a useful experimental estimate of the dominant magnetic interaction energy[60, 5]. A positive θ_{CW} suggests net ferromagnetic interactions, while a negative value indicates antiferromagnetic coupling. In real materials, J_{eff} is often a combination of multiple exchange pathways, and competing interactions—such as nearest-neighbor vs. next-nearest-neighbor coupling—can lead to deviations from simple mean-field predictions. For the AF case, the observed transition temperature (denoted as the Néel temperature T_N) and the T_c fit to the Curie-Weiss law can be used to estimate the frustration parameter f, as discussed earlier in Section 2.1.2, Eq. 2.11.

While temperature-dependent magnetization measurements probe phase transitions and thermal effects, field-dependent measurements provide insight into the alignment of moments and saturation behavior. When measured at a constant temperature, as a function of applied magnetic field, we can expect materials in the paramagnetic with moments of angular momentum J regime to follow

$$M = Ng\mu_B J B_J(x) \tag{2.25}$$

where $B_J(x)$, the Brillouin function, is given by

$$B_J(x) = \frac{2J+1}{2J}\coth\left(\frac{(2J+1)x}{2J}\right) - \frac{1}{2J}\coth\left(\frac{x}{2J}\right) \tag{2.26}$$

with $x = \frac{gJ\mu_B B}{k_B T}$ representing the ratio of magnetic interaction energy to thermal energy. By fitting M(H) curves to the Brillouin function at different temperatures, the effective g_J value can be extracted, allowing for verification of the expected angular momentum states of the magnetic ions in the system. In the low-field limit ($x \ll 1$), $B_J(x)$ reduces to a linear response, recovering Curie's Law. In the high-field limit ($x \gg 1$), the magnetization asymptotically approaches the saturation value $M_{\text{sat}} = Ng\mu_B J$. However, in real materials, additional effects—such as anisotropic interactions, metamagnetic transitions, or dynamic magnetic effects can modify this behavior, necessitating a more detailed theoretical treatment. Such refinements include exchange interactions that drive collective magnetism, spin-orbit and crystal field couplings that induce anisotropic response, quantum effects that modify the saturation process, and frustration leading to nontrivial magnetization plateaus. In many cases, these effects require beyond-mean-field approaches such as perturbative statistical mechanical approaches, Monte Carlo simulations, or time-dependent simulations to fully describe the field-dependent behavior.

Additionally, the dependence of magnetization on crystallographic orientation provides a direct probe of anisotropy. The susceptibility, χ, and Landé g-factor, g, become tensorial quantities, meaning that magnetic response varies with applied field direction. This anisotropic response, arising from spin-orbit coupling and crystal field effects, manifests in direction-dependent susceptibility and magnetization behavior. By measuring χ(T) and M(H) along different crystallographic directions, one can extract key parameters governing magnetic anisotropy.

Experimental Considerations

Magnetization measurements were performed using the MPMS3 SQUID magnetometer

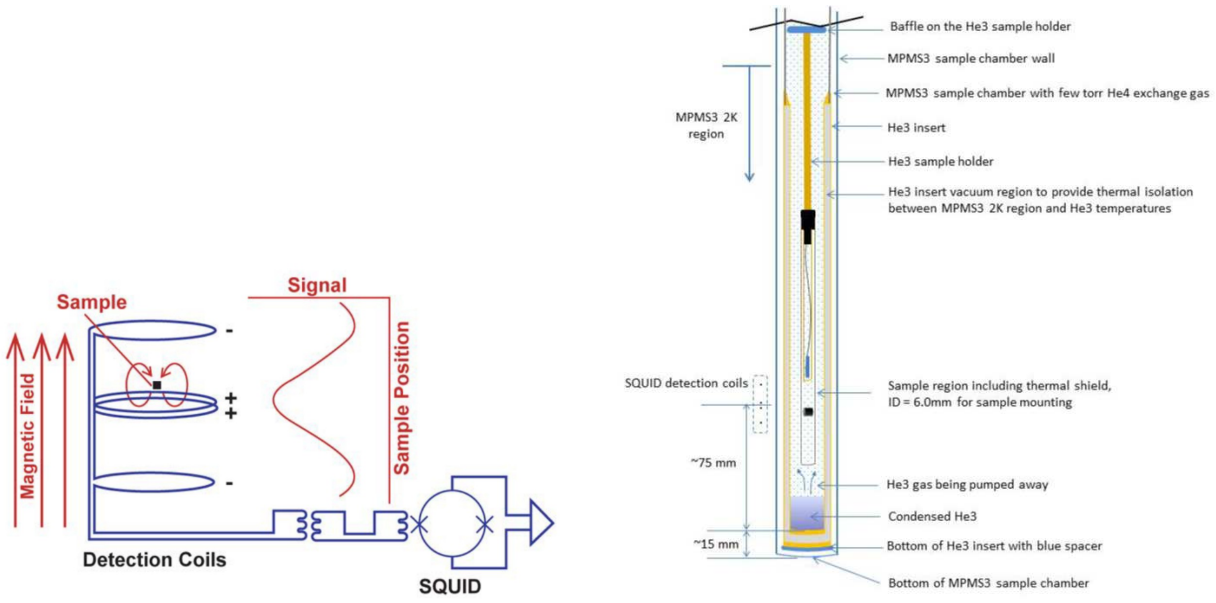

(a) (b)

Figure 2.15: (a) Schematic illustrating the MPMS detection principle, where a sample translated through detection coils induces a voltage amplified by a SQUID [6]. (b) Diagram of the iQuantum ^{3}He insert for MPMS3, enabling sub-kelvin measurements via evaporative cooling of condensed ^{3}He [7].

from Quantum Design. A Superconducting Quantum Interference Device (SQUID) is an ultrasensitive magnetometer that detects extremely small magnetic signals, with a sensitivity down to 10^{-8} emu. As illustrated in Figure 2.15a, the system operates by measuring the voltage induced in a set of detection coils as a magnetic sample is translated through them. The induced signal, proportional to the sample's magnetic moment, is processed by the SQUID circuit to determine the total magnetization. The MPMS3 was operated in both DC mode and Vibrating Sample Magnetometry (VSM) mode, enabling precise characterization of field- and temperature-dependent magnetization behavior.

For ultra-low-temperature measurements, the iQuantum ^{3}He insert was utilized. This system functions by condensing ^{3}He gas into a liquid and subsequently pumping on it with a turbomolecular pump, leveraging evaporative cooling to reach temperatures as low as 0.3 K (Fig. 2.15b). Unlike the base MPMS3 system, which can continuously vary temperature down to 1.8 K, the ^{3}He insert is a one-shot cooling system, meaning that once the liquid ^{3}He

is fully evaporated, re-cooling requires recondensing and evaporating the ^{3}He again [7]. This capability was particularly essential for this work, as many rare-earth compounds exhibit ultra-low magnetic transition temperatures. This arises from two primary factors: strong magnetic frustration, which prevents conventional ordering down to low temperatures, and weak exchange interactions due to the highly localized nature of $4f$ orbitals, which limits direct magnetic coupling between rare-earth ions. As a result, many of the materials studied in this work required sub- kelvin measurements to fully capture their ordering behavior.

Samples were mounted using various techniques depending on their physical properties and experimental requirements, ensuring they remained securely fixed during measurements to prevent torque effects caused by the applied magnetic field. Both powder and single-crystal samples were studied, with mounting strategies selected based on stability, alignment, and thermal contact considerations.

For powder samples, immobilization was achieved through pelletization, tight packing in a capsule, or embedding in a stabilizing medium such as eicosane or Stycast, which prevented particle movement and ensured reproducibility.

For single-crystal samples, precise alignment was critical due to their anisotropic magnetic properties. Laue diffraction was used to align each sample along the desired crystallographic axis, after which the crystals were mounted on quartz paddles using rubber glue or GE varnish. This provided a stable platform while ensuring minimal background signal during measurement.

For angular-dependent magnetization measurements, the MPMS3 rotating stage option was employed to precisely control the sample orientation within a fixed applied field. This stage enabled stepwise or continuous rotation, allowing measurements of the anisotropic magnetic response as the crystal's alignment relative to the applied field was systematically varied. To ensure accuracy, samples were pre-aligned using Laue diffraction and securely mounted with GE varnish, preventing any movement during rotation. The high angular resolution of the rotating stage allowed for detailed mapping of direction-dependent mag-

netization, making it an essential tool for studying crystallographic anisotropy in magnetic materials.

For ultra-low-temperature measurements using the ^{3}He option, samples were mounted in a sealed capsule, a straw, or a lower straw adapter, ensuring proper thermal contact while minimizing environmental interference. To achieve efficient cooling, the sample was positioned as close as possible to the system's thermometer, allowing accurate temperature tracking. Care had to be taken to avoid placing the sample too low in the probe, as this could result in submersion in liquid ^{3}He, which would severely reduce its evaporative cooling power and affect thermal equilibration. This setup ensured stable temperature control, reducing misalignment errors and improving the reproducibility of low-temperature magnetization measurements (Fig. 2.15b).

Temperature-dependent magnetization measurements were performed using the standard zero-field-cooled (ZFC) and field-cooled (FC) protocols. In the ZFC procedure, the sample was cooled to the base temperature in zero applied field, and magnetization was recorded while warming under a small applied field. In the FC procedure, the sample was cooled in a constant applied field, and magnetization was measured upon warming. These measurements provided insight into thermal effects on magnetic ordering and any irreversibilities associated with metastable states. Field-dependent magnetization measurements were conducted using a single- quadrant procedure (positive field ramp only, with no hysteresis loops), as the materials studied in this work exhibited negligible hysteresis. To ensure accurate data interpretation, background contributions from the sample holder were separately measured and subtracted from the total signal.

2.2.5 Heat capacity

Heat capacity provides a direct probe of phase transitions, excitations, and collective behaviors in condensed matter systems. In magnetic materials, anomalies in $C(T)$ reveal ordering transitions, field-induced phase changes, or quantum fluctuations. When combined

with neutron scattering and magnetization, this technique is an essential tool for studying complex magnetic interactions.

Theoretical Considerations

Heat capacity, denoted as C, is a fundamental thermodynamic quantity that characterizes the amount of heat required to change a system's temperature. For a system held at constant pressure P, the heat capacity is defined as

$$C_P = \left(\frac{dQ}{dT}\right)_P = -T\left(\frac{\partial^2 F}{\partial T^2}\right)_P \tag{2.27}$$

where dQ is the change in heat (non-work energy transferred into or out of the system), dT is the change in temperature, and F is the Helmholtz free energy of the system, defined as

$$F = U - TS \tag{2.28}$$

where U is the total internal energy of the system and S is the entropy [61, 62, 63]. In solids, particularly at low temperatures, $C_P \approx C_V$ since volume changes are negligible. (In general, the relation between C_P and C_V can be expressed in terms of the material's coefficient of thermal expansion α and isothermal compressibility κ_T, and is more rigorously written as $C_P = C_V + \frac{TV\alpha^2}{\kappa_T}$.) By normalizing this quantity to either the number of moles or the mass of a sample, we can define the specific heat, denoted as c.

In general, heat capacity measurements capture contributions from three primary sources: phononic (lattice vibrations), electronic, and magnetic. At temperatures above 1K, phonons typically dominate the total heat capacity. However, since we are primarily interested in contributions from the other two, it is often necessary to subtract the phonon signal. To model the phonon contribution in three dimensions, we employ the Debye approximation

$$C_V \sim \left(\frac{T}{\theta_D}\right)^3 \quad or \quad C_V \approx \left(\frac{k_B}{\hbar v_s}\right)\frac{V}{6\pi^2 N}T^3 \tag{2.29}$$

where θ_D is the Debye temperature, which represents the characteristic temperature above which phonons can no longer propagate, v_s is the speed of sound in the material, N is the number of atoms, and V is the sample volume. The Debye model is valid for $T \ll \theta_D$, while at higher temperatures, C_V asymptotically approaches the classical limit of $3Nk_B$ (the Dulong-Petit law) [60, 5]. While this phonon contribution can be estimated analytically if v_s is known, a more practical approach is to measure the heat capacity in a non-magnetic analogue with an identical lattice structure. Since phonons correspond to quantized lattice vibrations, this allows for an empirical determination of the phonon contribution, which can then be subtracted from the total heat capacity.

In addition to phonons, electronic degrees of freedom contribute to the total heat capacity by providing additional channels for heat absorption. In metals, this arises from conduction electrons, which can absorb energy by transitioning to higher energy states near the Fermi level. However, in insulating systems, this contribution is negligible.

A more relevant electronic contribution in rare-earth systems comes from the thermal population of discrete energy levels due to crystal field splitting (discussed in Section 2.1.3). When a material has well- separated, low-energy electronic states with a gap of Δ, as temperature increases, thermal population of higher-energy states increases, altering the system's entropy and leading to a Schottky anomaly—a broad peak in $C(T)$ centered around $T \sim \Delta/k_B$. At sufficiently low temperatures, a nuclear Schottky anomaly can also emerge due to hyperfine interactions. When k_BT becomes comparable to the hyperfine energy gap, nuclear spin states begin to thermally populate, producing an additional low-temperature peak in $C(T)$. This contribution typically appears in the millikelvin range and can dominate the heat capacity at ultralow temperatures [64].

The entropy change associated with these thermal excitations is quantified by the statistical definition

$$\Delta S = R \ln(\Omega) \tag{2.30}$$

where Ω is the number of available microstates. For a two-level system, such as an effective spin-1/2 system, we expect Ω=2, leading to the characteristic entropy plateau at $\Delta S = R\ln(2)$ in the high-temperature limit. While this statistical formula provides insight into the available microstates, entropy changes can also be directly measured by numerically integrating the heat capacity

$$\Delta S = \int \frac{C}{T} dT \tag{2.31}$$

For spin-1/2 systems, this integration should asymptotically approach $R\ln(2)$, verifying that the heat capacity captures all relevant degrees of freedom. This serves as a consistency check against potential errors such as incomplete thermalization or background contributions. Additionally, entropy recovery across phase transitions provides insights into the degree of ordering and collective excitations in the system.

Magnetic contributions to heat capacity arise from the thermal excitations of spin degrees of freedom. In systems with localized magnetic moments, the nature of these excitations depends on exchange interactions, anisotropies, and external fields. Unlike phonon or electronic contributions, which typically follow smooth trends, magnetic heat capacity often exhibits sharp anomalies associated with phase transitions, as well as broader features due to collective spin fluctuations.

A key feature in many magnetic systems is the presence of a lambda anomaly, indicative of a second-order phase transition to long-range magnetic order at the Néel (antiferromagnetic) or Curie (ferromagnetic) temperature [65]. At a phase transition, the second derivative of the Helmholtz free energy, which defines the heat capacity (Eq. 2.27), exhibits a singularity. In C_P measurements, this results in a curve looking like the "λ" symbol, hence the name.

At the transition temperature, symmetry breaking occurs, and the system moves from a disordered to an ordered state, minimizing F. The specific nature of the anomaly depends on the universality class of the transition, with critical fluctuations modifying the scaling behavior of heat capacity near T_c. Near a second-order phase transition, fluctuations in the

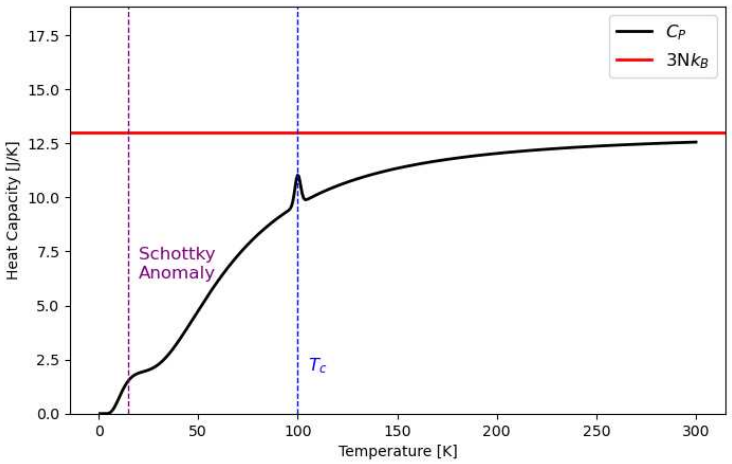

Figure 2.16: A synthetic example of C_P data illustrating key heat capacity features: T^3 dependence (Debye approximation) at intermediate temperatures, saturation to $3Nk_B$ (Dulong-Petit Law), a lambda anomaly at T_C=100K—marking a phase transition to an ordered state, and a Schottky anomaly at 15K—corresponding to a low-lying CEF energy gap of approximately $\Delta \sim 1.3$meV.

order parameter become long-ranged, leading to diverging correlation lengths. This results in a singularity in the heat capacity, which follows a power-law scaling characterized by the exponent α

$$C_{\text{mag}} \sim |T - T_c|^{-\alpha} \tag{2.32}$$

The exponent α is determined by the system's dimensionality and interaction type, following universality class predictions [66, 67]. Systems belonging to the same universality class share identical critical exponents, despite differences in microscopic details. The values of these exponents depend only on symmetries and dimensionality, not the specific interactions at the atomic level. For example, in the 3D Ising model, $\alpha \approx 0.11$, while for the 2D Ising model, the heat capacity exhibits a logarithmic divergence ($\alpha = 0$). Universality extends beyond magnetism, with systems as varied as liquid-gas transitions, percolation theory, and even cosmological phase transitions near the early universe following similar scaling laws [68, 69, 70].

Even in systems that do not order magnetically, short-range spin correlations contribute

to heat capacity. These correlations can give rise to broad peaks in $C(T)$, distinct from the sharper anomalies of long- range ordering. Such features are often seen in geometrically frustrated systems, where competing interactions prevent conventional ordering down to very low temperatures.

The interplay between phonon, electronic, and magnetic contributions makes heat capacity a powerful tool for characterizing quantum materials. By isolating and analyzing these components, we can extract key insights into spin interactions, phase transitions, and emergent quantum effects.

Experimental Considerations

Heat capacity measurements were performed using the Heat Capacity option for Quantum Design PPMS (Physical Property Measurement System), which employs a heat-pulse relaxation method to determine specific heat. In this technique, a known heat pulse is applied to the sample through a resistive heater, and the resulting temperature rise and subsequent thermal relaxation are recorded. The heat capacity is extracted by fitting the temperature decay curve to an exponential model, allowing for precise determination of the sample's heat capacity, with a typical resolution on the order of 0.1μJ/K at 2K. This method is highly effective for obtaining temperature- and field-dependent heat capacity data over a broad range, with automated measurement sequences ensuring high reproducibility.

To access ultralow temperatures, as is often needed when studying rare-earth ions due to the localized $4f$ orbitals, relatively small exchange interactions, frustration discussed previously in Section 2.1, we employed the PPMS dilution refrigerator (DR) option (Fig. 2.17a), which enables measurements down to 50 mK. The DR operates using a ^{3}He-^{4}He mixture, which phase-separates below 870 mK into a concentrated phase (nearly pure ^{3}He) and a dilute phase (mostly ^{4}He with $\sim$6% ^{3}He). Cooling occurs at the phase boundary in the mixing chamber, where ^{3}He atoms transition into the dilute phase, absorbing heat in the process. A continuous circulation cycle is maintained by the still, held at 0.6 K by a turbo pump, which

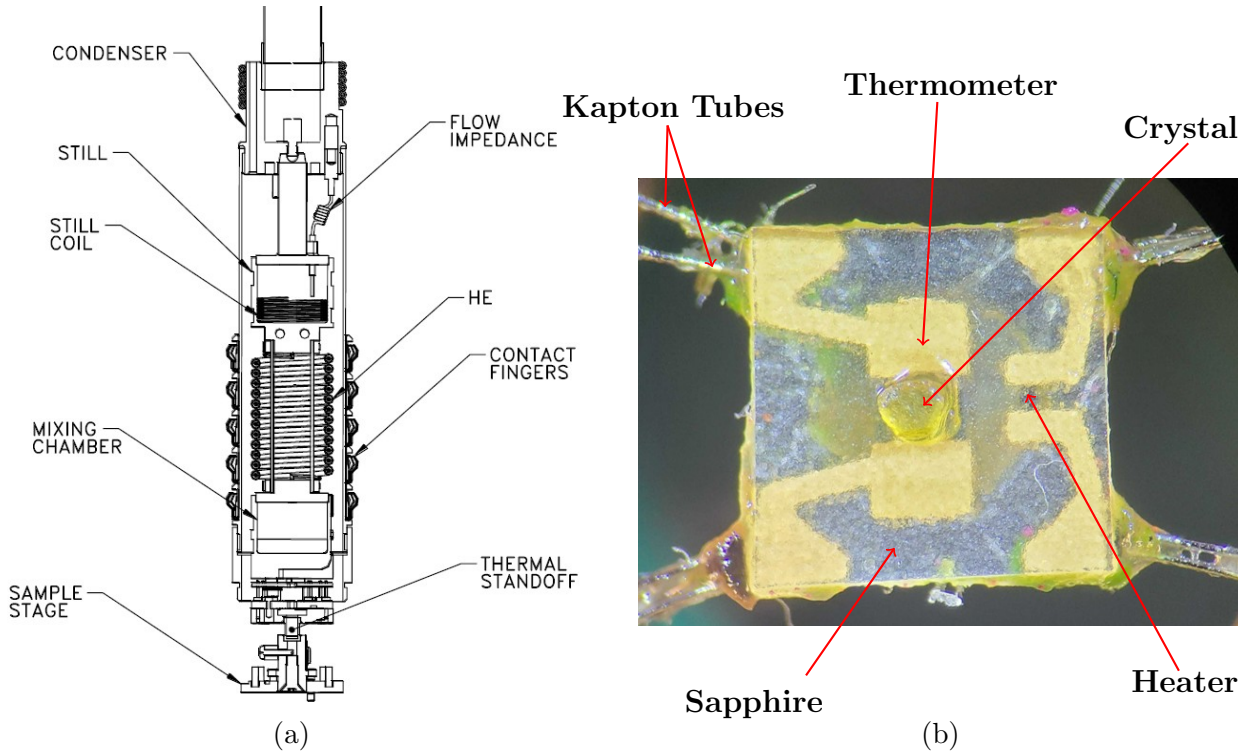

Figure 2.17: (a) Diagram of Quantum Design Dilution Refrigerator probe layout, adapted from Ref.[8]. This schematic illustrates key components including the mixing chamber, still, condenser, and sample stage, where the heat capacity puck can be mounted in thermal contact with the mixing chamber. (b) An annotated optical image of a mounted $Ce_2Sn_2O_7$ crystal on the sapphire stage within the heat capacity puck, highlighting the Kapton tubes, sapphire stage, crystal, thermometer, and heater.

selectively evaporates ^{3}He, reducing its concentration and driving osmotic flow from the mixing chamber. The extracted ^{3}He gas is re-condensed in the condenser, thermally anchored to the PPMS sample chamber. The liquid ^{3}He then flows through a flow impedance, precools via the counterflow heat exchanger (HE), and returns to the mixing chamber, completing the cycle. This technique provides stable temperature control well below the typical PPMS base temperature of 1.8 K.

Samples were mounted on the PPMS heat capacity puck, which consists of a sapphire stage suspended in vacuum with Kapton tubes and an integrated resistive heater and thermometer (Fig. 2.17b). The high thermal conductivity of sapphire ensures rapid thermal equilibration between the sample and the platform, minimizing temperature gradients and improving measurement accuracy. To ensure optimal thermal contact, a thin layer of Apiezon

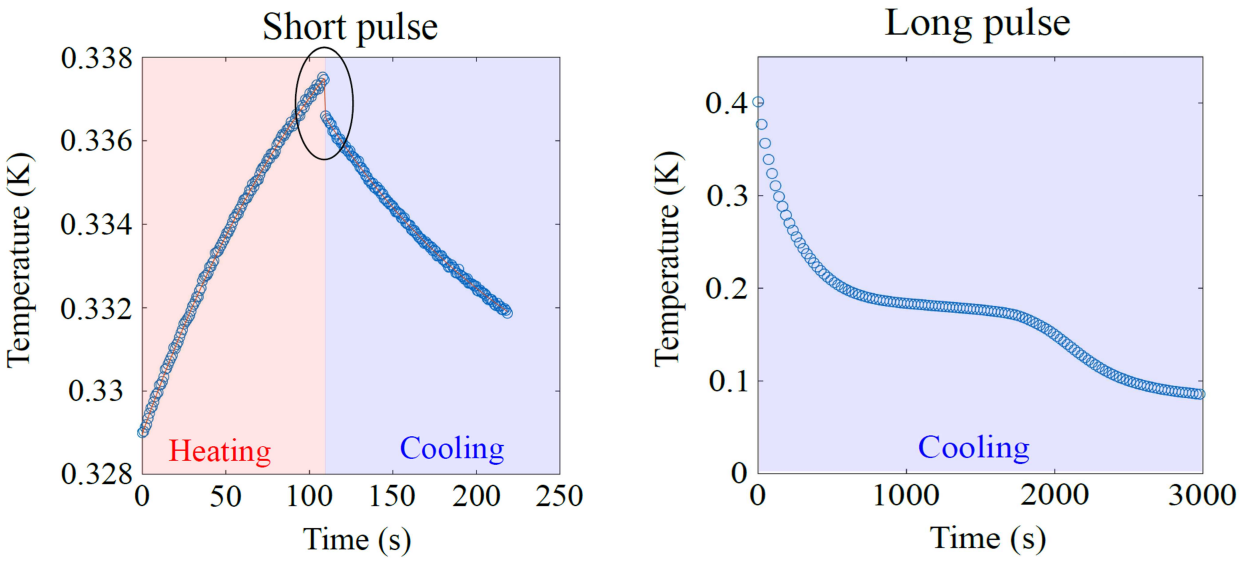

(a) (b)

Figure 2.18: Adapted from Ref.[9], a comparison of short-pulse and long-pulse heat capacity measurements, performed at each temperature set point. (a) In the short-pulse method, rapid heating (red) is followed by cooling (blue). The circled jump arises from the heat capacity of the grease, which has a faster thermal decay than the sample. (b) In the long-pulse method, gradual heating allows full equilibration before cooling, improving accuracy but requiring longer measurement times. A decay curve is fit to both the warming and cooling segments, generating a single data point in $C(T)$.

N-grease was applied between the sample and the sapphire stage [71]. This grease was chosen for its excellent thermal conductivity at cryogenic temperatures while introducing minimal background signal.

Whenever possible, single-crystal samples were crystallographically oriented using Laue diffraction prior to mounting. This ensured that heat capacity measurements were performed with the sample aligned along the intended crystallographic axis, improving consistency across experiments.

Short-pulse and long-pulse techniques offer complementary advantages. The short-pulse method is faster but more prone to thermal lag, whereas the long-pulse method ensures better equilibration but requires extended measurement times. In the short-pulse method (Fig. 2.18a), a brief heat pulse is applied, and the initial rapid relaxation is analyzed. This method is well-suited for samples with small heat capacities, as it prevents excessive heating

and enables faster data acquisition. However, it is more susceptible to thermal lag effects, which can introduce errors in larger heat capacity materials.

In contrast, the long-pulse method (Fig. 2.18b) involves applying a more extended heat pulse, ensuring full equilibration before cooling begins. This technique is advantageous for samples with higher heat capacities or broad heat capacity features, such as phase transitions. While more accurate in such cases, the long-pulse approach is more prone to excess heating artifacts, particularly near low-temperature transitions, where thermal dissipation is slower.

To accurately extract sample heat capacity, background subtraction was performed to remove addenda contributions from the platform and grease. This was achieved by separately measuring the heat capacity of the sapphire stage and grease alone under identical experimental conditions. The resulting addenda contribution was then subtracted from the total measured heat capacity, ensuring that only the intrinsic properties of the sample were analyzed.

Heat capacity values were extracted by fitting relaxation curves to exponential decay models. Additional background corrections were applied by estimating the phonon contribution via Debye model fits or through comparison with measurements of a non-magnetic structural analogue.

Error analysis was conducted to account for potential sources of uncertainty, including thermal contact resistance, addenda corrections, and relaxation fitting errors. The reliability of measurements was further validated through multiple trials, reproducibility checks, and/or comparison with literature when possible—ensuring that observed features in heat capacity were intrinsic to the sample rather than artifacts of the measurement process.

This methodology allows for highly precise and reproducible heat capacity measurements across a wide temperature range, from room temperature down to ultralow millikelvin regimes. By carefully considering sample preparation, measurement techniques, and data correction procedures, we ensure that the extracted heat capacity data accurately reflect the intrinsic thermodynamic properties of the studied materials.

2.2.6 Neutron Scattering

Neutron scattering stands among the most powerful and versatile techniques for exploring both the structural and magnetic properties of condensed matter systems. Its unique capabilities originate from several fundamental properties of the neutron. Most notably, neutrons carry no net electric charge, so they undergo only weak nuclear interactions and can penetrate deeply into a sample, providing information about the bulk rather than just the near-surface region. In addition, neutrons have spin 1/2 and thus a magnetic dipole moment, allowing them to couple directly to unpaired electron spins—a critical advantage for probing magnetism. Crucially, their energies and wavelengths can be tuned over an exceptionally broad range: from around 0.1 meV (with a corresponding wavelength of 3 nm) in cold neutron beams up to 500 meV (with wavelengths near 0.4 Å) in hot neutron beams. This spread neatly encompasses both atomic length scales and relevant magnetic energy scales in solids, making neutrons extremely sensitive to lattice vibrations, spin waves, and other excitations relevant to this work. Moreover, specialized neutron instruments can be designed to harness these broad intrinsic possibilities, extending the accessible range of energies and length scales for different experiments (see Fig. 2.19).

Neutron scattering also benefits from isotopic sensitivity—different isotopes of the same element can scatter neutrons with markedly distinct cross sections. This feature allows for "contrast variation" experiments in which particular components of a multi-phase system can be highlighted or suppressed. For instance, in biological or polymeric samples, selectively substituting hydrogen with deuterium can render specific domains or molecules "visible" in the scattering pattern, revealing structural or dynamic features otherwise obscured. By comparison, X-ray photons and electron beams both interact primarily with the electronic structure of the material; they can offer rapid data collection, chemical specificity, and high spatial resolution, but typically have shallower penetration depths and limited direct sensitivity to spin degrees of freedom. Consequently, these techniques complement neutrons in a broader suite of scattering methods used in modern materials research.

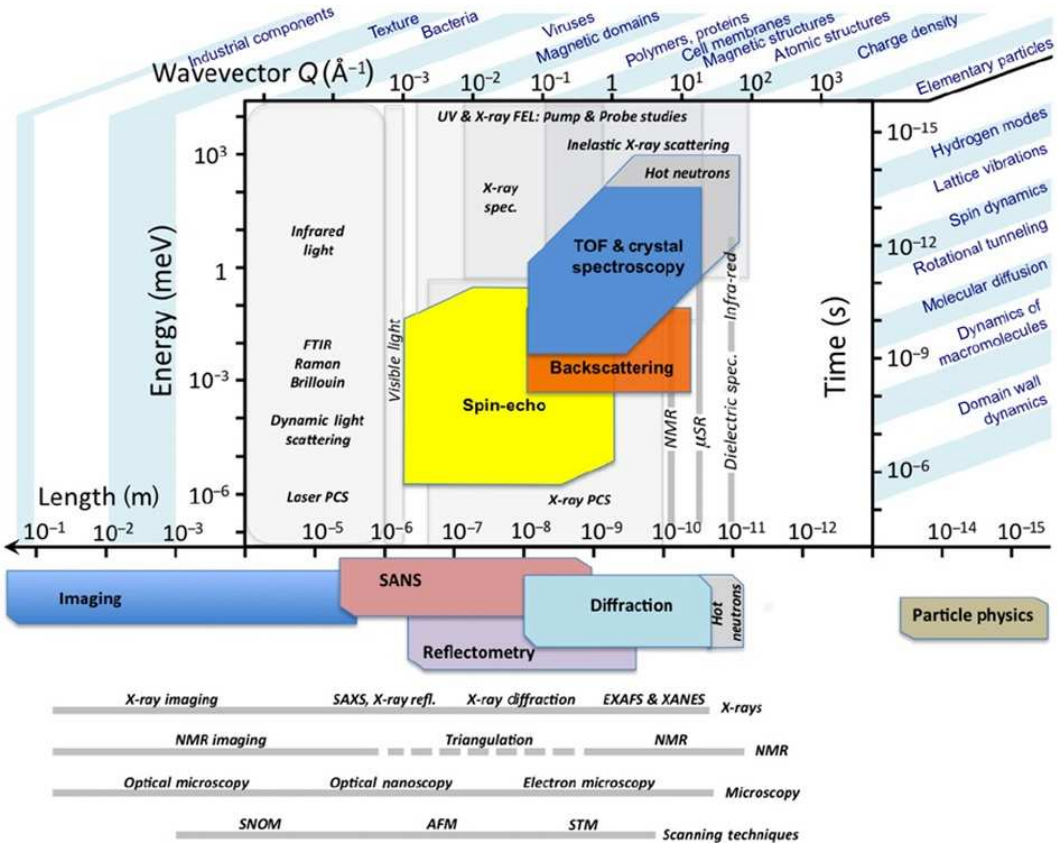

Figure 2.19: Time and wavelengths accessible via neutrons and comparison with other experimental techniques, adapted from Ref.[10]. This diagram reinforces how versatile neutron scattering is for investigating an incredible range of phenomena—from fundamental physics at atomic length scales to bulk imaging of industrial components.

Rare-earth magnets, in particular, provide an ideal testing ground for these capabilities. Their $4f$ electrons are strongly localized and experience large spin-orbit coupling, often giving rise to the anisotropic exchange or bond-dependent interactions implicated in a range of unconventional magnetic phases. By leveraging neutron scattering to measure magnetic Bragg peaks, refine ordered moment sizes, and map dispersing spin excitations, researchers can pinpoint the microscopic parameters—exchange constants, anisotropy terms, and critical fields—that underlie exotic behavior. Critically, many rare-earth driven interactions lie in the meV range, making cold or thermal neutron beams a natural match for probing these collective modes at low temperatures and under applied fields. In essence, the synergy between rare-earth physics and neutron- based experimental techniques opens a clear route

to unraveling the fundamental quantum magnetism at play.

In this section, we will first summarize the theoretical framework of neutron scattering, focusing on the roles of nuclear and magnetic interactions in both elastic and inelastic processes as they pertain to this work. The discussion will then progress to key experimental concepts: momentum transfer, energy transfer, and how different spectrometer configurations are used to address structural versus dynamical questions. Finally, we delve into the specific neutron methods employed in this dissertation to investigate rare-earth magnetism, highlighting the unique challenges posed by air-sensitive samples and the specialized instrumentation needed to maintain an inert environment throughout the measurement process. By weaving together these theoretical, technical, and practical elements, we set the stage for a detailed analysis of our neutron scattering results in rare-earth quantum magnets.

Theoretical Considerations

Neutron scattering experiments are analyzed within the geometry depicted in Fig. 2.20, where incoming neutrons with mass m and momentum $\hbar\boldsymbol{k}_i$ are scattered into a solid angle $d\Omega$ by a scattering potential (sample), acquiring a final momentum $\hbar\boldsymbol{k}_f$. Their incident and final energies are given by

$$E_i = \frac{\hbar^2 \boldsymbol{k}_i^2}{2m} \quad , \quad E_f = \frac{\hbar^2 \boldsymbol{k}_f^2}{2m} \tag{2.33}$$

The scattering process is classified as elastic if $E_i = E_f$ and inelastic if $E_i \neq E_f$. The difference between the final and initial wavevectors is known as the scattering vector, while the difference between the final and initial energies is referred to as the energy transfer:

$$\boldsymbol{Q} = \boldsymbol{k}_f - \boldsymbol{k}_i \quad , \quad \hbar\omega = E_f - E_i \tag{2.34}$$

Here, $\hbar\boldsymbol{Q}$ represents the momentum imparted to (or absorbed from) the sample by the neutron, and $\hbar\omega$ denotes the energy transfer. It is common practice to omit the $\hbar$ for

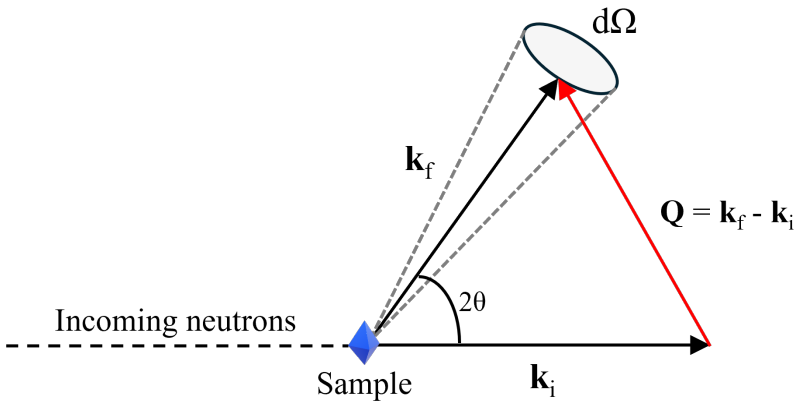

Figure 2.20: Schematic representation of neutron scattering geometry. An incident neutron with wavevector $\boldsymbol{k}_i$ interacts with the sample and scatters into a final state with wavevector $\boldsymbol{k}_f$, forming a scattering angle 2θ. The momentum transfer is given by $\boldsymbol{Q} = \boldsymbol{k}_f - \boldsymbol{k}_i$. The scattered intensity is measured over a solid angle $d\Omega$.

brevity. During a measurement, detectors positioned around the sample count the number of neutrons scattered per second into the solid angle $d\Omega$ in a given direction, with a final energy resolution spanning E_f to some dE_f. This measurable quantity is the double differential scattering cross-section, expressed as

$$\frac{d^2\sigma}{d\Omega dE_f} = \frac{k_f}{k_i} S(\boldsymbol{Q}, \omega) \tag{2.35}$$

where $S(\boldsymbol{Q}, \omega)$ is the dynamic structure factor, which encapsulates the spatial and temporal correlations of the scattering centers. The dynamic structure factor can be derived using utilizing the Born Approximation and Fermi's Golden Rule. The former assumes that both incoming and scattered neutron waves are plane waves.[11] The latter states that the transition probability between initial and final states is proportional to the squared matrix element of the interaction potential V. Explicitly,

$$S(\boldsymbol{Q}, \omega) = \left(\frac{m}{2\pi\hbar^2}\right)^2 \sum_{\lambda_i} p_{\lambda_i} \sum_{\lambda_f} |\langle \sigma_f \lambda_f | V(\boldsymbol{Q}) | \sigma_i \lambda_i \rangle|^2 \delta(E_{\lambda_f} - E_{\lambda_i} - \hbar\omega) \tag{2.36}$$

[11] In reality, neutrons are scattered into spherical wave states, but the distinction between plane and spherical waves become negligible at large distances—which makes this approximation applicable in typical neutron scattering experiments.

A complete derivation of the dynamic structure factor (and the subsequent reformulations that we will present here) can be found in Refs. [72, 73, 74]. However, its key components can be understood as follows: The prefactor ensures proper normalization and unit consistency. The summation over initial states, weighted by their Boltzmann probability p_{λ_i}, accounts for the statistical distribution of sample states at thermal equilibrium. The quantum labels λ_i and λ_f correspond to the eigenstates of the sample before and after scattering, respectively, while σ_i and σ_f denote the neutron's initial and final spin states. The squared matrix element $|\langle\sigma_f\lambda_f|V(\boldsymbol{Q})|\sigma_i\lambda_i\rangle|^2$ represents the probability amplitude for the combined neutron-sample system to transition from the initial state $|\sigma_i\lambda_i\rangle$ to the final state $|\sigma_f\lambda_f\rangle$ due to interaction with the scattering potential $V(\boldsymbol{Q})$, which is the Fourier transform of the real-space potential $V(\boldsymbol{r})$. This term encapsulates both nuclear and magnetic contributions, determining how neutrons interact with the sample. Finally, the delta function enforces energy conservation, ensuring that the energy lost or gained by the neutron precisely matches the energy transferred to or from the sample.

As a quick aside—if the sample were a purely rigid structure, meaning there were no internal degrees of freedom capable of absorbing or emitting energy, the system's initial and final states would necessarily be the same, i.e., $\lambda_i = \lambda_f$. In this case, the energy-conserving delta function simplifies to

$$\delta(E_{\lambda_f} - E_{\lambda_i} - \hbar\omega) = \delta(\hbar\omega) \tag{2.37}$$

This implies that energy transfer is strictly zero, meaning that the double differential scattering cross-section in Eq. 2.35 is only nonzero for $E_i = E_f$, corresponding to purely elastic scattering. Furthermore, in this limit, the sum over sample states simplifies as well: since the system remains unchanged, the sum over p_{λ_i} trivially satisfies $\sum_{\lambda_i} p_{\lambda_i} = 1$, and the squared matrix element reduces to a transition probability that depends only on the neutron spin states σ_i and σ_f. Physically, this result aligns with the expectation that an ideal rigid structure would only scatter neutrons elastically, preserving their incident energy. However, even

in elastic scattering, the observed intensity depends on whether phase relationships between scattered waves are preserved (coherent) or lost (incoherent).

Elastic scattering arises from the interference of neutron waves scattered from different sites within the sample. If the scattering centers are well-ordered and phase relationships between different scattering sites are preserved, we obtain coherent scattering, which produces Bragg peaks in diffraction experiments and provides direct information about long-range crystalline order. Coherent scattering is also responsible for detecting collective excitations, such as phonons and magnons, in inelastic neutron scattering.

In contrast, incoherent scattering occurs when the neutron interacts in a way that varies randomly from one site to another—such as due to isotope disorder or the random orientations of nuclear spins. Because phase relationships are lost, incoherent scattering lacks interference effects and does not contribute to Bragg peaks or long-range order. Instead, it appears as a diffuse background that is spread uniformly in all directions, as there is no constructive interference to focus intensity at specific Q values. However, incoherent scattering is valuable for studying local fluctuations, such as atomic diffusion, paramagnetic fluctuations, and single-particle motion.

Thus, coherent elastic scattering reveals structural and long-range order, while incoherent elastic scattering primarily probes local disorder and stochastic fluctuations. Since both coherent and incoherent processes contribute to the total elastic intensity, their combined effect is accounted for by integrating over all final energies, yielding the single differential scattering cross-section.

$$\begin{aligned} \frac{d\sigma}{d\Omega} &= \int \frac{d^2\sigma}{d\Omega dE_f} dE_f \\ &= \left(\frac{m}{2\pi\hbar^2}\right)^2 |\langle \sigma_f | V(\boldsymbol{Q}) | \sigma_i \rangle|^2 \end{aligned} \tag{2.38}$$

Thus, we have arrived at the measurable quantity used in elastic neutron scattering, which serves as a fundamental tool for structural characterization in its broadest sense. While commonly associated with atomic structure determination, elastic neutron scattering also

provides insight into crystallographic order, magnetic structures, lattice distortions, and the spatial distribution of light elements, making it invaluable for studying both ordered and disordered materials. However, if the sample can undergo internal transitions, meaning $\lambda_i \neq \lambda_f$, then inelastic scattering processes contribute as well. In this more general case, we return to the full Eq. 2.35, where the total scattering intensity contains both elastic and inelastic components. Among the various inelastic processes that neutrons can probe, two important examples are lattice vibrations (phonons) and crystal electric field (CEF) excitations, which provide insight into both structural and electronic properties.

A key class of inelastic scattering processes involves the excitation of lattice vibrations (phonons) and electronic crystal field (CEF) transitions. These excitations appear as distinct energy losses (or gains) in neutron spectra, providing insight into lattice dynamics and electronic structure. Phonons, which are quantized lattice vibrations, are excited or absorbed by neutrons through interactions with atomic nuclei. This results in inelastic peaks in $S(\boldsymbol{Q}, \omega)$, symmetrically positioned around the elastic line (ω=0) due to both phonon creation and annihilation. Their intensity follows the detailed balance principle, meaning phonon absorption becomes more probable at higher temperatures. Since phonons are collective excitations, coherent scattering is required to observe well-defined phonon dispersions in energy- momentum space.

In materials containing magnetic ions, the surrounding crystal field lifts the degeneracy of electronic states, creating discrete CEF levels. Neutrons can induce transitions between these states, producing sharp, non-dispersive inelastic peaks in neutron spectra. Unlike phonons, which disperse with momentum transfer, CEF excitations remain localized and depend on the symmetry of the crystal environment. Their intensity follows the magnetic form factor, meaning they are strongest at low Q values. Both phonon and CEF excitations contribute directly to the dynamic structure factor, reinforcing the fundamental role of correlation functions in neutron scattering.

While the structure factor encodes spatial correlations, it also provides insight into the

temporal fluctuations of the system. Since neutron scattering is sensitive to dynamical processes, it is natural to reformulate $S(\boldsymbol{Q},\omega)$ in terms of time-dependent correlation functions. A key observation is that this constraint can be rewritten in an integral form as

$$\delta(E_{\lambda_f} - E_{\lambda_i} - \hbar\omega) = \frac{1}{2\pi\hbar}\int_{-\infty}^{\infty} e^{i(E_{\lambda_f} - E_{\lambda_i} - \hbar\omega)t/\hbar} dt \tag{2.39}$$

This formulation makes explicit the underlying time dependence of the scattering process, demonstrating how neutron interactions probe dynamical correlations in the sample. A more natural way to describe this evolution is through the Heisenberg picture, where operators evolve in time according to

$$\hat{A}(t) = e^{i\hat{H}t/\hbar}\hat{A}(0)e^{-i\hat{H}t/\hbar} \tag{2.40}$$

where $\hat{H}$ is the Hamiltonian operator of the system. Using this, we can define a time-dependent scattering operator

$$\hat{A}(\boldsymbol{Q},t) = \left(\frac{m}{2\pi\hbar^2}\right)\langle k_f,\sigma_f,\lambda_f|\hat{V}(\boldsymbol{Q},t)|k_i,\sigma_i,\lambda_i\rangle \tag{2.41}$$

where $\hat{A}(\boldsymbol{Q},t)$ and $\hat{V}(\boldsymbol{Q},t)$ are now Heisenberg operators, evolving in time governed by the Hamiltonian of the scattering system. By inserting the integral form of the delta function into Eq. 2.36 and rewriting $S(\boldsymbol{Q},\omega)$ in terms of $\hat{A}$, the summation over initial and final states naturally reorganizes into an expectation value (a thermal ensemble) of these time-dependent operators. This follows from the completeness of eigenstates and the time evolution of operators in the Heisenberg picture, leading to a double differential scattering cross section of

$$\begin{aligned}\frac{d^2\sigma}{d\Omega dE_f} &= \frac{k_f}{k_i}S(\boldsymbol{Q},\omega) \\ &= \frac{k_f}{k_i}\left(\frac{1}{2\pi\hbar}\right)\int_{-\infty}^{\infty}\langle\hat{A}^\dagger(\boldsymbol{Q},0)\hat{A}(\boldsymbol{Q},t)\rangle e^{-i\omega t}dt\end{aligned} \tag{2.42}$$

Thus, we see that neutron scattering directly measures the Fourier transform of a time-dependent correlation function $\langle \hat{A}^\dagger(\boldsymbol{Q}, 0)\hat{A}(\boldsymbol{Q}, t)\rangle$, encoding both spatial and temporal correlations of the scattering centers. Correlation functions are fundamental in physics because they quantify how a physical quantity at one time is related to its value at a later time. In nuclear scattering, for example, the dynamic structure factor describes density-density correlations, given by

$$G_{\text{nuc}}(\boldsymbol{r}, t) = \langle \rho(\boldsymbol{r}, t)\rho(0, 0)\rangle \tag{2.43}$$

where $\rho(\boldsymbol{r}, t)$ represents the local atomic density operator. These correlations determine how atomic positions fluctuate in space and time, providing insight into both crystal structures (via elastic scattering) and lattice vibrations (via inelastic scattering). In thermal equilibrium, the time dependence we measure corresponds to the spectrum of thermal and quantum fluctuations of the atomic density field.

While nuclear scattering provides insight into atomic positions and lattice vibrations, many materials also host magnetic moments that give rise to spin correlations, introducing an entirely different class of scattering processes. Since neutrons possess an intrinsic spin of S_n=1/2 and an associated magnetic dipole moment, they can couple to unpaired electronic spins in a sample via the dipole-dipole interaction (Eq. 2.2). This makes neutron scattering a powerful probe of spin-spin correlation functions, analogous to how nuclear scattering probes density correlations.

The scattering operator $\hat{A}(\boldsymbol{Q}, t)$ introduced previously takes on a different physical meaning in the case of magnetic scattering. Instead of representing the nuclear scattering potential, it corresponds to the spin density operator

$$\hat{A}(\boldsymbol{Q}, t) = \sum_j e^{i\boldsymbol{Q}\cdot\boldsymbol{r}_j}\hat{S}_j^\alpha(t) \tag{2.44}$$

where $\hat{S}_j^\alpha(t)$ represents the α-component (i.e. $\alpha \in \{x, y, z\}$) of the spin operator at site

j, evolving in the Heisenberg picture. Substituting this into the dynamic structure factor formulation gives the magnetic structure factor

$$S^{\alpha\beta}_{\text{mag}}(\boldsymbol{Q},\omega) = \frac{1}{2\pi}\int_{-\infty}^{\infty}\sum_{j,k}\langle S^{\alpha}_{j}(0)S^{\beta}_{k}(t)\rangle e^{i\boldsymbol{Q}\cdot(\boldsymbol{r}_j-\boldsymbol{r}_k)}e^{-i\omega t}dt \tag{2.45}$$

This function describes how neutron scattering probes spin fluctuations in a sample, providing direct insight into both static spin order (e.g., magnetic Bragg peaks in ordered phases) and dynamical excitations (e.g., spin waves).

Unlike nuclear scattering, magnetic scattering intensity is modulated by the perpendicular component of magnetic form factor $F_{\perp}(\boldsymbol{Q})$, which accounts for the spatial extent of the electron wavefunction and the projection of spin fluctuations perpendicular to the scattering vector $\boldsymbol{Q}$

$$\frac{d^2\sigma}{d\Omega dE_f} \propto |F_{\perp}(\boldsymbol{Q})|^2 S^{\alpha\beta}_{\text{mag}}(\boldsymbol{Q},\omega) \tag{2.46}$$

Since electron orbitals are spatially extended, magnetic scattering intensity decreases at high Q, distinguishing it from nuclear scattering, which arises from nearly point-like nuclei. This falloff is an important experimental signature that helps separate magnetic from nuclear contributions.

Furthermore, neutron scattering allows for the direct study of collective spin excitations in ordered magnetic materials. In magnetically ordered systems, small deviations from the ground state propagate as collective spin-wave excitations, known as magnons. These excitations provide a direct probe of the exchange interactions governing the system. A particularly useful regime for studying magnons is the field-polarized state, where a strong external magnetic field simplifies the spin dynamics, making them analytically accessible through linear spin-wave theory (LSWT).

In the field-polarized state, where all spins are aligned by an external magnetic field—effectively mimicking a ferromagnetic state, deviations from the polarized configuration can

be treated as small fluctuations. This allows the magnon spectrum to be well-described by LSWT, which approximates spin deviations as bosonic excitations. This approach provides a quantitative framework for modeling the dispersion relations of magnons, which are directly measured via inelastic neutron scattering.

The basic methodology begins with a Hamiltonian containing a given set of interactions, typically exchange interactions and a Zeeman term. The Hamiltonian is then rewritten in terms of bosonic raising and lowering operators that satisfy commutation relations (representing the magnon excitations) using second quantization techniques, such as the Holstein-Primakoff transformation. The resulting quadratic Hamiltonian is then diagonalized, yielding the magnon dispersion relation $\hbar\omega_{\boldsymbol{Q}}$, which is a function in reciprocal space parameterized by the set of interactions J in the Hamiltonian. While various methods exist for solving LSWT, the results tend to converge in the field-polarized regime due to the quadratic nature of the Hamiltonian formulation and the weakly interacting limit of the magnons. In cases where interactions are strong or where quantum fluctuations are significant, higher-order corrections to LSWT may be necessary to accurately describe the magnon spectrum. This allows experimental data to be fitted with LSWT, using the exchange interactions J as fitting parameters. Thus, by measuring $\hbar\omega_{\boldsymbol{Q}}$ using neutron scattering and comparing to LSWT predictions, one can quantify the strengths and types of magnetic interactions present in the system.

Experimental Considerations

With the theoretical groundwork established, we now turn to the experimental aspects, beginning with how neutrons are generated for scattering measurements. Neutrons are produced at large-scale research facilities using either spallation or nuclear fission (steady state) sources.

In a spallation source, high-energy protons are accelerated and directed onto a heavy metal target, typically tungsten or mercury. This impact induces a cascade of nuclear re-

actions, liberating neutrons from the target nuclei. These neutrons are then moderated using materials such as liquid hydrogen, water, or hot graphite to bring them to the desired energy/wavelength range before being directed toward experimental instruments. Spallation sources inherently operate in a pulsed mode, with neutron bursts produced at regular intervals determined by the proton beam repetition rate.

Reactor-based sources generate neutrons through nuclear fission, where a heavy nucleus, such as uranium-235, undergoes controlled chain reactions, releasing a steady flux of neutrons. These neutrons are moderated in a similar way to those from spallation sources, allowing precise selection of the neutron energy distribution. Unlike spallation sources, reactors provide a continuous neutron output, which is particularly advantageous for certain types of measurements that require high stability over extended periods.

Each neutron source type has distinct characteristics that influence its suitability for different experimental needs. Spallation sources produce neutrons in short, intense pulses with high peak brightness, enabling efficient energy selection and access to a broad energy spectrum. Reactor sources, in contrast, provide a continuous neutron flux, which is advantageous for experiments requiring stable, high-intensity beams over extended periods. Notable spallation facilities include the Spallation Neutron Source (SNS) in the U.S., which operates in a pulsed mode, and the Swiss Spallation Neutron Source (SINQ) in Switzerland, which uniquely functions as a continuous spallation source by using a neutron moderator optimized for steady extraction, rather than relying on pulsed proton beams. In contrast, reactor-based sources such as the High Flux Isotope Reactor (HFIR) in the U.S. and the NIST Center for Neutron Research (NCNR) in the U.S. offer continuous neutron beams with high average flux, making them particularly well-suited for experiments requiring long counting times or high cold neutron intensity. While reactors have historically been superior for cold neutron production due to dedicated moderators, advancements in spallation source design have significantly reduced this gap. The choice between spallation and reactor sources depends on experimental requirements, with spallation sources excelling in applications where pulsed

neutron delivery is beneficial and reactors providing advantages in scenarios that require sustained high flux and long-duration measurements.

Once neutrons are produced, they must be guided and conditioned before reaching the experimental instruments. Neutrons are transported along beamlines, which are typically evacuated to minimize losses due to air scattering. These beamlines often incorporate monochromators or choppers to refine the neutron energy spectrum based on experimental needs. Monochromators, typically made from highly ordered crystals such as pyrolytic graphite or silicon, use Bragg reflection to select a single neutron wavelength, making them essential for techniques like neutron diffraction and triple-axis spectroscopy. In contrast, choppers—rapidly rotating disks with precisely spaced slits—control the time structure of the neutron beam, a crucial component for time-of-flight spectroscopy.

Additional neutron optics, such as supermirror guides and focusing elements, enhance beam intensity and optimize spatial coherence. Supermirrors, composed of multilayer coatings of materials like Ni/Ti, extend the range of total reflection, allowing efficient transport of neutrons over long distances. Some instruments also employ polarizers and spin filters to prepare beams with specific spin states, enabling polarized neutron scattering experiments.

Once neutrons have been guided and conditioned, they interact with the sample at the experimental station, where different scattering techniques are used to extract structural and dynamical information. The experimental setup often requires specialized sample environments to control external conditions such as temperature, magnetic field, or pressure, ensuring that materials are studied under relevant thermodynamic regimes. Closed-cycle refrigerators (CCRs) and helium cryostats enable low-temperature measurements, while dilution refrigerators (DRs) are essential for reaching ultra-low temperatures below 100 mK, making them crucial for studying quantum ground states and low-energy excitations. High-temperature furnaces can reach up to 1800 K using neutron-transparent shielding materials like vanadium or niobium. Superconducting magnets allow for static magnetic field-dependent experiments up to 15 T, whereas pulsed magnets provide access to higher fields

for short-duration measurements. Pressure cells, such as diamond anvil cells, enable studies under extreme conditions, with careful material selection to minimize neutron attenuation. The sample itself must be mounted in low-background holders, such as thin-walled aluminum or vanadium cans for powders, or silicon and sapphire plates for single crystals.

The simplest of the neutron scattering techniques is neutron diffraction, which relies on the elastic scattering of neutrons to determine the atomic and magnetic arrangements within a material. When the neutron wavelength is comparable to interatomic distances, diffraction occurs according to Bragg's law (Eq. 2.18), producing a pattern that encodes information about the sample's periodic structure. This technique is widely used to refine crystal structures, identify phase transitions, and probe magnetic ordering.

For most bulk structural and magnetic investigations, powder neutron diffraction is the method of choice. In this approach, a powdered sample—consisting of randomly oriented microcrystals—is placed in a neutron beam, producing scattered intensities that form concentric rings. Instead of detecting the full rings, neutron powder diffractometers use position-sensitive detector banks arranged at fixed angles to collect diffraction intensities as a function of scattering angle 2θ. Similar to PXRD (discussed in Section 2.2.3), the data is recorded as intensity vs. 2θ, allowing structural and magnetic information to be extracted. By analyzing the positions, intensities, and shapes of the peaks in this pattern, researchers can determine lattice parameters, atomic positions, and long-range magnetic ordering in polycrystalline materials.

While neutron diffraction provides valuable static structural and magnetic information, many physical properties of interest—such as spin excitations, phonons, and other collective modes—require probing inelastic processes, where neutrons exchange energy with the sample. Studying these excitations necessitates measuring the final energy of the scattered neutrons, which is not analyzed in standard diffraction experiments. This can be accomplished through energy-resolved techniques that either use an analyzer crystal to select a specific final energy or determine it through the neutron's travel time. The former approach is the basis of triple-

axis spectroscopy (TAS), which allows for detailed energy-momentum mapping of excitations, while the latter forms the foundation of time-of-flight (TOF) spectroscopy, where a broad energy range is accessed in a single measurement.

Triple-axis spectroscopy (TAS) is an inelastic neutron scattering technique used to measure momentum- and energy-resolved excitations in materials. Unlike diffraction, which probes static structures, TAS allows the study of dynamical processes such as spin waves, phonons, and other collective excitations. The name "triple-axis" refers to the three key rotational axes involved in the experiment: the monochromator, sample, and analyzer crystal. A monochromator crystal first selects neutrons of a specific incident energy before they interact with the sample. Some neutrons scatter elastically, while others exchange energy and momentum with the sample, undergoing inelastic scattering. To determine the energy change, the scattered neutrons pass through an analyzer crystal, which selects only those with a specific final energy based on Bragg reflection. A detector then measures the intensity of these energy-selected neutrons, allowing researchers to extract information about the sample's excitations.

TAS provides a high degree of flexibility in data collection, as measurements can be performed in different scanning modes. By fixing the momentum transfer and varying the energy transfer, constant-Q scans reveal excitation spectra at specific wavevectors. Alternatively, constant-energy scans track how an excitation disperses across momentum space. This flexibility makes TAS particularly useful for mapping dispersions of well-defined excitations, such as magnons and phonons, along high-symmetry directions. However, TAS requires point-by-point scanning, which limits its efficiency when surveying broad energy and momentum regions. Compared to time-of-flight (TOF) spectroscopy, which captures a wide range of energy transfers simultaneously, TAS offers higher energy resolution but lower data acquisition rates. This makes it ideal for detailed investigations of specific excitations, complementing broader surveys performed with TOF techniques.

The data collected in TAS experiments forms a four-dimensional dataset of scattered

intensity as a function of momentum transfer ($\boldsymbol{Q}$) and energy transfer ($\hbar\omega$). Since visualizing a full 4D dataset is impractical, results are typically plotted as 2D slices—such as intensity maps of energy transfer vs. momentum along a particular direction—or 1D cuts, where intensity is plotted as a function of either energy or momentum at fixed parameters. These visualizations allow researchers to extract key information about excitation spectra, damping, and dispersion relations in the material.

Time-of-flight (TOF) spectroscopy is an inelastic neutron scattering technique that determines the final energy of scattered neutrons by measuring their travel time after interaction with the sample. When a neutron of known incident energy scatters from the sample, its final energy can be determined by measuring how long it takes to reach a detector at a known distance. This is based on the fundamental relation between neutron velocity and energy, where slower neutrons correspond to lower final energies and faster neutrons to higher energies. In practice, TOF spectrometers use a precisely timed neutron pulse from a spallation source, and the scattered neutrons are detected at different angles by large banks of ^{3}He position-sensitive detectors (PSDs) arranged in a semicircle around the sample. By recording the arrival time of neutrons at these detectors, their energy loss or gain during scattering is determined, allowing for a full energy and momentum map to be constructed in a single measurement.

TOF spectroscopy is particularly well-suited for studying broad energy and momentum ranges in materials, making it an essential tool for mapping magnon and phonon dispersions, diffuse scattering, and weakly correlated excitations. Because TOF instruments collect data over a large volume of reciprocal space in a single measurement, they are highly efficient for surveying excitation spectra, especially in systems where the dispersion relations are not well known beforehand. This makes TOF an ideal choice for exploratory studies, where an overview of excitations across different momentum directions is needed before performing more targeted measurements. However, while TOF excels at capturing large energy-momentum regions quickly, its energy resolution is typically lower than that of triple-axis

spectroscopy (TAS), since energy determination relies on measuring neutron flight times rather than precise selection via an analyzer crystal. This trade-off means that TOF is better suited for broad overviews of excitations and weak signals, while TAS remains the preferred method for high-resolution investigations of well-defined, sharp modes.

Like TAS, TOF datasets consist of intensity as a function of momentum transfer ($\boldsymbol{Q}$) and energy transfer ($\hbar\omega$), forming a four-dimensional dataset. Since TOF measurements inherently capture a broad energy-momentum range in a single experiment, the data is typically visualized as 2D intensity maps of energy vs. momentum along specific directions, or 1D cuts that highlight specific features such as dispersion relations or linewidth broadening. This ability to capture a wide spectral range efficiently makes TOF particularly valuable for studying complex excitation landscapes, especially in systems with multiple interacting modes or diffuse scattering features.

Chapter 3

A Further Investigation Into the Properties of $Yb_2Si_2O_7$

3.1 Context

When quantum objects are forced to make a choice between available physical states, the universe often allows them to exist in a combination of all possible states simultaneously—an effect known as *quantum entanglement*. Over the past century, extensive multi-disciplinary efforts have sought to explore, understand, and harness this phenomenon, pushing modern physics and technology toward a quantum future.

However, a fundamental challenge arises when carefully prepared quantum systems interact with the chaotic, non-Hermitian external environment. Such interactions cause decoherence, effectively averaging out quantum effects beyond microscopic scales [75]. To combat this, physicists employ extreme isolation techniques to maintain coherence across measurable distances. One promising avenue lies within condensed matter physics, where highly symmetric electromagnetic environments can stabilize exotic quantum states, making them accessible for experimental study.

One particularly striking manifestation of quantum entanglement in condensed matter systems is the Quantum Dimer Magnet (QDM). In a QDM, entangled pairs of spin-$\frac{1}{2}$ particles form a lattice of dimers, with a nonmagnetic singlet ground state $|S = 0, m_S = 0\rangle$. The first excited states—triplets ($|S = 1, m_S = -1, 0, 1\rangle$)—are separated from the singlet by a finite spin gap (Δ) and behave as bosonic quasiparticles known as triplons. In the presence of

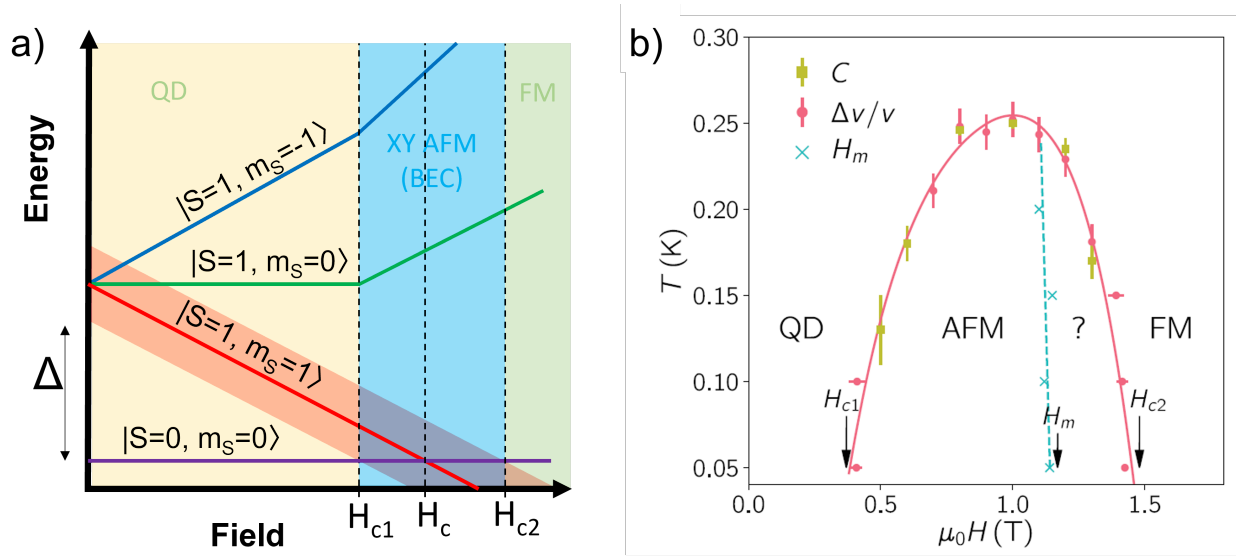

Figure 3.1: (a) Diagram illustrating the Zeeman splitting of dimer energy levels. States are labelled with their respective kets. Zero field spin gap Δ and critical fields are shown along the axes. The red shading indicates the energy dispersion due to intradimer interactions and the blue shading indicates the field region where triplons are thought to condense into a BEC. (b) BEC dome of $Yb_2Si_2O_7$ mapped out via transitions in heat capacity and ultrasound resonance measurements, adapted from Ref.[11].

a magnetic field, the degeneracy of the triplet states is lifted, and Δ decreases until the spin gap closes at a critical field H_c. For $H \geq H_c$, triplons become energetically favorable, effectively replacing the singlet ground state. This is illustrated in Fig. 3.1.

Above H_c, the system enters a Bose-Einstein Condensate (BEC) of triplons, where a macroscopic number of bosons occupy the lowest-energy single-particle state. This transition—analogous to superfluidity or superconductivity—breaks a continuous $U(1)$ symmetry, leading to the emergence of long-range XY antiferromagnetic (AFM) order. The field-induced phase diagram of a QDM thus resembles a "BEC dome", where the ordered phase exists between two critical fields, H_{c1} and H_{c2} [76].

In 2019, Hester et al. identified $Yb_2Si_2O_7$ as the first rare-earth-based QDM [11]. This system exhibits BEC-like triplon condensation, making it an ideal candidate for experimental and theoretical study. Unlike transition metal QDMs, $Yb_2Si_2O_7$ features strong spin-orbit coupling (SOC) and crystal electric field (CEF) effects, which stabilize an effective spin-$\frac{1}{2}$

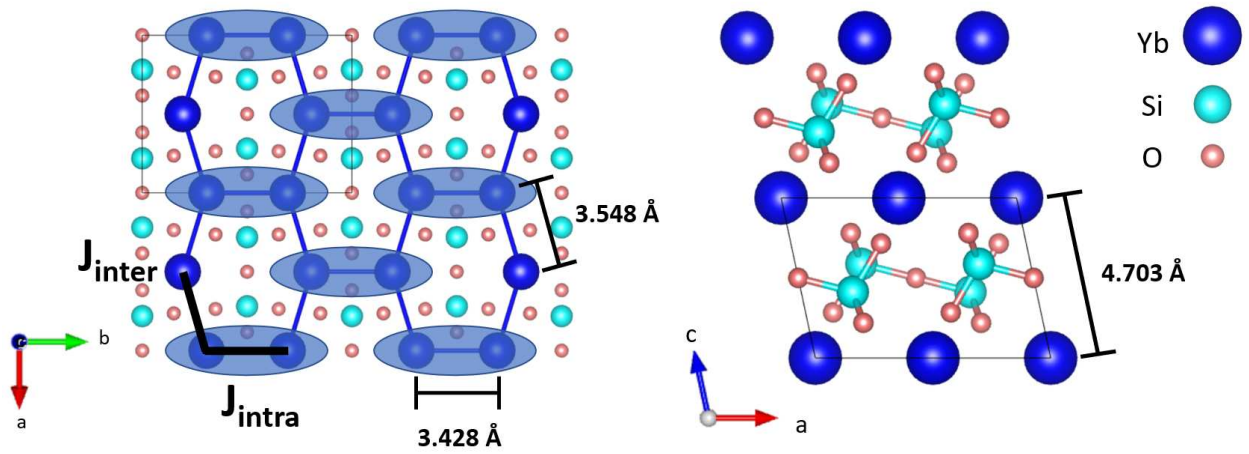

Figure 3.2: (a) Monoclinic (C2/m) crystal structure of $Yb_2Si_2O_7$ as viewed along the c axis, and (b) as viewed from the b axis. Yb atoms (blue) form a distorted honeycomb lattice in the ab-plane. Si atoms are cyan. O atoms are red. Interlayer and intra/interdimer distances and exchanges are illustrated in black.

description at low temperatures. Its monoclinic C2/m crystal structure (Figure 3.2) creates a distorted honeycomb lattice of Yb^{3+} ions, where subtle structural differences enhance intradimer interactions relative to interdimer ones, stabilizing robust singlet pairs, i.e., quantum dimers.

Experimental studies, including specific heat, ultrasound velocity, and inelastic neutron scattering (INS), have been used to map out the BEC phase diagram of $Yb_2Si_2O_7$. These measurements provided strong evidence for field-induced phase transitions and the formation of a Bose-Einstein condensate (BEC) of triplons, establishing $Yb_2Si_2O_7$ as a rare-earth quantum dimer magnet (QDM). However, despite clear thermodynamic signatures of a phase transition leading into the BEC dome, determination of the particular antiferromagnetic (AFM) order remained elusive.

In many quantum dimer magnets, the BEC phase is characterized by long-range XY AFM order, which should be observable via elastic neutron scattering. A previous diffraction experiment on HB-1A attempted to detect this ordering by measuring Bragg peak intensities as a function of applied field. However, these measurements were inconclusive due to limited resolution and an unfortunate sample torquing caused by the strong g-tensor anisotropy,

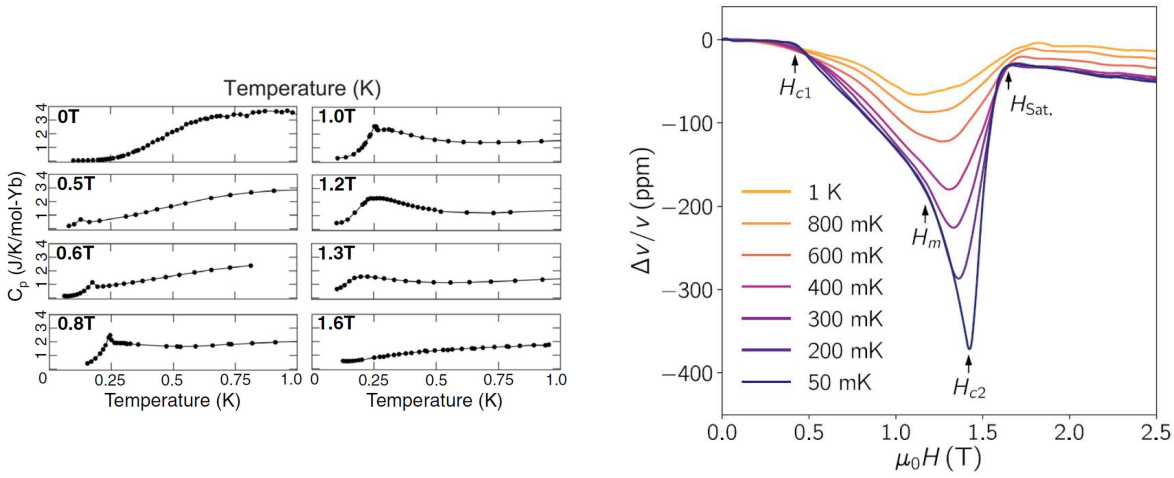

(a) (b)

Figure 3.3: Measurements used to map out the BEC dome of $Yb_2Si_2O_7$. (a) Specific heat measurements as a function of temperature and magnetic field. As magnetic field is increased, a sharp transition can be seen at lower fields, which smooths out at fields above 1T before dissapating at higher fields. (b) Ultrasound velocity measurements as function of temperature and field. Aside from the obvious slope changes around the critical fields H_{c1} and H_{c2}, an additional kink feature is observed around the proposed mystery field $H_m \approx$ 1.1T.

which led to uncertainty in crystal alignment. As a result, it was not possible to reliably and precisely determine the magnetic structure.

Additionally, recent measurements indicate the presence of two distinct phases within the BEC dome of Yb_2Si2O7, which deviates from the behavior expected in conventional QDM models. This phenomenon is evident in both the heat capacity and ultrasound velocity data (Fig. 3.3). Specifically, while clear slope changes are observed around the critical fields H_{c1} and H_{c2}, an additional anomaly appears around the intermediate field $H_m \approx$ 1.1T. This observation suggests a two-phase structure within the BEC dome.

To account for this unconventional phase behavior, a theoretical model was recently proposed that introduces a staggered g-tensor [12]. The model hypothesizes that the principal axis of the g-tensor is tilted away from the crystallographic c-axis and alternates in direction between adjacent Yb sites, resulting in staggered M_x and M_y moments. This symmetry breaking generates off-diagonal components in the ordered state, which could directly affect

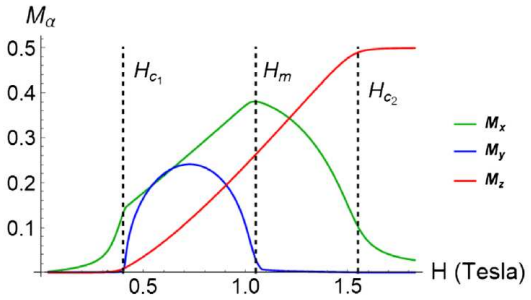

Figure 3.4: Magnetization components M_x (green), M_y (blue), and M_z (red) in $Yb_2Si_2O_7$ obtained from mean-field theory. For $H_{c1} < H < H_m$, the presence of finite M_x and M_y indicates a staggered transverse moment, characteristic of an XY antiferromagnetic phase. At H_m, M_y vanishes, marking a transition to a canted phase, followed by full polarization for $H > H_{c2}$. Adapted from Ref. [12].

the Bragg peak intensities observed in neutron scattering.

Given the unusual nature of this proposed model, further experimental verification was crucial. A second attempt was necessary to both probe the magnetic structure within the BEC dome and rigorously test the staggered g-tensor hypothesis. The following sections detail our improved elastic neutron scattering and magnetization measurements, aimed at providing a definitive assessment of the proposed model and clarifying the magnetic behavior within the BEC dome of $Yb_2Si_2O_7$.

3.1.1 Contributions

The synthesis of $Yb_2Si_2O_7$ was primarily performed by H. S. Nair, T. Reeder, G. Hester, T. N. DeLazzer, J. R. Neilson, and K. A. Ross. Magnetization measurements and the analysis was performed by A. Treglia. The elastic neutron scattering measurements and analysis were performed by A. Treglia, K. A. Ross, and A. A. Aczel.

3.2 Preparation

3.2.1 Theory

The staggered g-tensor model proposed for $Yb_2Si_2O_7$ suggests a field-dependent competition between M_x and M_y moments within the BEC dome. To test this hypothesis, we calculated the expected Bragg peak intensities using the spin expectation values obtained from mean-field theory (MFT) by Flynn et al. [12]. These spin expectation values predict the evolution of magnetization components M_x, M_y, and M_z as a function of magnetic field (Fig. 3.4).

To facilitate a direct comparison with neutron scattering data, we computed the magnetic form factor, $\boldsymbol{\mathcal{F}}(\boldsymbol{Q})$, using the calculated spin components as inputs. The magnetic form factor, representing the Fourier transform of the spin density distribution, is given by

$$\boldsymbol{\mathcal{F}}(\boldsymbol{Q}) = \sum_m \boldsymbol{S}_m e^{i\boldsymbol{Q}\cdot\boldsymbol{r}_m} \tag{3.1}$$

In the monoclinic (C2/m) structure of $Yb_2Si_2O_7$, the x, y, and z axes correspond to the $\hat{a^*}$, $\hat{b}$, and $\hat{c}$ crystallographic directions, respectively. Therefore, the magnetization vector $\boldsymbol{M}$ can be expressed as

$$\boldsymbol{M} = M_x\hat{a^*} + M_y\hat{b} + M_z\hat{c} \tag{3.2}$$

We could then convert $\boldsymbol{M}$ from the monoclinic basis to cartesian coordinates with the following transformation

$$\begin{aligned} \hat{a^*} &= (\sin(\beta), 0, \cos(\beta)) \\ \hat{b} &= (0, 1, 0) \\ \hat{c} &= (\cos(\beta), 0, \sin(\beta)) \end{aligned} \tag{3.3}$$

which gives

$$\boldsymbol{M} = (M_x\sin(\beta) + M_z\cos(\beta), M_y, M_x\cos(\beta) + M_z\sin(\beta)) \tag{3.4}$$

In the interest of clarity, we show the magnetic unit cell in Fig. 3.5, and write out the

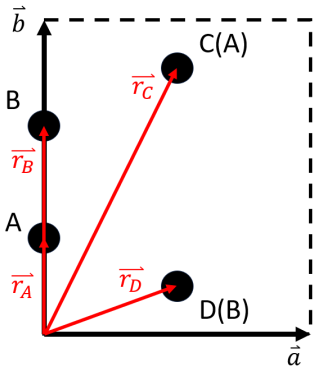

Figure 3.5: Magnetic unit cell of $Yb_2Si_2O_7$. Black dots are the Yb sites, red vectors show the cartesian coordinates of each, and each of the four sites is designated as lying on the A or B sublattices.

position vectors, $\boldsymbol{r_i}$ as

$$\begin{aligned}
\boldsymbol{r}_A &= y_1\boldsymbol{b} &&= (0, y_1 b, 0), \\
\boldsymbol{r}_B &= y_2\boldsymbol{b} &&= (0, y_2 b, 0), \\
\boldsymbol{r}_C &= \frac{1}{2}\boldsymbol{a} + y_3\boldsymbol{b} &&= \left(\frac{1}{2}a, y_3 b, 0\right), \\
\boldsymbol{r}_D &= \frac{1}{2}\boldsymbol{a} + (1-y_3)\boldsymbol{b} &&= \left(\frac{1}{2}a, (1-y_3)b, 0\right)
\end{aligned} \tag{3.5}$$

Additionally, we can write out the reciprocal lattice vector in the monoclinic basis as

$$\boldsymbol{Q} = (\frac{2\pi h}{a}, \frac{2\pi k}{b}, \frac{2\pi l \csc(\beta)}{c} - \frac{2\pi h \cot(\beta)}{a}) \tag{3.6}$$

With our geometry now explicitly established, we can move to the calculation of the magnetic form factor.

For a given magnetic field $\boldsymbol{H} = H\hat{z}$, we can expand the magnetic form factor as a sum over the 4 magnetic lattice sites A-D in the magnetic unit cell

$$\begin{aligned}
\boldsymbol{\mathcal{F}}(\boldsymbol{Q}) &= \sum_m \boldsymbol{M}_m e^{i\boldsymbol{Q}\cdot\boldsymbol{r}_m} \\
&= \boldsymbol{M}_A e^{2\pi i y_1 k} + \boldsymbol{M}_B e^{2\pi i y_2 k} + \boldsymbol{M}_C e^{2\pi i[\frac{h}{2}+y_3 k]} + \boldsymbol{M}_D e^{2\pi i[\frac{h}{2}+(1-y_3)k]}.
\end{aligned} \tag{3.7}$$

In order to include the staggered component of the g-tensor, we must then stipulate that

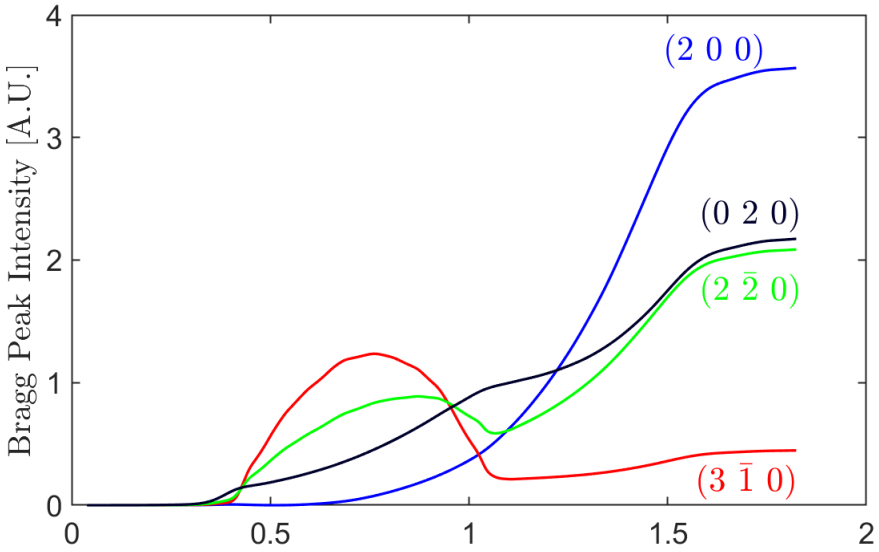

Figure 3.6: Expected bragg peak intensity behavior as a function of applied magnetic field. The four peaks shown here were selected based on available Q coverage in HB-1A as well as those that would clearly display a hump signature within the dome for this staggered model (aside from (200), which is only sensitive to the z-component).

the x and y components of all B sites are flipped. We can now write out the fully expanded vector magnetic form factor as

$$\begin{aligned}\boldsymbol{\mathcal{F}}(\boldsymbol{Q}) =&(M_x\sin(\beta)+M_z\cos(\beta), M_y, M_x\cos(\beta)+M_z\sin(\beta))e^{2\pi i y_1 k}\\ &+(-M_x\sin(\beta)-M_z\cos(\beta), -M_y, M_x\cos(\beta)+M_z\sin(\beta))e^{2\pi i y_2 k}\\ &+(M_x\sin(\beta)+M_z\cos(\beta), M_y, M_x\cos(\beta)+M_z\sin(\beta))e^{2\pi i[\frac{h}{2}+y_3 k]}\\ &+(-M_x\sin(\beta)-M_z\cos(\beta), -M_y, M_x\cos(\beta)+M_z\sin(\beta))e^{2\pi i[\frac{h}{2}+(1-y_3)k]}\end{aligned} \tag{3.8}$$

Since neutron scattering measures magnetic moments perpendicular to the scattering vector $\boldsymbol{Q}$, the experimentally relevant quantity is $|\boldsymbol{\mathcal{F}}_\perp(\boldsymbol{Q})|^2$, the perpendicular component of the magnetic form factor, which is directly proportional to the expected Bragg peak intensities.

For this next step, we first take the component of $\boldsymbol{\mathcal{F}}$ that is perpendicular to $\boldsymbol{Q}$ with the relation

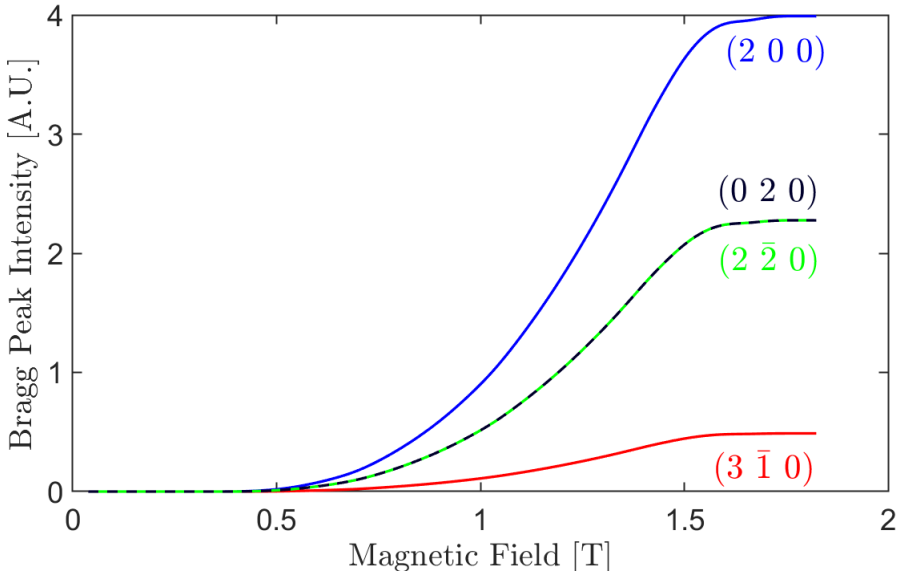

Figure 3.7: Expected bragg peak intensity behavior with no staggered moments (uniform) as a function of applied magnetic field. Here, no deviation from monotonic growth is seen throughout the BEC dome.

$$\boldsymbol{\mathcal{F}}_{\perp}(\boldsymbol{Q}) = \boldsymbol{\mathcal{F}} - \frac{\boldsymbol{\mathcal{F}} \cdot \boldsymbol{Q}}{|\boldsymbol{Q}|^2}\boldsymbol{Q} \tag{3.9}$$

Once we have the perpendicular component, we then take its conjugate squared to reveal a function of Q, as well as the magnetic field dependent M_α values from the work of Flynn et al.

Fig. 3.6 depicts a few of the selected results from the calculation of $|\boldsymbol{\mathcal{F}}_{\perp}(\boldsymbol{Q})|^2$ as function of $\boldsymbol{Q}$ and external magnetic field H. It should be noted that this model was used to qualitatively compare to neutron scattering results, as expected intensity is not equal to $|\boldsymbol{\mathcal{F}}_{\perp}(\boldsymbol{Q})|^2$, but simply proportional. Though the intensity from actual neutrons will be scaled differently, the appearance (or lack thereof) of hump signatures within the BEC dome for peaks sensitive to the x and y components should be within our experimental resolution.

For comparison, we also calculated $|\boldsymbol{\mathcal{F}}_{\perp}(\boldsymbol{Q})|^2$ without staggering the x and y components. This can be seen in Fig. 3.7, where we show the same four bragg peaks with a purely uniform (z) component. From this, we can see that no hump signatures would be seen within the

BEC dome. Rather, we would expect to see a purely monotonic growth until the spins are fully polarized above H_{c2}.

3.2.2 Samples

Single-crystal samples of $Yb_2Si_2O_7$ were previously synthesized using the optical floating zone (OFZ) method, a technique well-suited for growing high-purity, large single crystals. The starting material was prepared by combining stoichiometric amounts of Yb_2O_3 and SiO_2, followed by multiple heating cycles at 1350°C under high-temperature conditions to ensure complete reaction and phase purity. The resultant polycrystalline material was then hydrostatically pressed into cylindrical rods with an 8 mm diameter, which served as feedstock for crystal growth.

Crystals were grown using a Crystal Systems FZ-T-10000-H-VIII-VPO-PC optical floating zone furnace, under optimized conditions. The best results were obtained with 1.5 kW lamps at 70-73% power, a growth rate of 3-5 mm/hr, and an oxygen atmosphere (1-2 L/min flow rate) to maintain oxidation conditions. A counter-rotation of 20 rpm between the feed and seed rods was used to promote uniform crystal growth. Despite careful optimization, most boules exhibited some level of cracking and multi-crystallinity, which required post-growth selection and characterization to isolate high-quality single-crystal domains.

Individual crystals were cleaved from the boule and characterized via Laue X-ray diffraction to assess crystallographic quality and determine their orientations. Since multiple growth attempts had been performed, dozens of crystals were screened using Laue diffraction to identify the highest-quality specimens with minimal mosaicity. The final selected crystal exhibited well-defined Laue diffraction spots, indicative of excellent single-crystal quality. A representative Laue image and corresponding fit are shown in Fig. 3.8.

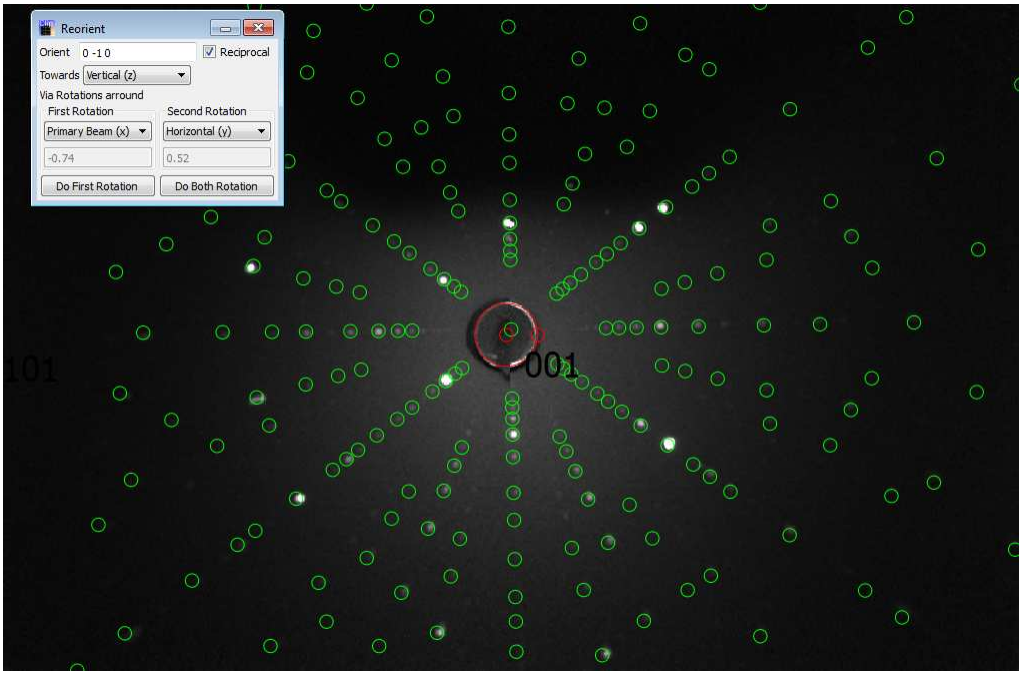

Figure 3.8: Laue X-ray diffraction pattern of a $Yb_2Si_2O_7$ single crystal, showing alignment along the crystallographic *c*-axis. The experimental diffraction spots (bright points) closely match the calculated pattern (green circles), confirming high single-crystal quality. The fit places the sample within 1° of perfect alignment, ensuring precise orientation for subsequent measurements.

3.3 Experiments

With high-quality single crystals of $Yb_2Si_2O_7$ selected and oriented, a series of experimental measurements were conducted to investigate its magnetic properties and field-induced behavior. Our primary objectives were to characterize the anisotropic magnetization response and investigate the proposed staggered g-tensor model which aims to describe the observed two-phase structure within the BEC dome. To this end, magnetization measurements were performed using a superconducting quantum interference device (SQUID) magnetometer, and elastic neutron scattering was conducted on HB-1A, a triple-axis spectrometer at Oak Ridge National Labs. The following sections describe these experiments in detail.

3.3.1 Magnetization Measurements

Magnetization measurements were performed using a Quantum Design MPMS3 SQUID magnetometer, equipped with the horizontal rotator probe option to allow for controlled angular-dependent studies. The goal of these measurements was to investigate the anisotropic magnetic response of $Yb_2Si_2O_7$.

Given the material's strong g-tensor anisotropy, maintaining mechanical stability during mounting was critical to prevent torque-induced misalignment in applied magnetic fields. Initially, the sample was mounted using GE-varnish alone, but this proved insufficient, as the sample became dislodged during an M(H) sweep and fell into the MPMS3 sample chamber, necessitating retrieval from the sample chamber. To prevent this from recurring, the mounting method was modified to a more secure sandwich configuration, where the sample was placed between two thin quartz plates (from a broken glass slide) and secured with a small amount of GE-varnish. This setup prevented sample displacement while minimizing background interference. Photographs of these mounted samples are shown in Fig. 3.9.

The field-dependent magnetization of $Yb_2Si_2O_7$ was measured along the crystallographic a- and b-axes up to 7 T at 1.8 K, as shown in Fig. 3.10. The data reveal a notably stronger

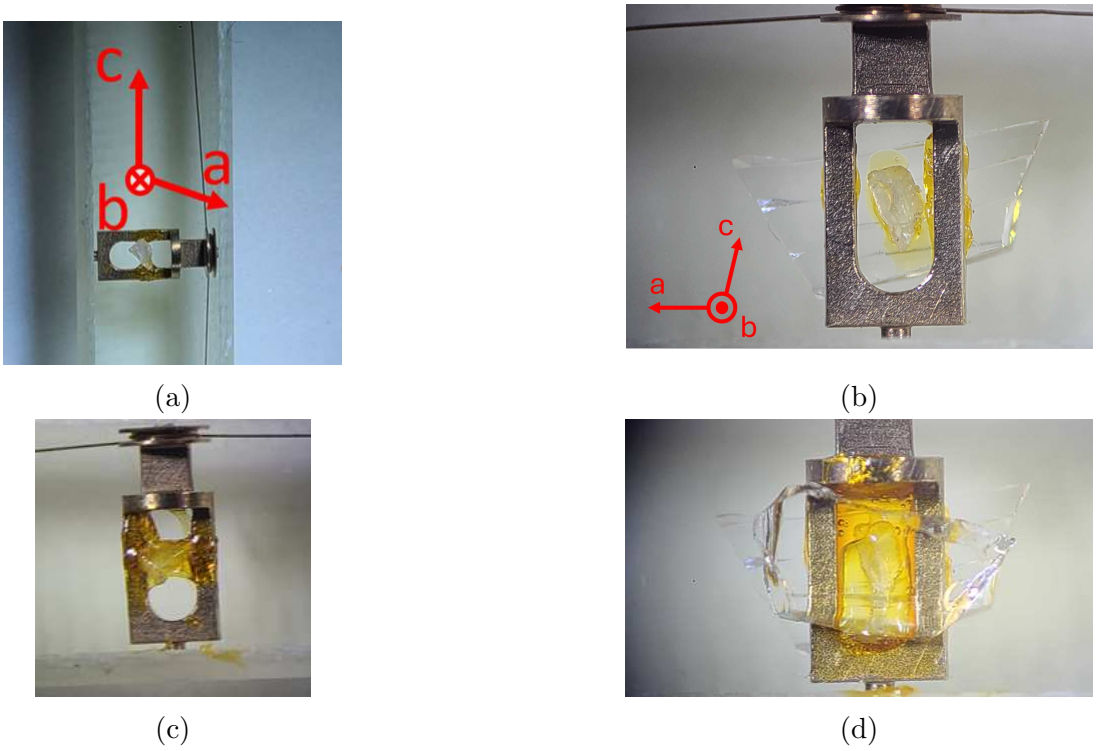

(a) (b)

(c) (d)

Figure 3.9: Photographs of the $Yb_2Si_2O_7$ single-crystal mounting process for magnetization measurements. (a) and (b) show the sample during alignment for bc-plane and ab-plane sweeps, respectively. (c) and (d) show the final mounted configurations. The sample was secured between two thin quartz plates to minimize torqueing effects under applied magnetic fields.

response for $H \parallel a$ compared to $H \parallel b$, consistent with previous reports [11]. Clear saturation behavior is observed, with M(H) along $H \parallel a$ reaching a near-constant value above 5 T. In contrast, $H \parallel b$ exhibits a more gradual approach to saturation, asymptotically flattening near 7 T. This behavior reflects the progressive alignment of Yb^{3+} moments in the applied field, in accordance with the expected strong single-ion anisotropy.

Temperature-dependent magnetization measurements were conducted with $H \parallel b$ at a fixed field of 1000 Oe from 300 K down to 1.8 K, as shown in Fig. 3.11a. The data exhibit a typical paramagnetic response, decreasing monotonically with cooling, with no anomalies observed above the expected ordering temperature of 250 mK. This result is consistent with previous thermodynamic studies, confirming that $Yb_2Si_2O_7$ remains in a paramagnetic state within the temperature range accessible by the base MPMS3 system.

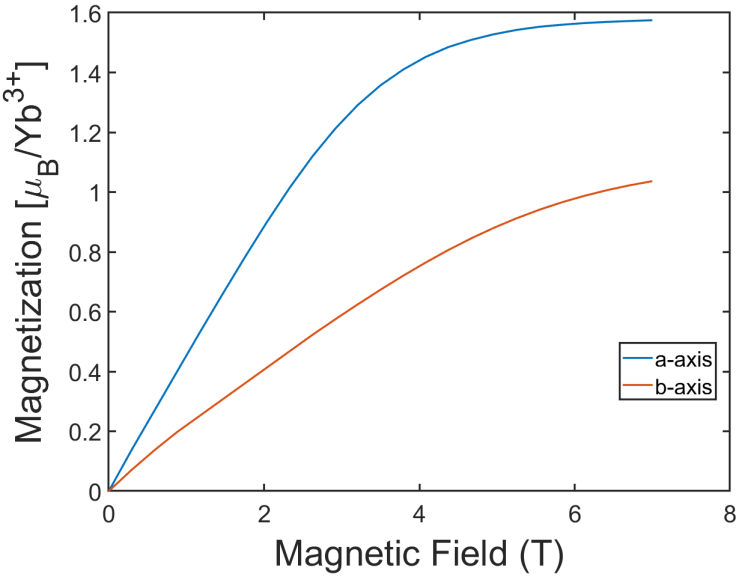

Figure 3.10: Field-dependent magnetization of $Yb_2Si_2O_7$ measured along the crystallographic a- and b-axes at 1.8 K. The data show a stronger response for H $\parallel$ a compared to H $\parallel$ b, consistent with previous reports [11]. Saturation is observed above 5 T for $H \parallel a$, while $H \parallel b$ exhibits a more gradual approach toward saturation, leveling off near 7 T.

To further analyze the magnetic behavior, Curie-Weiss fits were performed in two temperature regimes: a high-temperature fit for T>130 K and a low-temperature fit for T<40 K, as shown in Fig. 3.11. The high-temperature fit yields an effective moment of $\mu_{\text{eff}} = 2.44\mu_B$ and a Curie-Weiss temperature of $\Theta_{\text{CW}} = -252$ K. The extracted effective moment is lower than the free-ion value of 4.54 μ_B expected for Yb^{3+} in the J=7/2 state, consistent with crystal field effects splitting the J manifold and confining the system to a low-energy effective spin-1/2 doublet. However, the large negative Curie-Weiss temperature suggests an apparent strong antiferromagnetic interaction, though this likely does not reflect the true exchange strength due to the influence of excited crystal field levels.

At lower temperatures, a second Curie-Weiss analysis was performed for T<40 K, yielding a significantly reduced effective moment of $\mu_{\text{eff}} = 0.95\mu_B$ and a Curie-Weiss temperature of $\Theta_{\text{CW}} = -2.96$ K. This shift indicates that as thermal population of higher-energy crystal field levels becomes negligible, the system transitions to a regime dominated by the ground-state doublet, leading to a drastically different susceptibility response. The near-zero Θ_{CW} in this

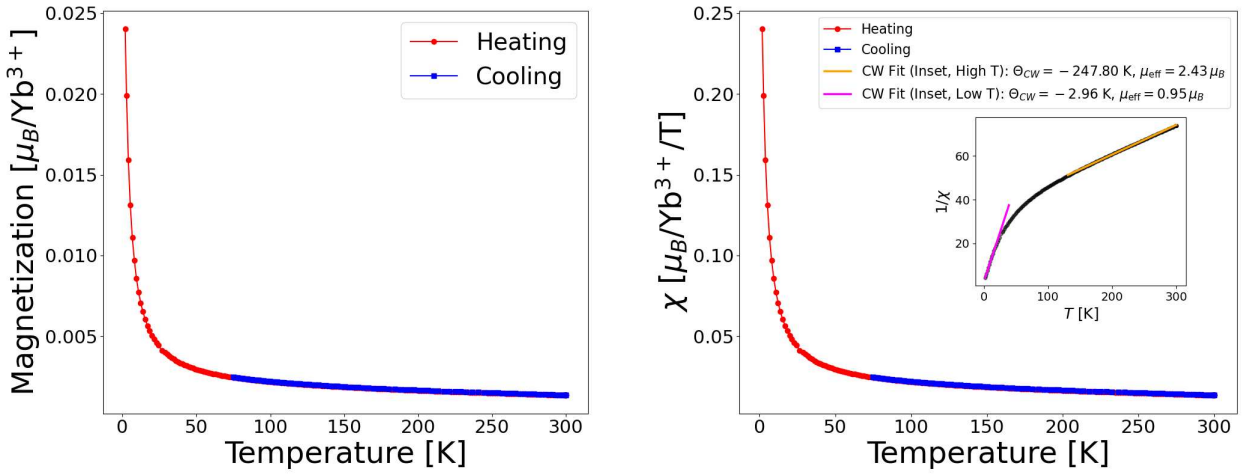

(a) (b)

Figure 3.11: (a) Magnetization vs. temperature for $Yb_2Si_2O_7$ with $H \parallel b$ at 1000 Oe, showing a monotonically decreasing paramagnetic response down to 1.8 K. (b) Magnetic susceptibility χ as a function of temperature, with Curie-Weiss fits shown in the inset for high and low temperature regimes. The high-temperature fit (T>130 K) yields an effective moment of $\mu_{\text{eff}} = 2.44\,\mu_B$ and a Curie-Weiss temperature of $\Theta_{\text{CW}} = -252$ K, while the low-temperature fit deviates due to crystal field effects, yielding $\mu_{\text{eff}} = 0.95\,\mu_B$ and a Curie-Weiss temperature of $\Theta_{\text{CW}} = -2.96$ K.

range suggests that exchange interactions are relatively weak within the low-energy manifold, emphasizing the role of anisotropic interactions and the g-tensor structure in determining the low-temperature magnetism. These effects will be explored further in later sections, where we discuss the anisotropic g-tensor and its implications for the observed magnetic properties.

The angle-dependent magnetization measurements show a clear periodicity, with maxima and minima corresponding to the high-symmetry directions of the $\hat{a}^*$, $\hat{b}$, and $\hat{c}$ crystallographic axes. The overall trend follows $M_c > M_a > M_b$, with the difference between M_c and M_a being relatively small. This alignment of the principal axes along the $\hat{a}^*$, $\hat{b}$, and $\hat{c}$ directions suggests that the g-tensor is not significantly tilted away from the c-axis, as was proposed in the staggered g-tensor model.

These measurements display strong reproducibility, with close agreement between forward and reverse rotations, as well as consistency with field-dependent $M(H)$ measurements along the principal axes. The polar representation in Fig. 3.12b further highlights the anisotropic

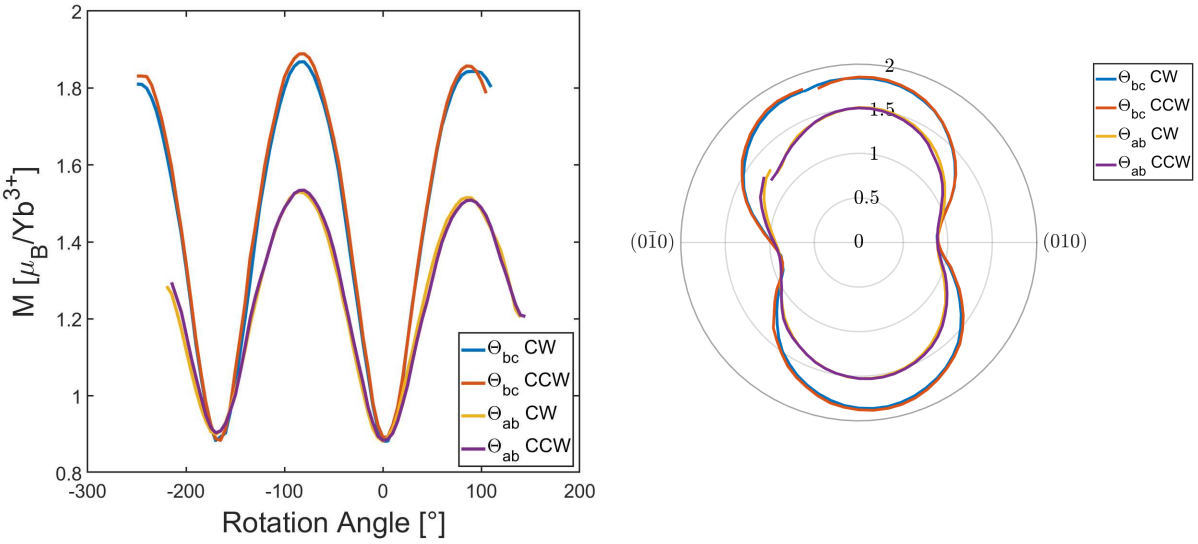

(a) (b)

Figure 3.12: (a) (a) Angle-dependent magnetization measurements of $Yb_2Si_2O_7$ at 1.8 K and 5 T, showing a periodic response with extrema occurring close to 90° intervals. Minor deviations from exact periodicity are likely due to slight misalignment or imperfect rotation through the intended crystallographic plane. (b) The corresponding polar plot highlights the anisotropic nature of the response.

response, revealing a slight asymmetry, likely due to minor sample misalignment or imperfect rotation through the intended plane. These results will be discussed in more detail in a following section.

3.3.2 Neutron Scattering

The neutron scattering experiment was conducted on pre-mounted $Yb_2Si_2O_7$ single-crystal samples that were shipped to Oak Ridge National Laboratory (ORNL) for measurement. The samples were pre-mounted prior to this study, and while details of their original mounting are unavailable, they were used as received for elastic neutron scattering measurements without modification.

The neutron scattering experiment was conducted using the HB-1A triple-axis spectrometer (TAS) at the High Flux Isotope Reactor (HFIR) at Oak Ridge National Laboratory (ORNL). HB-1A is a fixed-incident-energy spectrometer optimized for elastic scattering mea-

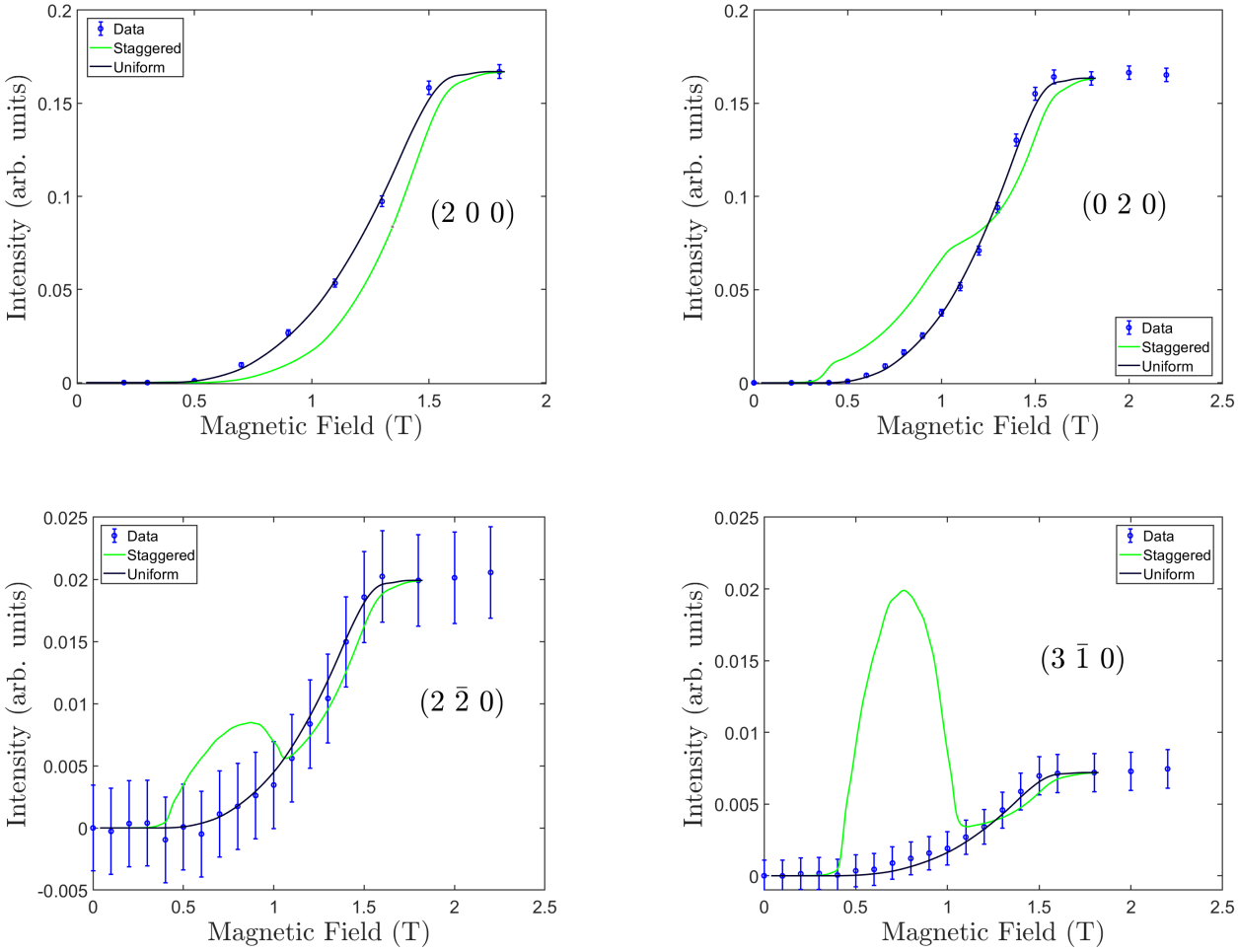

Figure 3.13: Field-dependent neutron scattering intensity at selected Bragg peaks in $Yb_2Si_2O_7$, measured as a function of applied magnetic field. The data (blue points) closely follow the predictions of the uniform moment model (black) across the entire field range, while the staggered moment model (green) predicts a hump-like feature in the intermediate field range that is not observed. This absence of staggered magnetization suggests that $Yb_2Si_2O_7$ does not exhibit the expected two-sublattice antiferromagnetic order, challenging prior theoretical expectations and raising questions about the nature of magnetic correlations in the system.

surements, making it well-suited for tracking Bragg peak intensities as a function of applied magnetic field. Measurements were performed at a base temperature of approximately 50 mK using a dilution refrigerator, with applied fields up to 2.25 T. The primary objective was to monitor the intensity of selected magnetic Bragg peaks as a function of field and compare the observed behavior to theoretical predictions. As discussed in Section 3.2.1, the

staggered g-tensor model predicts that, within the BEC dome (H_{c1} <H< H_{c2}), Bragg peaks sensitive to the x- and y-spin components should exhibit a characteristic hump feature. By comparing the measured intensity evolution to the uniform and staggered moment models, the experiment aimed to assess whether $Yb_2Si_2O_7$ hosts a field-induced antiferromagnetic state consistent with prior theoretical and experimental work.

Selected results from the experiment are presented in Fig. 3.13, showing the field-dependent Bragg peak intensities alongside two theoretical models: a staggered g-tensor model (green) and a uniform moment model (black). The models are normalized to match the experimental data in the high-field polarized limit ($H > H_{c2}$), allowing for a direct qualitative comparison. The data do not show a discernible hump feature within the intermediate field regime predicted by the staggered model, while the uniform model shows a more consistent alignment with the observed trend. This suggests that the staggered g-tensor model may not fully capture the field-dependent magnetic behavior of $Yb_2Si_2O_7$. The implications of this result are discussed further in the following section, where we explore the potential limitations of the model and alternative interpretations.

3.4 Discussion

The results presented in this study provide important insights into the magnetic behavior of $Yb_2Si_2O_7$. Our experimental efforts focused on two main objectives: (1) verifying the previously observed field-induced magnetic behavior and anisotropy, and (2) evaluating whether the staggered g-tensor model could account for the unconventional two-phase structure observed within the BEC dome. Through comprehensive magnetization and neutron scattering experiments, we systematically investigated the magnetic structure of $Yb_2Si_2O_7$ in the context of this staggered model. Instead, our findings strongly indicate that this model does not accurately describe the magnetic structure, challenging prior theoretical predictions.

Our magnetization measurements revealed a highly anisotropic response, consistent with

the presence of strong single-ion anisotropy. The field-dependent data was consistent with the previous study by Hester et al. [11]. The temperature-dependent magnetization data displayed a clear transition from a high-temperature paramagnetic regime to a low-temperature regime dominated by an effective spin-1/2 doublet. Notably, the high-temperature Curie-Weiss fit (T>130 K) yielded a large negative Θ_{CW}, indicative of apparent strong antiferromagnetic interactions. However, this effect likely reflects the influence of excited crystal field states rather than intrinsic exchange interactions. At lower temperatures (T<40 K), the effective moment decreases significantly, reflecting the dominant role of the ground-state doublet and revealing much weaker exchange interactions.

Angle-dependent magnetization measurements revealed that the principal axes of the magnetic response align with the crystallographic $\hat{a^*}$, $\hat{b}$, and $\hat{c}$ directions, rather than being tilted away from the c-axis as proposed by the staggered g-tensor model. This observation provides strong evidence against the model's key prediction that the g-tensor principal axis alternates between adjacent Yb sites. The polar representation of the angle-dependent data highlights the anisotropic response, showing a slight asymmetry, which is likely attributable to minor sample misalignment or imperfect rotation through the intended plane.

Neutron scattering measurements were conducted to investigate whether the staggered g-tensor model could account for the unconventional two-phase structure observed within the BEC dome. Field-dependent Bragg peak intensities were measured and compared to predictions from both the staggered g-tensor model and a uniform moment model. The models were normalized to match the high-field polarized limit ($H > H_{c2}$) to facilitate a direct qualitative comparison. The experimental data consistently followed the uniform moment model across the entire field range, whereas the staggered model predicted a characteristic hump feature in the intermediate field regime that was not observed within the experimental resolution.

While the absence of nonmonotonicity in the Bragg peak intensity suggests that the staggered g-tensor model does not accurately describe the field-induced magnetic structure

of $Yb_2Si_2O_7$, there are some considerations to address. One possibility is that strong quantum fluctuations could suppress the expected hump feature, preventing its resolution. Another is that the sample may not have fully reached base temperature during the measurement, which could reduce the visibility of subtle magnetic effects. However, both of these scenarios are unlikely given the consistency of the data with the uniform moment model and the robust evidence from magnetization measurements indicating that the principal axis lies along the crystallographic c-axis. These factors strongly disfavor the staggered g-tensor model as an explanation for the two-phase structure observed within the BEC dome.

Chapter 4

Synthesis, Preparation, and Experimentation on $ErCl_3$

4.1 Context

Early in our investigation of potential Quantum Spin Liquid (QSL) candidates, we explored a diverse range of materials with properties that aligned with the theoretical requirements for realizing Kitaev or other bond-dependent interactions. Key criteria included the presence of spin-1/2 (or effective spin-1/2) particles arranged on a honeycomb lattice, crystal symmetries capable of suppressing competing interactions such as the Dzyaloshinskii-Moriya (DM) interaction through inversion symmetry, and sufficient interlayer spacing to confine magnetic interactions to two dimensions[77, 78, 79]. Additionally, practical considerations, such as the ability to synthesize these materials in bulk quantities for neutron scattering experiments, were essential.

Our initial attention was drawn to the RX_3 series (RX_3, where R = rare-earth, X = Cl, Br, I), with $YbCl_3$ standing out as a promising candidate. This interest stemmed from its compatibility with our imposed criteria and its mention in recent theoretical papers predicting bond-dependent anisotropic exchange interactions [80, 81, 79]. These predictions were largely attributed to the edge-sharing octahedra of ligand ions surrounding the rare-earth ions, which provide the superexchange pathways necessary to facilitate the bond-dependent exchange anisotropy. Moreover, $YbCl_3$ was readily available in polycrystalline powder form and reportedly amenable to growth into large crystals via chemical vapor transport (CVT),

a synthesis technique that was both familiar and accessible[58].

After successfully synthesizing single crystals of $YbCl_3$ using the CVT technique, we validated their purity through magnetization and specific heat measurements, finding excellent agreement with existing literature[82]. These results confirmed the suitability of our samples for further investigation. Subsequently, we proposed several inelastic neutron scattering experiments to quantify the exchange interactions in the ground state by fitting measured spin waves using a linear spin wave theory (LSWT) parameterized by Kitaev-based models. However, Sala et al. conducted similar experiments and demonstrated that $YbCl_3$ behaves as a nearly ideal two-dimensional Heisenberg antiferromagnet with a Néel ground state [83, 84]. This finding implies that the magnetic interactions in $YbCl_3$ are isotropic and dominated by nearest-neighbor Heisenberg exchange, contrasting sharply with the bond-dependent anisotropic exchange predicted in Kitaev-based models. With no evidence of Kitaev-like interactions in $YbCl_3$, we turned to alternative RX_3 compounds where anisotropic exchange may be stronger.

While $YbCl_3$ remains an intriguing subject for studying phenomena such as magnon dynamics, magnetic field dependence, and the effects of strong spin-orbit coupling in Heisenberg materials, we shifted our focus to another member of this family—$ErCl_3$. This transition was motivated by several unique properties of $ErCl_3$ that distinguish it from other RX_3 compounds. The Er^{3+} ion ($4f^{11}$) has a larger unquenched orbital moment, resulting in stronger spin-orbit coupling and enhanced single-ion anisotropy compared to Yb^{3+}, making its exchange interactions more sensitive to the crystal field environment. These factors contribute to a greater likelihood of bond-dependent exchange interactions, a crucial ingredient for realizing Kitaev-like physics. Furthermore, neutron diffraction studies have revealed an unusual antiferromagnetic order in $ErCl_3$, distinct from the simple Néel state seen in $YbCl_3$, suggesting that competing interactions contribute to its ground state[85, 86, 15]. These attributes, along with its structural compatibility with theoretical models, make $ErCl_3$ a particularly promising candidate for exploring novel quantum magnetic phenomena.

This chapter first details the synthesis and optimization of high-quality single crystals of $ErCl_3$, an essential step for ensuring the reliability of subsequent neutron scattering experiments. Special emphasis is placed on the iterative development of synthesis methods, addressing the unique challenges posed by the air-sensitive and hygroscopic nature of the material. Detailed discussions will outline the innovative techniques employed to maintain sample integrity during preparation and experimentation, including strategies for air-free handling and transport.

Following the synthesis and preparation, we then describe the meticulous planning and execution of inelastic neutron scattering experiments. These experiments are designed to probe the bond-dependent anisotropic exchange interactions that underpin the magnetic behavior of $ErCl_3$. By leveraging state-of-the-art experimental setups and data analysis techniques, this work seeks to elucidate the underlying mechanisms that drive the observed magnetic phenomena. Through this exploration, we aim to contribute to the broader understanding of anisotropic exchange interactions and their role in stabilizing exotic quantum states of matter.

4.1.1 Contributions

Attention was guided to the investigation of these materials by K. A. Ross. Synthesis was performed by A. Treglia and J. R. Neilson. Magnetization measurements and analysis were performed by A. Treglia. Air-Sensitive components were fabricated by A. Treglia and J. Breitschopf. Inelastic neutron experiments and analysis were performed by A. Treglia, D. Yahne, J. R. Neilson, J. Lass, and D. Mazzone.

4.2 Synthesis

In this work, we synthesized large single crystals of $ErCl_3$ using the modified Bridgman method discussed in Section 2.2.2. This approach was selected over alternative techniques

such as chemical vapor transport (CVT) and flux growth due to its ability to produce high-purity crystals without requiring transport agents or residual flux that could introduce impurities or complicate post-growth processing, as well as its simple solution to scalability. The modified Bridgman method was optimized based on prior work with rare-earth trihalides, incorporating refinements in ampoule preparation, temperature control, and post-growth handling to improve crystal quality and reproducibility. Given the highly hygroscopic nature of $ErCl_3$, extensive precautions were taken to maintain an air-free environment throughout the synthesis process, from precursor preparation to final sample storage.

The synthesis began with thorough cleaning and drying of quartz ampoules to remove surface contaminants and residual moisture, both of which can compromise the integrity of the crystal growth process. Ampoules were first cleaned by sequential washes with organic solvents and deionized (DI) water to dissolve organic residues and remove particulates. After rinsing, they were baked overnight at 160°C to eliminate any remaining surface-adsorbed moisture. The ampoules were then flame-dried under vacuum ($\sim$10 mTorr) to remove any residual water molecules, ensuring that the inner walls were completely dry. To prevent re-exposure to ambient air, the ampoules were transferred into the glovebox under vacuum using a sealed transfer system consisting of a series of KF flanges and an intermediate ball valve. This method ensured that the ampoules remained isolated from moisture throughout the transfer process. Once inside the glovebox, commercially purchased $ErCl_3$ powder (99.9% REO, Alfa Aesar) was loaded into the ampoules under an argon atmosphere. Using the same sealed transfer system, the loaded ampoules were then transported back to the vacuum line, where they were evacuated to $\sim$10 mTorr before being permanently sealed with a methane-oxygen torch. This ensured that the ampoules remained air-free throughout the entire process, preserving the integrity of the precursor material before growth.

The sealed ampoules were placed in a temperature-controlled tube furnace, where the heating profile (Fig. 4.1a) was optimized to promote high-quality single-crystal growth while minimizing thermal stress and unwanted nucleation effects. The furnace was first heated to

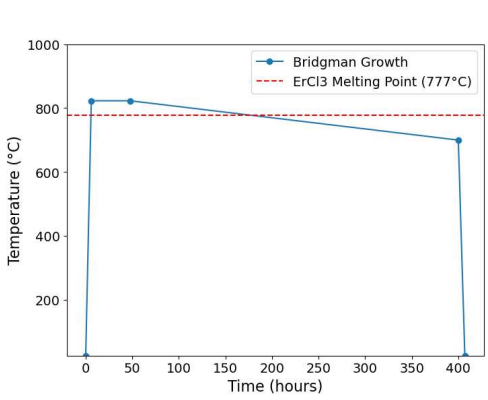

(a)

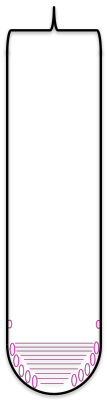

(b)

Figure 4.1: (a)Temperature profile for $ErCl_3$ crystal growth using the modified Bridgman method. The schedule includes the initial heating phase above the melting point, an extended hold at 823°C, and a gradual cooling period to well below the melting point (red dashed line) over 1–2 weeks to promote high-quality crystallization. A final furnace-cooling step completes the process. (b) Diagram illustrating cross-section of $ErCl_3$ growth ampoule after synthesis has been completed. Open circles represent the polycrystalline areas close to the quartz ampoule walls and lines indicate the crystallized core.

about 50°C above the melting point of $ErCl_3$, which is reported to be 776°C [87], over several hours to ensure complete melting of the precursor material. The melt was then held at this temperature for an extended period to allow for full homogenization and to reduce thermal fluctuations. Avoiding excessive overheating was crucial, as it could increase the volatility of molten $ErCl_3$, leading to splashing on the ampoule walls and possible dissociation into elemental Er and Cl gases. The cooling process was carefully controlled to optimize crystallinity and prevent the formation of polycrystalline grains. The temperature was gradually reduced to about 100°C below the melting point, followed by a natural furnace cool to room temperature. This temperature schedule was refined to account for variations in furnace accuracy, as different furnaces exhibited inconsistencies in reported temperatures and in which zones were accurately measured. These refinements ensured reproducible growth conditions and enhanced the uniformity of the resulting single crystals.

After cooling, the ampoule contained a large crystalline mass surrounded by a polycrystalline crust, as illustrated in Fig. 4.1b. To retrieve the single-crystal core, the ampoule was scored with a diamond saw and broken open inside the glovebox to prevent exposure

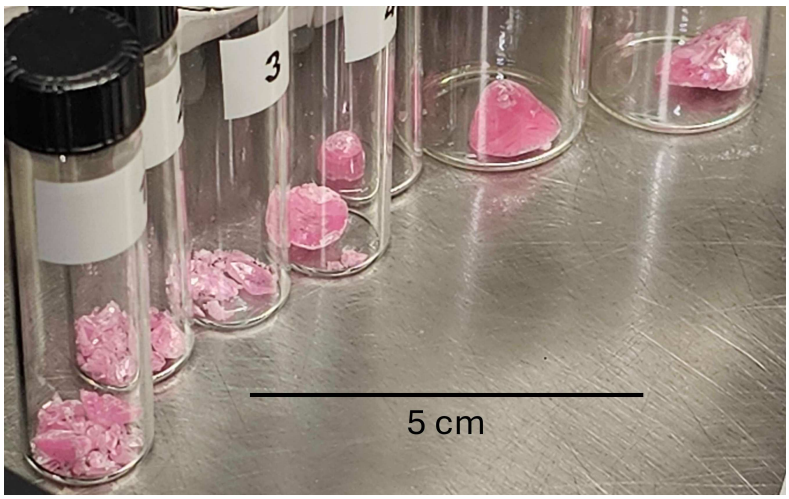

Figure 4.2: $ErCl_3$ Single Crystals After Synthesis—Photograph of synthesized $ErCl_3$ single crystals stored in labeled glass vials. The crystals exhibit a distinct pink hue, with sizes ranging from small fragments to larger pieces. The scale bar represents 5 cm, providing a reference for the crystal dimensions.

to air. The polycrystalline crust was mechanically removed using a fine blade, revealing a well-formed single crystal typically measuring several millimeters to centimeters in size. The final product was stored in an argon-sealed container to prevent degradation before further characterization. The relative fraction of single-crystal material to polycrystalline byproduct could be improved by refining the temperature setpoints, controlling the cooling rate, and optimizing the sealed ampoule geometry. Larger crystals could be grown by increasing the precursor load, though this required careful tuning of growth parameters to prevent excessive strain within the sample. These refinements collectively enhanced the reliability and reproducibility of the modified Bridgman technique for $ErCl_3$, ensuring the production of high-quality single crystals (as pictured in Fig. 4.2) suitable for neutron scattering and other experimental investigations.

4.3 Air-Sensitive Handling Techniques

When exposed to atmospheric moisture, $ErCl_3$ rapidly absorbs water and forms the hydrate, $ErCl_3 \cdot 6H_2O$. This behavior is common among lanthanide chlorides due to their high

Figure 4.3: Degradation of $ErCl_3$ Crystals Upon Air Exposure—Image showing $ErCl_3$ single crystals after exposure to ambient air, resulting in significant hydration and decomposition into a fine, white powder. This transformation occurs due to the hygroscopic nature of $ErCl_3$, which rapidly absorbs moisture and forms $ErCl_3 \cdot 6H_2O$, leading to structural collapse and deliquescence.

charge density and strong affinity for polar water molecules [88, 89]. This hydration process is energetically favorable, resulting in a structural transformation that significantly alters the physical properties of the compound. In many cases, the combination of hygroscopicity and weak interlayer interactions leads to deliquescence, where the solid absorbs sufficient water to dissolve into solution. Any exposure to ambient atmospheric conditions will cause $ErCl_3$ crystals to degrade into a fine white powder within hours (Fig. 4.3). Even momentary exposure to air can initiate significant degradation, as moisture rapidly reacts with the crystal surface. Once exposed, the damage is irreversible, as moisture-induced structural changes cannot be undone, even upon returning to an inert environment. This extreme sensitivity necessitates that all handling and experimental procedures be performed under strictly inert or dry conditions

to prevent rapid degradation and preserve the crystalline quality. To address this challenge, extensive efforts were made to develop air-free methods for sample preparation and measurement, leading to the majority of experimental work being conducted inside an argon-filled glovebox.

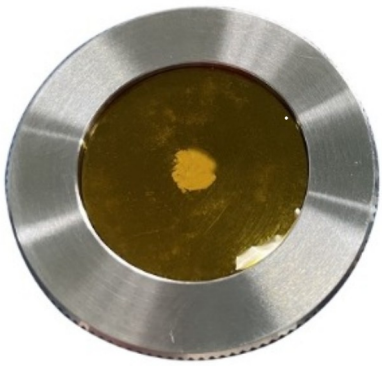

Figure 4.4: Air-Free Powder X-ray Diffraction (PXRD) Sample Preparation—Image demonstrating the air-free method for PXRD measurements, where a powder sample is sealed onto a zero-diffraction plate (ZDP) using Kapton tape. This technique prevents moisture contamination and degradation during data collection, ensuring the integrity of air-sensitive samples.

For powder X-ray diffraction (PXRD), an air-free mounting technique was necessary to prevent moisture contamination during measurements. Samples were sealed onto the zero-diffraction plate (ZDP) under an inert atmosphere using Kapton tape (Fig. 4.4). While Kapton tape introduces minor background noise at lower 2θ angles, it remains a widely used and effective sealing method for protecting air-sensitive samples. All sample preparation steps, including mounting onto the ZDP, were performed inside the glovebox to minimize air exposure and prevent sample degradation during data collection.

For Laue diffraction, we developed a sealed Air-Tight Module (ATM) to allow samples to be mounted in an argon-filled environment and transferred to the Laue X-ray system without exposure to ambient air. This design was inspired by a previous method developed for neutron scattering on air-sensitive materials [90] and adapted for use in X-ray alignment. The ATM functioned as a fully enclosed chamber, isolated from the surrounding atmosphere by tightening a KF50 clamp around its outer perimeter. The front side featured a transparent elastic window, which permitted X-rays to pass through while also enabling in situ crystal adjustments. Sample positioning could be fine-tuned in situ by gently pressing a Q-tip against the elastic film, allowing adjustments without breaking containment. To ensure reproducibility and stability during measurements, the ATM was mounted inside the Laue

(a) (b) (c)

Figure 4.5: Air-Tight Module used for air-free Laue diffraction and crystal orientation. (a) Exploded view. (b) Assembled view. (c) Mounted in the Laue X-ray cabinet with a custom 3D printed holder.

cabinet using a custom 3D-printed holder, which provided a secure and consistent alignment for all samples.

Beyond its role in Laue diffraction, the ATM was designed to be highly modular, making it adaptable to different custom sample stages, as well as transportation and neutron scattering canisters. This adaptability made it a versatile tool for handling air-sensitive materials across multiple experimental setups while maintaining an inert environment. By swapping out internal mounting components, the ATM could be configured to securely hold different sample holders, ensuring compatibility with various techniques. This design was particularly useful for measurements requiring air-free sample transfer between preparation environments and experimental apparatus. One such application involved the use of the ATM alongside custom 3D-printed sample stages for magnetization measurements, ensuring that air-sensitive samples remained fully protected throughout the process.

To facilitate air-free magnetization measurements, we developed custom 3D-printed PLA (polylactic acid) sample stages, chosen for their negligible magnetic signal. These stages were designed to be fully compatible with the ATM, allowing samples to be first aligned using Laue diffraction before being sealed inside a glovebox for transportation. To ensure an airtight seal, a thin layer of GE varnish (7031) was applied to the vertical sides of the upper tier of the stage, where the cap would slide down and make contact, preventing any exposure to ambient air. Once sealed, the entire assembly could be directly integrated into the MPMS by

(a) (b)

Figure 4.6: CAD models of custom 3D printed sample stages designed for the MPMS. (a) Standard 3D-printed sample stage designed for air-free sample handling and integration with experimental setups. (b) Modified vertical stage, allowing for alternative mounting orientations while maintaining an inert environment. Both designs were developed for compatibility with the Air-Tight Module (ATM), enabling seamless transfer between preparation and measurement environments without air exposure.

inserting the sealed stage into the end of a standard straw. This approach provided a fully air-free workflow, protecting sensitive samples throughout the measurement process. The design relied on mechanical mounting, with a removable cap securing the sample in place, eliminating the need for adhesives or additional fasteners. Additionally, the flexibility of 3D printing allowed for customized mounting angles, making it possible to position samples at arbitrary orientations with respect to the applied magnetic field—an approach that could be useful for future angular-dependent magnetization studies.

The standard procedure for heat capacity measurements only required slight modification to accommodate the air sensitivity of $ErCl_3$. The PPMS heat capacity puck was first brought into the glovebox, where the sample was carefully placed on the sapphire stage using a light coating of N-grease (Apiezon) to ensure thermal contact. In standard procedures, a small vacuum assembly stabilizes the sapphire stage, preventing excessive pressure during sample placement. However, in the glovebox, this step had to be performed manually, requiring extra care to avoid damaging the delicate stage. The stage itself is suspended on fragile Kapton tubes and gold wires, making it particularly susceptible to damage if pressed down

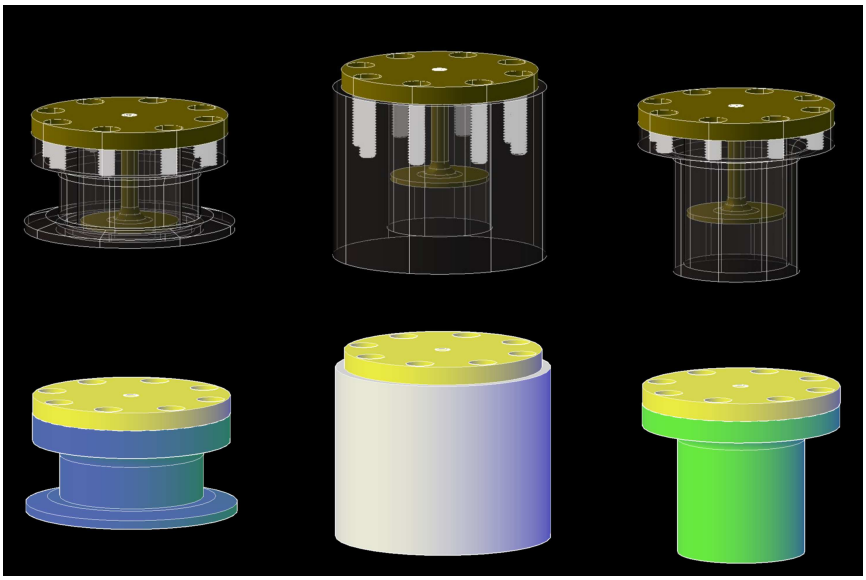

Figure 4.7: CAD renderings of the modular Air-Tight Module (ATM) system designed for air-free preparation, transportation, and execution of neutron scattering experiments. The top row shows X-ray-style views, while the bottom row presents solid models. The yellow component in all configurations represents the sample stage, which serves as the mounting base for all interchangeable modules. From left to right, the ATM is shown with three different front-end attachments: the Laue diffraction adapter (blue) for crystallographic alignment, the polycarbonate transportation can (white) for secure and transparent air-free transport, and the neutron scattering can (green) for direct integration with the experimental setup. This modular design ensured seamless transitions between each stage while maintaining an inert environment.

too forcefully. This added an element of risk and required extra care when positioning the sample. Once mounted, the puck was carefully transported to the PPMS and inserted into the measurement system. The brief exposure during this transfer process was insufficient to cause significant sample degradation, as the N-grease layer effectively minimized contact with ambient air. This approach ensured that high-quality heat capacity data could be collected without compromising the integrity of the sample.

Conducting neutron scattering experiments on air-sensitive $ErCl_3$ required a fully sealed workflow, ensuring sample integrity during neutron scattering experiments required a fully sealed workflow, spanning coalignment, transport, and integration into the instrument. To achieve this, we designed a modular Air-Tight Module (ATM) system, which enabled samples to remain isolated from ambient air at every stage of the experiment.

The first step was to develop a sample stage that was compatible with a dilution refrigerator system used in neutron scattering experiments, serving as the base of the ATM. This sample stage was then modified by machining eight threaded holes (M6×1) into the base, allowing it to integrate with the ATM system. This design enabled interchangeability between three different modules: (a) the Laue diffraction module, (b) the transportation module, and (c) the neutron scattering module, each of which could be swapped inside a glovebox without breaking containment. Fig. 4.7 illustrates the ATM's modular design, showing its different configurations. These interchangeable components highlight the system's adaptability for each stage of the experiment.

For crystal coalignment, the sample stage was first mounted inside the ATM-Laue module (Fig. 4.8a). This setup consisted of an SS-ATM Adapter, which on one side mated to the sample stage via the M6 screws and an O-ring, and on the other side was connected to a KF50 blank flange window secured by a KF50 clamp. Between the adapter and the blank window flange, a spacer with an O-ring ensured a tight seal around the elastic polymer film, which acted as the observation window. A proper seal was confirmed by the slight positive pressure buildup inside the ATM, which caused the elastic window to bow outward into a concave shape as the clamp was tightened.

Once sealed in the glovebox, the ATM-Laue module was transported to the Laue X-ray system and mounted using a custom 3D-printed holder (Fig.4.5c). The initial orientation of each crystal was determined, after which a Q-tip was used to nudge the crystal into the desired position through the elastic window. To allow for iterative adjustments, crystals were initially held in place with putty, which provided temporary adhesion without restricting realignment (Fig. 4.8b). Once the final orientation was achieved, the ATM was returned to the glovebox, where the putty was removed and a small amount of GE varnish (7031) was applied to permanently fix the crystal in place. This process was repeated until the sample stage was fully loaded with coaligned crystals.

After coalignment, the Laue module was swapped for the transportation module. The

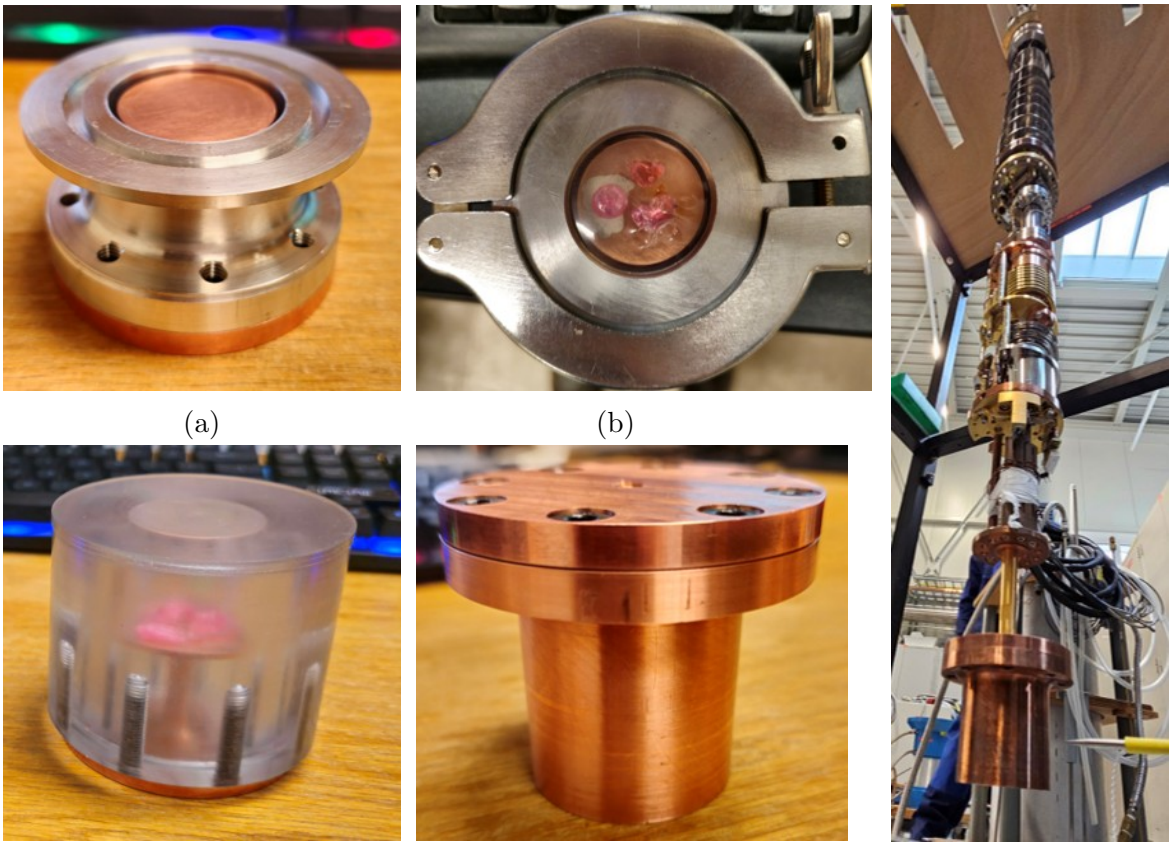

Figure 4.8: The Air-Tight Module (ATM) at various stages of air-free sample handling and experimental integration for $ErCl_3$ neutron scattering studies. (a) ATM in its Laue diffraction configuration, with the sample stage secured to the Laue adapter. (b) A view through the transparent elastic film, showing $ErCl_3$ crystals inside the ATM during Laue orientation. (c) The transportation module, designed with a transparent polycarbonate can to ensure airtight transport while allowing visual inspection. (d) The neutron scattering (NS) module, featuring a fully sealed copper sample can for integration into a dilution refrigerator system. (e) The NS module fully assembled and attached to the dilution refrigerator probe for the CAMEA instrument.

transportation can consisted of a well-polished polycarbonate cylinder, designed with threaded holes and a groove for an indium wire seal, allowing it to securely mate with the sample stage (Fig. 4.8c). The polycarbonate enclosure allowed for full visual inspection of the interior, a critical design feature for transportation security, as it enabled customs agents to inspect the contents without opening the container. The indium wire seal was selected for its exceptional robustness, as its soft metal composition filled gaps and created

an airtight, durable seal that could withstand extended transport conditions.

At the neutron facility, the ATM-transportation module was transferred into a glovebox, where the transportation can was replaced with the neutron scattering can, ensuring the sample remained air-free. This experimental can was constructed from Copper 101, ensuring compatibility with low-temperature neutron scattering systems. Like the transportation can, it was secured via M6 screws and an indium wire seal to maintain airtight integrity (Fig. 4.8d). The fully assembled ATM-NS module was then removed from the glovebox and securely mounted onto the dilution refrigerator probe. This final step ensured seamless integration into the neutron instrument while preserving the air-free conditions of the $ErCl_3$ crystals.

This workflow enabled a fully air-free process for sample preparation, transport, and integration into the neutron scattering instrument. The modular design of the ATM ensured that each step—from co-alignment to final mounting—was executed in a controlled, inert environment. Although this system was designed for a specific neutron instrument and dilution refrigerator, the approach is broadly adaptable to other setups. The methodology outlined here can serve as a general framework for future neutron scattering experiments on air-sensitive materials, with modifications as needed to accommodate different instruments and cryogenic setups. Detailed blueprints of all custom-designed components developed for air-free sample handling, including the ATM and associated modules, can be found in Appendix A.

4.4 Experiments

Magnetization measurements were conducted to investigate the anisotropic magnetic response of $ErCl_3$ using the MPMS3 with the ^{3}He option for low-temperature measurements. Samples were mounted in custom 3D-printed holders (Section 4.3) to maintain an air-free environment. The standard stage (Fig.4.6a) was used for measurements with the magnetic

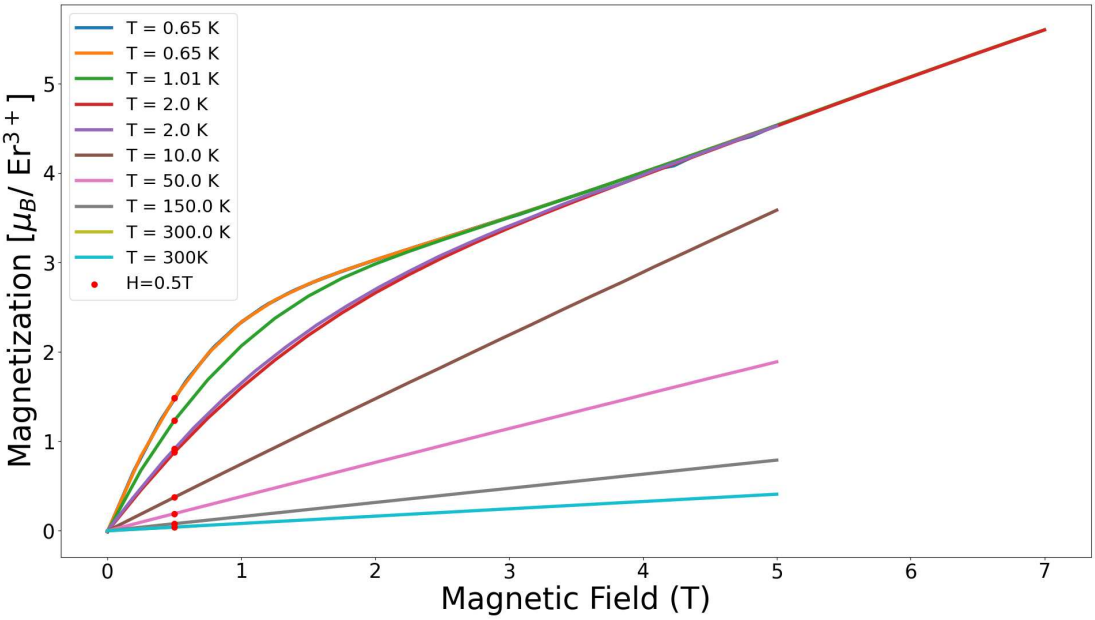

Figure 4.9: A plot of $ErCl_3$ magnetization (M) vs applied magnetic field (H), measured at a variety of different temperatures spanning from 0.65K to 300K. The red dots correspond to magnetization values at H = 0.5T, which are later compared in Fig. 4.10a.

field applied parallel to the crystallographic c-axis ($H \parallel c$), while a modified vertical stage (Fig. 4.6b) was used for $H \parallel ab$, ensuring that the sample was correctly aligned by standing it upright. This method allowed for seamless sample transfer from the glovebox to the MPMS3 while preventing degradation due to air exposure. Achieving precise in-plane ($H \parallel ab$) and out-of-plane ($H \parallel c$) alignment was straightforward, as the layered nature of $ErCl_3$ allowed samples to be cleaved from larger crystals, exposing well-defined ab-plane surfaces. The flat platforms of both 3D-printed stages naturally accommodated these orientations, ensuring reproducibility and ease of alignment. Further refinement to achieve alignment along a specific in-plane direction (H $\parallel$ a or H $\parallel$ b) would require additional Laue diffraction measurements using the ATM system.

Magnetization as a function of applied field, M(H), was measured for $H \parallel c$ at temperatures of 0.65 K, 1 K, and 2 K using the ^{3}He option in DC mode, while additional measurements at 2 K, 10 K, 50 K, 150 K, and 300 K were performed using the base MPMS3 system in Vibrating Sample Magnetometer (VSM) mode. The applied field was swept up to 7 T for the

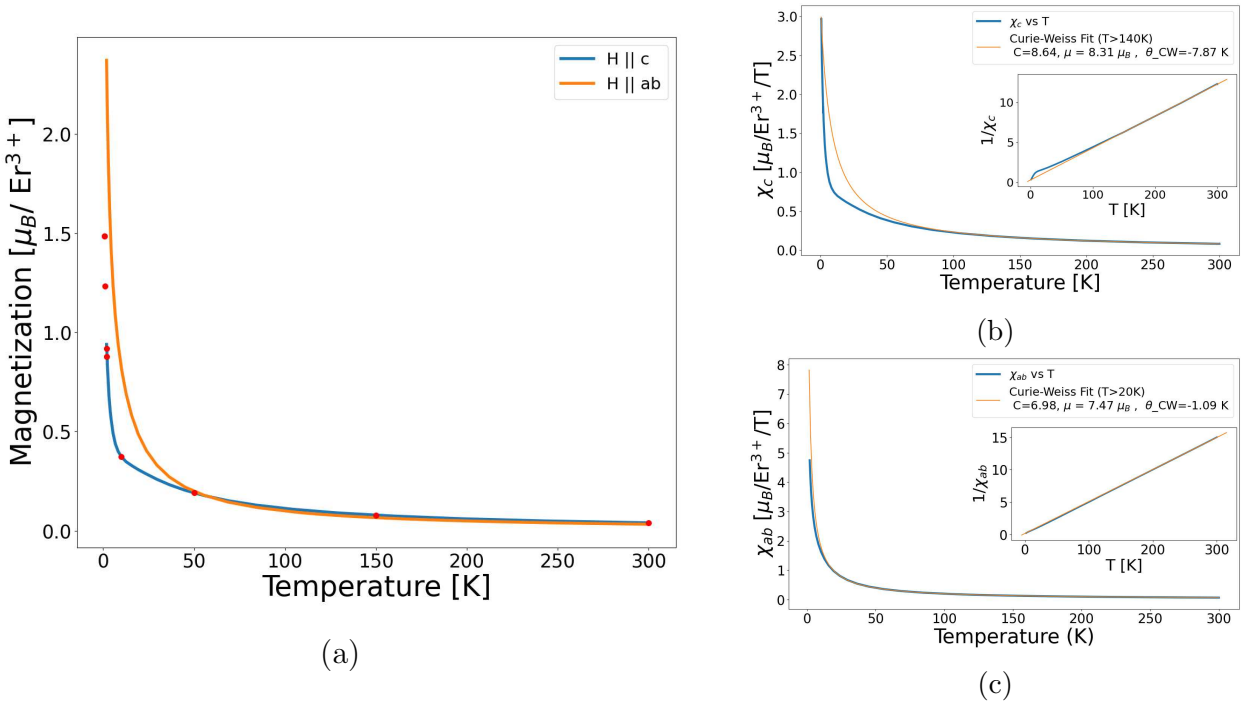

Figure 4.10: (a) Magnetization vs. temperature for $ErCl_3$ with $H \parallel c$ (orange) and $H \parallel ab$ (blue), highlighting clear anisotropy, particularly in the low-temperature regime. (b) Inverse susceptibility $1/\chi$ vs. T for $H \parallel c$, showing deviations from Curie-Weiss behavior below 50K. (c) $1/\chi$ vs. T for $H \parallel ab$, which closely follows Curie-Weiss behavior in the high-temperature regime. The insets in (b) and (c) show the linear Curie-Weiss fits used to extract the effective magnetic moments and Curie-Weiss temperatures for each field orientation.

lowest-temperature measurements and up to 5 T for higher temperatures. At temperatures above 10 K, M(H) displayed a linear dependence with the applied field, consistent with a paramagnetic response. However, at lower temperatures, deviations from linearity emerged, indicating the onset of additional interactions beyond simple paramagnetism. These measurements were performed on different samples, yet yielded highly consistent results across both DC and VSM techniques, demonstrating excellent sample-to-sample reproducibility. The results are summarized in Fig. 4.9.

Temperature-dependent magnetization, M(T), was measured under an applied field of 0.5 T for both $H \parallel c$ and $H \parallel ab$ orientations to directly compare the in-plane and out-of-plane magnetic responses. A clear anisotropy was observed, with M(T) for $H \parallel ab$ exhibiting significantly higher values than for $H \parallel c$, indicating a stronger in-plane magnetic response.

This behavior reflects the intrinsic anisotropy of $ErCl_3$, likely stemming from spin-orbit coupling and the crystal field environment. The M(T) curves for both orientations are shown in Fig. 4.10.

To further characterize the observed anisotropy, inverse magnetic susceptibility, $1/\chi$ vs. T, was analyzed using a Curie-Weiss analysis to extract the effective moment and Curie-Weiss temperature for each orientation. For $H \parallel ab$, the data followed a Curie-Weiss law over a broad temperature range, enabling the extraction of an effective magnetic moment and Curie-Weiss temperature. For $H \parallel c$, deviations from Curie-Weiss behavior below 50 K suggest additional interactions, such as crystal field effects or short-range correlations, influencing the out-of-plane response. The Curie-Weiss fits and extracted parameters for each orientation are presented in Fig. 4.10.

All magnetization data were converted to units of Bohr magnetons per Er^{3+} ion to facilitate comparison with theoretical predictions and previous studies. The extracted effective moments from Curie-Weiss fits highlight the anisotropy: $\mu_{\text{eff},ab} = 7.47\mu_B$ and $\mu_{\text{eff},c} = 8.31\mu_B$, both lower than the free-ion value of $\mu_{\text{eff,free}} = 9.58\mu_B$ for Er^{3+}. This reduction is consistent with the effects of crystal field interactions and spin-orbit coupling in $ErCl_3$. The corresponding Curie-Weiss temperatures were determined to be $\Theta_{\text{CW},ab} = -1.09$ K and $\Theta_{\text{CW},c} = -7.87$ K, indicating stronger antiferromagnetic correlations along the c-axis compared to the ab-plane. The deviation from Curie-Weiss behavior in $H \parallel c$ at low temperatures indicates additional effects influencing the out-of-plane response. These results quantitatively confirm the anisotropic magnetic behavior of $ErCl_3$ and establish a basis for further analysis of its exchange interactions and deviation from ideal Curie-Weiss behavior, which will be explored in later sections.

Neutron scattering experiments were conducted on the Continuous Angle Multiple Energy Analysis (CAMEA) spectrometer at the Paul Scherrer Institute (PSI) (Fig. 4.11b) to investigate the low-energy excitations in $ErCl_3$. CAMEA utilizes the Swiss Spallation Neutron Source (SINQ), which provides a continuous flux of cold neutrons optimized for

(a) (b)

Figure 4.11: (a) Schematic representation of CAMEAs multi-analyzer array, which enables simultaneous detection of eight final energy channels, each covering an azimuthal range of 60° in the horizontal plane. The analyzer-detector bank can be rotated to different 2θ angles, while the sample angle θ_s can also be adjusted for alignment and optimized momentum-space coverage. (b) Photograph of the CAMEA spectrometer at the Swiss Spallation Neutron Source (SINQ), showing the experimental setup.

high-resolution spectroscopy. Designed specifically for mapping out low-energy magnetic excitations in the horizontal plane, CAMEA is well suited for studying the spin dynamics within the honeycomb plane of $ErCl_3$. Traditional triple-axis spectrometers (TAS) measure individual $(\boldsymbol{Q}, \omega)$ points through stepwise scanning, while time-of-flight (TOF) spectrometers collect large $(\boldsymbol{Q}, \omega)$ regions at once but sacrifice energy resolution. CAMEA combines the strengths of both, achieving broad $(\boldsymbol{Q}, \omega)$ coverage while maintaining high energy resolution. The spectrometer employs a multi-analyzer array that splits the horizontally scattered neutrons up into eight distinct final energy detectors (linear position sensitive ^{3}He detector tubes) mounted radially, each covering 60° azimuthally in the horizontal plane, illustrated in Fig. 4.11a. This configuration allows CAMEA to efficiently map excitations across a broad momentum-energy range while maintaining high energy resolution (0.1 meV). By combining this multiplexed energy analysis with sample rotation and an independently rotating analyzer-detector bank, CAMEA is capable of rapidly measuring large regions of $(\boldsymbol{Q}, \omega)$ space while preserving the resolution necessary for resolving low-energy excitations [91, 92].

For this experiment, eight single crystals of $ErCl_3$, with a combined mass of approximately 4 grams, were co-aligned in the (HK0) plane using Laue X-ray diffraction before being

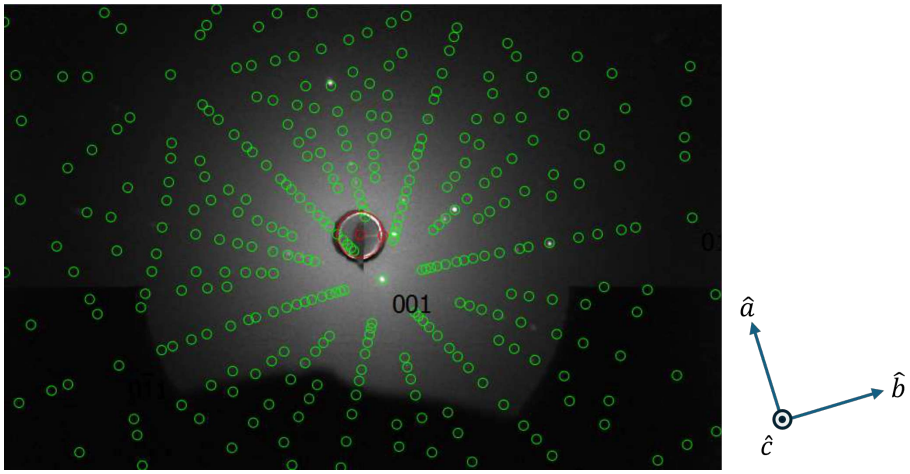

Figure 4.12: Example of Laue orientation of $ErCl_3$ crystal with crystallographic axes shown to the right. Green circles show the fit to the C2/m monoclinic structure. White dots indicate the (HKL) planar reflections from X-ray diffraction. Shadows seen near the bottom are from the putty and ATM module used for air-free orientation. The (001) reflection is slightly offset from the center due to alignment with $\hat{c}$ rather than $\hat{c}^*$.

sealed inside an air-free sample transport canister as part of the Air-Tight Module (ATM) system. This approach ensured that the highly air-sensitive material remained protected from degradation throughout transport and integration into the spectrometer. The sealed sample assembly was then installed in the dilution refrigerator and cryomagnet system, which is capable of reaching base temperatures as low as 30 mK and applying a vertical magnetic field of up to 11T.

The experimental plan was designed to measure the spin excitation spectrum of $ErCl_3$ in both the zero-field ground state and the field-polarized state, while also collecting data for background subtraction at elevated temperatures. Incident neutron energies were selected in the range of 3.75 to 10 meV, allowing for energy transfers spanning -1.5 to 7 meV, optimizing the detection of low-energy excitations. For the field-polarized spin wave measurements, a 5T magnetic field was applied along the crystallographic c-axis, perpendicular to the a^*b^*-plane. This orientation allowed for the measurement of in-plane spin correlations within the honeycomb layers, where dispersions could be modeled using linear spin-wave theory (LSWT) to extract the effective exchange interactions. Zero-field measurements were planned to provide the first characterization of the intrinsic spin excitation spectrum in the absence

of an applied field. Additionally, a higher-temperature scan at 2K was included to aid in background subtraction, distinguishing intrinsic magnetic excitations from thermally driven scattering.

However, during international transport, the co-aligned crystal assembly was mishandled by customs officers, resulting in misalignment of the originally coaligned samples. Due to time constraints, full realignment was not feasible before the experiment, necessitating an alternative approach to data analysis. Rather than treating the sample as a single-crystal measurement, the data were instead powder-averaged by integrating over constant values of $|\boldsymbol{Q}|$, effectively treating the misaligned assembly as a quasi-powder sample. While this compromised the ability to resolve momentum-dependent dispersions along specific crystallographic directions, it still allowed for a meaningful investigation of overall scattering intensity as a function of energy transfer.

Since the crystal misalignment necessitated a powder-averaging approach, the data analysis process became significantly more straightforward. Rather than treating the scattering data as a function of two in-plane momentum components, energy transfer, and intensity—leading to a four-dimensional dataset—the powder-averaging method allowed us to effectively reduce the dimensionality to two, considering only energy transfer and the magnitude of the total momentum transfer, $|\boldsymbol{Q}|$. While this simplification came at the cost of losing directional momentum resolution, it provided a clean way to analyze the excitation spectrum without introducing unnecessary complexity. This is certainly not the type of measurement for which the CAMEA spectrometer was designed, as its strength lies in resolving dispersive excitations in well-aligned single crystals. However, by leveraging the powder-averaged approach, we were able to extract meaningful insights into the scattering intensity distribution as a function of energy transfer, effectively making the best of an otherwise unfavorable experimental condition.

The series of intensity maps shown in Fig. 4.13 presents selected energy transfer slices from one of the field-polarized scans at 65 mK and 5 T. While only nine representative

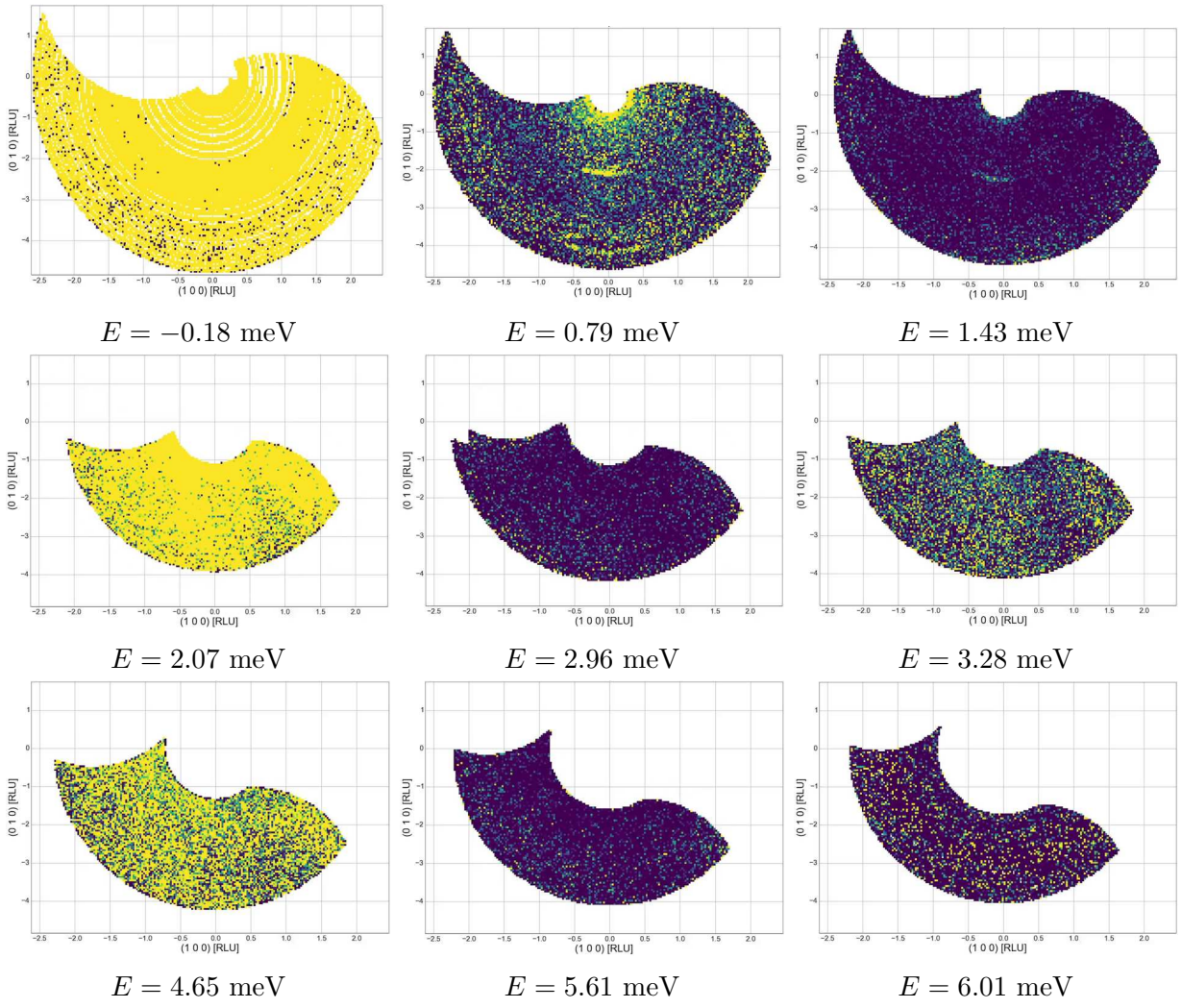

Figure 4.13: Slices of neutron scattering intensity in $ErCl_3$ at $T = 65$ mK and $H = 5$ T. Each panel represents a constant energy transfer slice, showing the distribution of scattering intensity as a function of momentum transfer in the $(H00)$ and $(0K0)$ directions. The horizontal and vertical axes correspond to crystallographic momentum components within the honeycomb plane, while the intensity (color scale) indicates the measured neutron scattering signal at each (H, K) point for a fixed energy transfer E. The shared colormap allows for direct comparison of intensity variations across energy slices.

slices are shown here, it is important to note that the full dataset consists of a much larger set of frames. For this particular temperature and field condition, eight different incident neutron energies were used, and each scan at a given incident energy simultaneously captured intensity at eight different final energy values. As a result, the complete dataset for this condition comprises 64 energy transfer frames. Although it would be ideal to present this as

an animation or interactive figure, such a format is not suitable for a printed dissertation.

These intensity maps reveal the expected semicircular distribution of $(\boldsymbol{Q}, \omega)$ space around $(HKL) = (000)$, which arises from the geometry of the detector bank and the constraints imposed by the available scattering angles. Across the different energy transfer slices, we observe an overall modulation of scattering intensity, with the entire field of view becoming systematically brighter or darker as energy transfer increases. This trend is more clearly visualized in the upcoming powder-averaged representations. Additionally, we observe diffuse scattering features near $(0, \bar{2}, 0)$ and $(0, \bar{4}, 0)$ on the intensity scale. These features are likely associated with low-energy excitations, either phononic or magnonic in origin, but due to the poor sample alignment, they appear significantly broadened along portions of the constant-$|\boldsymbol{Q}|$ rings. While this broadening limited the ability to extract detailed momentum-dependent information, the presence of distinct scattering features at specific $|\boldsymbol{Q}|$ values serves as strong evidence that the samples remained crystalline and undegraded throughout transport and integration into the neutron instrument. This result supports the effectiveness of the ATM system in enabling air-free handling, reinforcing its viability for future neutron scattering experiments on highly air-sensitive materials. Consequently, the subsequent analysis focuses on intensity trends as a function of energy transfer and total momentum magnitude, which remain well-defined despite the misalignment.

Since the misalignment of the sample assembly prevented resolution of dispersions along specific crystallographic directions, the data analysis was simplified by reducing the dimensionality of the dataset. Instead of analyzing intensity variations as a function of energy and two in-plane momentum transfer components $(H00)$ and $(0K0)$, the data were averaged over constant $|\boldsymbol{Q}|$ values, effectively treating the sample as a powder. This dimensional reduction collapses the data from four to three variables—leaving energy transfer E on the y-axis, total momentum transfer magnitude $|\boldsymbol{Q}|$ on the x-axis, and intensity represented through a colormap.

By averaging over all crystallographic directions at a fixed $|\boldsymbol{Q}|$, the resulting intensity

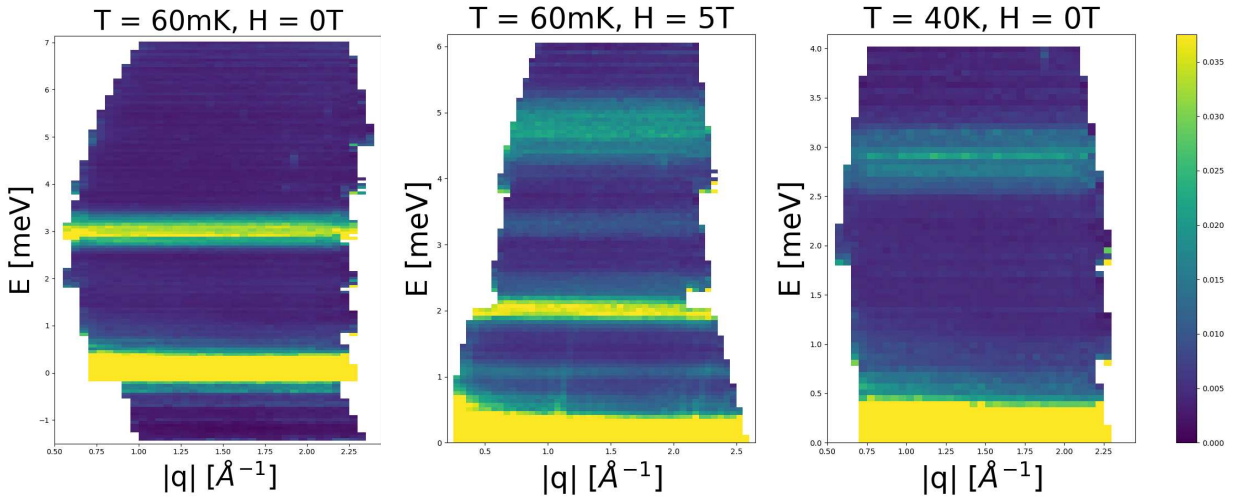

Figure 4.14: Powder-averaged neutron scattering intensity in $ErCl_3$ at different temperature and field conditions. Each panel shows the evolution of intensity as a function of energy transfer and total momentum transfer magnitude, $|\boldsymbol{Q}|$. The colormap is shared across all three panels to allow direct comparison of intensity distributions.

maps provide a more robust and interpretable representation of the overall scattering response. This approach leverages the natural symmetries of a powder-averaged sample, ensuring that observed features arise from intrinsic material properties rather than specific momentum-space artifacts caused by crystal misalignment. Although this transformation sacrifices directional resolution, it enables a clear identification of energy-dependent scattering features. In particular, any excitation modes, whether magnonic or phononic, should appear as dispersing intensity variations along the $|\boldsymbol{Q}|$-axis, provided that their signal remains sufficiently strong after averaging.

To visualize these effects, Fig. 4.14 presents three such powder-averaged datasets corresponding to different temperature and field conditions. These plots reveal how the overall scattering intensity evolves as a function of $|\boldsymbol{Q}|$ and energy transfer, highlighting any systematic trends in excitation spectra. In subsequent analyses, further dimensional reductions will be performed by integrating over all $|\boldsymbol{Q}|$ values, yielding purely energy-dependent intensity plots that facilitate direct comparisons with theoretical models.

Examining the powder-averaged data, several key features emerge. First, we observe

intensity that is largely independent of $|\boldsymbol{Q}|$ but varies as a function of energy transfer, consistent with localized crystal field excitations. These excitations, arising from transitions between different crystal field-split states of the Er^{3+} ions, are expected based on the single-ion energy level scheme discussed in Section 2.1.3 and 2.2.6. Their lack of momentum dependence suggests that they originate from purely local processes rather than dispersive collective excitations.

Additionally, weak streaks of intensity emanating from the elastic line at finite $|\boldsymbol{Q}|$ values can be seen. These features are likely instrumental artifacts, or spurions, arising from multiple scattering or unintended detector responses within the CAMEA setup.

Finally, at low but nonzero energy transfers, we observe faint intensity modulations with some dependence on $|\boldsymbol{Q}|$. These could correspond to low-energy phononic or magnonic excitations that were not fully resolved under the experimental conditions. Due to the crystal misalignment and subsequent powder averaging, any sharp dispersions in these modes would appear broadened or washed out, limiting the ability to extract well-defined dispersion relations. Nevertheless, these features suggest the presence of low-energy dynamic modes, warranting further investigation in future experiments with better sample alignment.

After reducing the dimensionality from four to three by powder averaging, we can further simplify the data by integrating over all values of $|\boldsymbol{Q}|$ to obtain energy-dependent cuts. This final reduction collapses the data into a two-dimensional intensity vs. energy transfer plot, providing a direct visualization of the spectral weight distribution. By summing intensity over all accessible $|\boldsymbol{Q}|$, these energy cuts enhance signal-to-noise and allow for a clearer identification of energy-resolved features that may have been less apparent in the full $(\boldsymbol{Q}, \omega)$ maps.

This representation is particularly useful for identifying non-dispersive excitations, such as crystal field levels, which should manifest as well-defined peaks at specific energy transfers. Additionally, this method suppresses spurious instrumental artifacts that may appear at specific $|\boldsymbol{Q}|$ values, further clarifying the intrinsic spectral features. Comparing energy

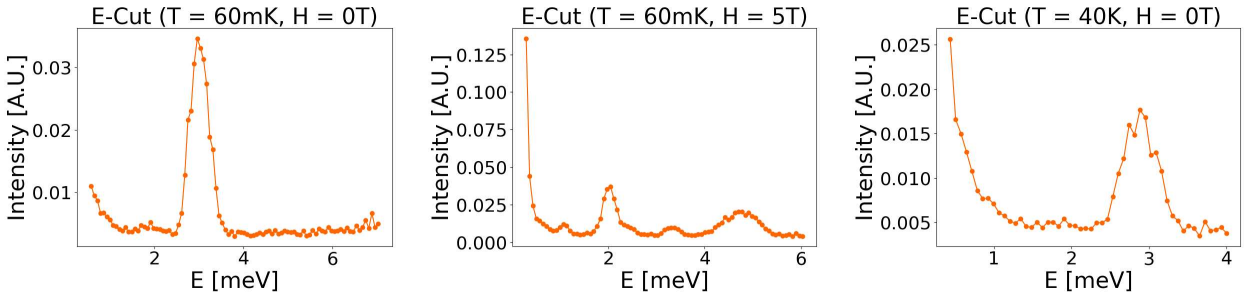

Figure 4.15: Energy-dependent neutron scattering intensity in $ErCl_3$ obtained by integrating over all values of $|\boldsymbol{Q}|$. Each panel represents an energy cut at different temperature and field conditions, revealing non-dispersive crystal field excitations. The comparison across different conditions highlights the evolution of excitation intensity with temperature and applied field.

cuts across different temperatures and applied fields provides insight into the evolution of magnetic and lattice dynamics in $ErCl_3$, revealing which excitations persist, shift, or broaden under varying conditions.

In the energy-dependent cuts shown in Fig. 4.15, several spectral features can be observed. To enhance visibility of these features, the low-energy transfer region (E <0.5 meV) has been omitted, as the intense elastic scattering would otherwise dominate the intensity scale. In the low-temperature, zero-field dataset (T=60 mK, H=0 T), a strong peak is observed near 3 meV, with a weaker feature appearing around 1.8 meV. Upon applying a 5T field at low temperature, the excitation spectrum exhibits additional structure, now showing four distinct peaks across the measured energy range. At elevated temperature (T=40 K, H=0 T), the 3 meV peak remains prominent, and the weaker 1.8 meV peak may also persist, though with reduced intensity. Additionally, there is some indication of spectral weight near the elastic line, at or below 1 meV, suggesting the presence of additional low-energy modes or quasielastic contributions. Tracking the evolution of these features under different conditions offers insight into the excitation spectrum, which will be explored in later sections.

4.5 Discussion

The magnetization and neutron scattering measurements presented in this section pro-

vide a foundation for analyzing the magnetic properties of $ErCl_3$, albeit with significant experimental limitations. The anisotropic magnetization response suggests strong crystal field effects governing the single-ion behavior of Er^{3+}, while deviations from Curie-Weiss behavior at low temperatures indicate additional interactions beyond simple paramagnetic moments. These observations are consistent with expectations for an easy-plane system, where in-plane magnetic interactions dominate the response, and suggest that further modeling will be necessary to fully understand the nature of the interactions in this system.

For the neutron scattering data, the unavoidable sample misalignment required a powder-averaged treatment, collapsing the data into intensity as a function of $|\boldsymbol{Q}|$ and E, thereby removing directional dependence. While this significantly simplified the data analysis, it came at the cost of resolving dispersive spin wave excitations, which could have provided direct constraints on exchange interactions. However, this does not render the data useless—powder-averaged scattering remains a valuable tool for identifying localized excitations, such as crystal field levels, and searching for hints of collective modes that could still provide insight into the magnetic Hamiltonian.

A key next step will be the construction of a point charge calculation to estimate the expected crystal field (CEF) energy levels. However, this will be highly challenging due to the limited number of observed spectral features. The splitting of the two low-temperature, zero-field peaks into four distinct peaks under an applied 5T field does provide some experimental constraints, but this remains severely underdetermined. Given that the monoclinic crystal structure of $ErCl_3$ allows for full CEF splitting of the ($2J$+1, J=15/2) manifold, we expect 16 energy levels in total. In contrast, only a handful of peaks are observed, making an unambiguous determination of the full CEF parameter set infeasible. This difficulty will be addressed in Chapter 5, where we will explore potential theoretical models and discuss the limitations of extracting CEF parameters from such an incomplete dataset.

From a data analysis perspective, the powder averaging allowed for further dimensionality reduction, first collapsing the data to ($|\boldsymbol{Q}|$,E,I) and then to purely energy-dependent intensity

cuts by integrating over all $|\boldsymbol{Q}|$. This final step is justified by the lack of clear dispersive features in the data. While this precludes a direct extraction of exchange interactions from the neutron data, it highlights the presence of low-lying excitation levels that may play an important role in understanding the deviations from typical Curie-Weiss behavior observed in low-temperature thermodynamic data.

The observed spectral peaks, particularly those in the low-temperature, zero-field and field-polarized spectra, strongly suggest that the dominant features in the neutron data correspond to CEF excitations rather than dispersive spin waves. Additionally, weak, diffuse features seen in the energy-momentum slices of the full dataset, as well as possible $|\boldsymbol{Q}|$-dependent intensity modulations near the elastic line in the powder averaged data, may correspond to low-energy phononic or magnonic modes. However, due to the misalignment of the crystal assembly and subsequent powder averaging, any sharp dispersions in these modes would appear broadened or washed out, limiting our ability to resolve them definitively. Fully characterizing these low-energy excitations would require future neutron experiments with improved sample alignment, as well as complementary spectroscopic techniques such as Raman scattering, which is well suited for probing low-energy crystal field excitations.

Chapter 5

Magnetic Interactions in $ErCl_3$

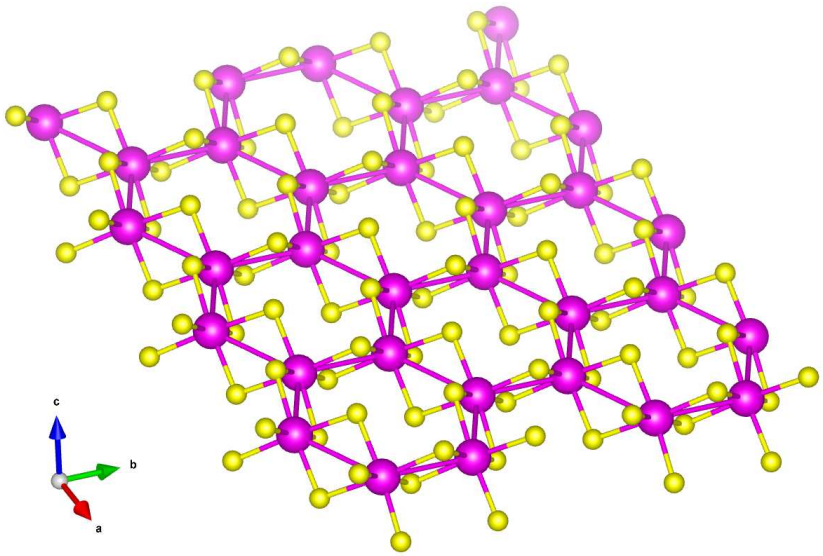

Figure 5.1: Crystal structure of $ErCl_3$ generated by VESTA software. Here only a single layer within the *ab*-plane is shown in order to make the honeycomb net more clearly visible.

5.1 Context

$ErCl_3$ was first studied in bulk form in the 1950s when Templeton and Carter successfully determined its crystal structure using X-ray diffraction. They found that $ErCl_3$ is isostructural with the second half of the lanthanide trichloride series (from holmium to lutetium), crystallizing in the monoclinic space group C2/m [93]. The room-temperature lattice parameters were determined to be $a = 6.8040$ $\AA$, $b = 11.7456$ $\AA$, $c = 6.3187$ $\AA$, and $\beta = 110.8510°$, as shown in Fig. 5.1. The trivalent erbium ions form honeycomb layers within the *ab*-plane, each surrounded by corner-sharing octahedra of chlorine ligands. This structural arrange-

(a)

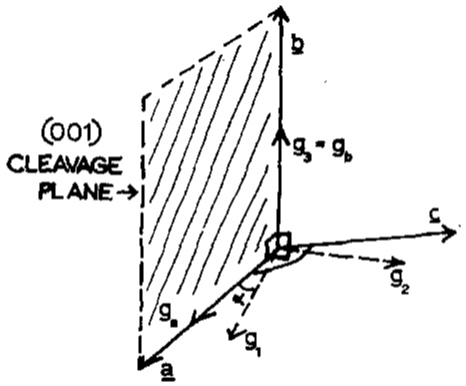

(b)

Ion	Host	g_a	g_1	g_2	g_3=g_b
Er^{3+}	YCl_3	8.29 (±0.03)	8.27 (±0.05)	3.78 (±0.05)	7.70 (±0.03)
Er^{3+}	$LuCl_3$	8.35 (±0.02)	8.34 (±0.02)	3.51 (±0.03)	7.92 (±0.02)

Figure 5.2: Principal g values of Er^{3+} ions in YCl_3 and $LuCl_3$. (a) A diagram showing the directional representation of g values (g_1, g_2, g_3) including the cleavage plane (001) and (b) A table summarizing the EPR experimentally determined g values and their variations, highlighting significant anisotropy between in-plane and out-of-plane values [13].

ment facilitates unique magnetic properties, as the layered geometry introduces a natural frustration to magnetic ordering.

By the 1960s, electron paramagnetic resonance (EPR) and optical fluorescence spectroscopy provided key insights into the single-ion physics of Er^{3+} in $ErCl_3$. Garton et al. [13] determined the principal g-values for Er^{3+} ions using EPR, revealing significant magnetic anisotropy (Fig. 5.2). The strong directional dependence of these values suggests that the erbium moments experience substantial crystal field effects, which split the spin-orbit coupled states of the J=15/2 manifold into a series of (2J+1) non-degenerate energy levels.

Optical fluorescence experiments performed by Rakestraw et al. [14] further refined this picture, revealing the energy gap between the ground-state Kramers doublet and the first excited doublet (Fig. 5.3). The measured gap of 22.26 cm^{-1} (∼32 K) establishes an important energy scale: below this temperature, $ErCl_3$ should behave effectively as a spin-1/2 system, as thermal fluctuations are insufficient to populate higher-lying CEF states. This finding positions $ErCl_3$ as a candidate for bond-dependent anisotropic exchange interactions, where spin-orbit entangled moments give rise to exotic quantum magnetism.

TABLE I. Energy levels of Er^{3+} in YCl_3.[a]

(1)	(2) E (cm^{-1})	(3) λ (Å)	(4) I	(5)	(6) Class.
Z_1	0.00			f	$^4I_{15/2}$
Z_2	22.26			f	
Z_3	24.15			f	
Z_4	60.83			f	
Z_5	66.24			f	
Z_6	256.55			f	
Z_7	289.26			f	
Z_8	291.53			f	
F_1	19 018.30	5 256.63	10*bb*	A	$^2H_{11/2}$
F_2	019.32	256.35	8*blend*	A	
F_3	023.17	255.29	10	A	
F_4	061.14	244.82	10*bb*	A	
F_5	145.69	221.65	10*bbd*	A	
F_6	185.01	210.95	10*bbd*	A	
G_1	20 390.11	4 902.97	8*d*	A	$^4F_{7/2}$
G_2	448.97	888.86	1*bdd*	A	

Figure 5.3: Measured energy levels of Er^{3+} ions in the YCl_3 determined via the absorption and flourescence spectra of Er^{3+} in YCl_3, performed at 4.2°K by Rakestraw et. al [14].

By the early 2000s, neutron scattering experiments significantly advanced the understanding of exchange interactions in $ErCl_3$. Powder and single-crystal neutron diffraction studies revealed a three-dimensional antiferromagnetic (AFM) ordered state with a Néel temperature of $T_N = 350$ mK. The propagation vector of this ordered phase, $\boldsymbol{k} = (2/3, 0, -1/12)$, corresponds to a noncollinear helical structure within the honeycomb layers (Fig. 5.4) [85, 15]. This ordering differs significantly from the simple Néel state observed in $YbCl_3$, indicating that additional interactions, beyond isotropic Heisenberg exchange, influence $ErCl_3$'s magnetic behavior.

The spin structure of $ErCl_3$ consists of two interlocked 120° triangular sublattices, each forming helices with opposite handedness along the c-axis. The ordered moment per Er^{3+} ion was determined to be 3.3 μ_B, significantly reduced from the free-ion value due to crystal field effects that isolate a low-energy Kramers doublet ground state. The persistence of short-range in-plane correlations above T_N further underscores the quasi-2D nature of the system, suggesting that interlayer interactions are weak and that the dominant physics lies within the honeycomb layers.

The temperature dependence of the magnetic Bragg peak intensities yielded a critical exponent ($\beta = 0.23$), consistent with a quasi-2D XY or anisotropic Heisenberg system, where strong in-plane interactions drive the primary magnetic behavior while weak out-of-plane couplings establish long-range order at lower temperatures. While these neutron

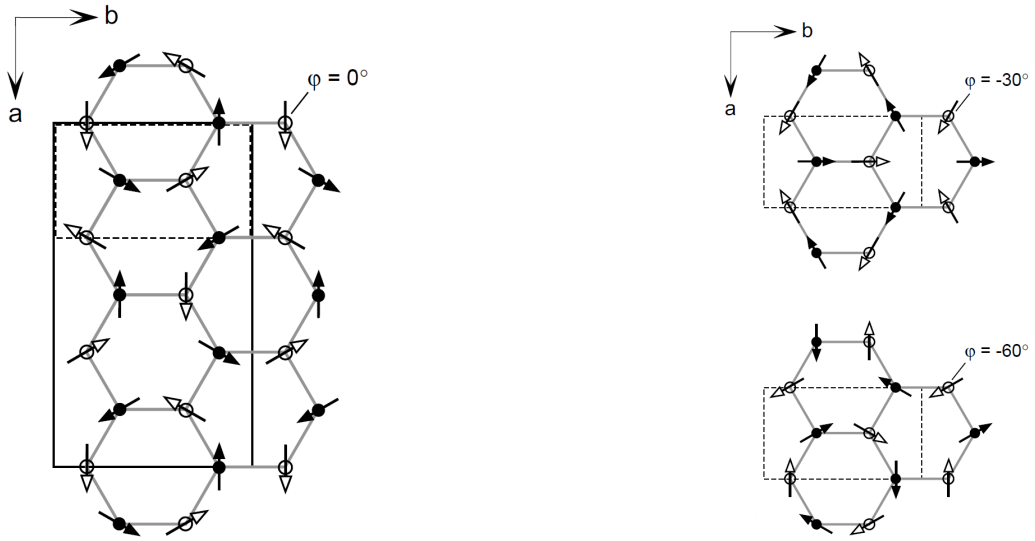

Figure 5.4: Magnetic structure of $ErCl_3$ within the *ab*-plane determined from neutron scattering experiments, performed by Kramer et al. [15]. Here, the structure can be visualized by showing how the spins could be arranged with any arbitrary value of φ. The white and black spins indicate those on either of the counterrotating sublattices.

diffraction experiments successfully resolved the static magnetic structure, they could not determine the microscopic exchange interactions responsible for stabilizing the noncollinear order. At the time, no clear theoretical framework existed to explain how spin-orbit coupling and exchange anisotropy might drive such behavior in rare-earth honeycomb magnets.

A major development in understanding anisotropic magnetism came with the Kitaev model, first proposed in 2006 [77], which introduced a new perspective on bond-dependent exchange interactions in honeycomb lattice materials. Originally formulated for $4d$ and $5d$ transition-metal compounds, the model has since been extended to rare-earth systems, where strong spin-orbit coupling and localized $4f$ moments naturally give rise to exchange anisotropy [79, 78]. Given that previous studies of $ErCl_3$ could not explain its observed noncollinear helical order, the possibility that Kitaev-like interactions—or other forms of anisotropic exchange—play a role in stabilizing this state has emerged as an important open question.

The combination of strong SOC, a Kramers doublet ground state, and a honeycomb lattice geometry makes $ErCl_3$ an ideal system for exploring deviations from a pure Heisen-

berg model. The edge-sharing octahedral coordination of Cl^- ligands creates superexchange pathways that could, in principle, give rise to bond-dependent interactions, similar to those found in Kitaev materials. Whether these interactions are sufficient to explain the non-collinear AFM order observed in neutron diffraction remains uncertain.

To address this, we performed magnetization and neutron spectroscopy measurements to probe both the anisotropic magnetic response and low-energy excitations that could reveal the nature of the exchange interactions. A key challenge arose due to sample misalignment in neutron experiments, which prevented direct extraction of spin wave dispersions that would have allowed for quantitative modeling of exchange parameters. Instead, we analyze the powder-averaged response, considering how, if dispersion were clearly observed, it could have been fitted using various interaction terms. Similarly, while the CEF levels we identified serve as a starting point, they remain insufficient for a full parameter determination.

Despite these limitations, our results establish new constraints on the energy scales governing $ErCl_3$'s magnetism, reinforcing its status as a material where anisotropic interactions influence the magnetic ground state. Whether the exchange Hamiltonian includes significant bond-dependent terms, or if an alternative anisotropic mechanism better explains the observed order, remains an open question. External tuning, such as applied field or pressure, may provide a way to access new phases, including a possible proximate quantum spin liquid state. The following sections explore these ideas further, linking experimental observations to theoretical models and outlining the next steps toward a full characterization of the interplay between single-ion and collective effects in this system.

5.2 $4f^{11}$ Single Ion Physics

During the formation of $ErCl_3$, neutral erbium atoms lose three valence electrons—two from the $6s$ orbital and one from the $5d$ orbital—resulting in trivalent Er^{3+} ions that bond ionically with chlorine anions. This oxidation state leaves 11 electrons in the $4f$ shell, giving

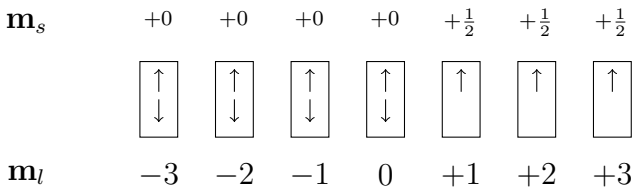

Figure 5.5: Hund's rules filling of the $4f$ orbitals for Er^{3+} in $ErCl_3$. This configuration establishes the fundamental basis for crystal field splitting, as the unpaired electrons in the $4f$ shell experience ligand-induced anisotropy that shapes the CEF Hamiltonian.

Er^{3+} a [Xe] $4f^{11}$ electronic configuration. The filling of these orbitals follows Hund's rules, which dictate that the total spin S is maximized by first occupying all seven available $4f$ orbitals with parallel spins. The remaining four electrons then fill orbitals with antiparallel spins, resulting in three unpaired spin-up electrons and a total spin quantum number of S=3/2. To maximize the total orbital angular momentum L, these unpaired electrons preferentially occupy orbitals with the highest possible magnetic quantum numbers, yielding L=6 (Fig. 5.5).

While Hund's rules establish the fundamental electronic configuration of Er^{3+}, they do not account for the strong interaction between an electron's spin and its orbital motion, known as spin-orbit coupling (SOC). SOC is particularly strong in heavy elements like erbium, where relativistic effects enhance this interaction. In the case of Er^{3+}, SOC couples the spin S and orbital L angular momenta to form a total angular momentum J, given by J=$L + S$=15/2. This SOC-dominated regime leads to a set of well-defined J-multiplets, with the ${}^4I_{15/2}$[1] manifold forming the ground state and all higher-energy states split off into well-separated excited multiplets. In $ErCl_3$, all experimentally relevant physics occurs within this 16-fold degenerate J=15/2 multiplet, as thermal energy is insufficient to excite electrons to higher J-levels.

The localized nature of $4f$ electrons strongly influences the behavior of SOC in $ErCl_3$. Unlike $3d$ or $5d$ electrons, which are spatially extended and interact more directly with sur-

[1]The notation ${}^{2S+1}L_J$ specifies the quantum state, where $2S + 1$ is the spin multiplicity, L corresponds to the total orbital angular momentum, and J represents the total angular momentum quantum number. For Er^{3+}, S=3/2, L=6, and J=15/2.

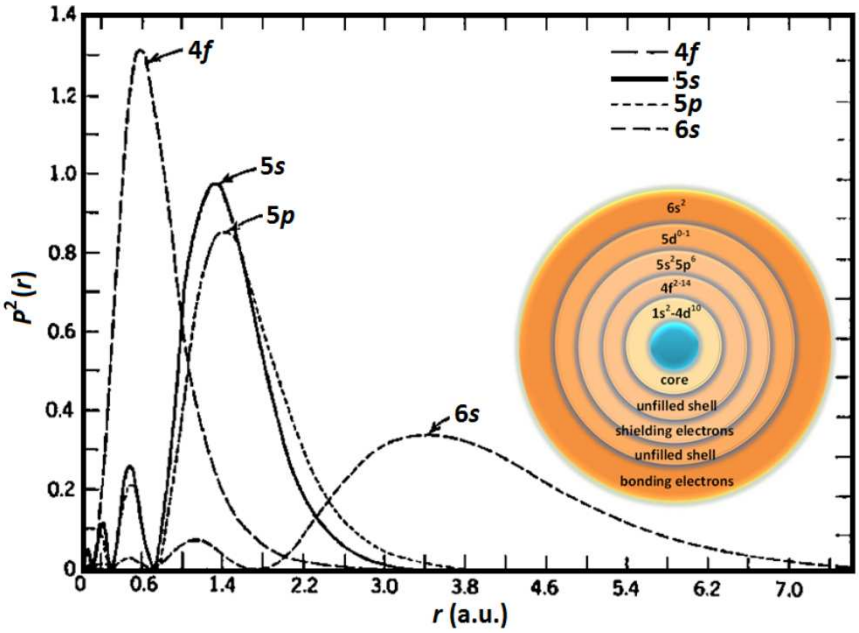

Figure 5.6: Square of the radial wavefunctions for the $4f$, $5s$, $5p$ and $6s$ energy levels from Hartree-Fock. It was a calculation for Gd^+ by Freeman e Watson (1962) [1, 2]. Picture inset schematically shows that the $4f$ orbital is within the $6s$, $5d$, $5p$, and $5s$ levels.

rounding ligands, $4f$ electrons are highly shielded by the outer $5s$ and $5p$ orbitals (Fig. 5.6). This shielding reduces direct ligand interactions, making SOC the dominant energy scale, while also ensuring that the $^4I_{15/2}$ manifold remains well-defined, even in the presence of moderate crystal field effects. As a result, the effective magnetic moment of Er^{3+} is largely determined by SOC and can be estimated using the Landé g-factor formula, yielding a theoretical value of $\mu_{\text{eff}} \approx 9.58\mu_B$.

However, this idealized picture does not account for the effect of the local crystal environment. In real materials, crystal electric fields (CEF) generated by the surrounding Cl^- ligands lift the $(2J+1)$ degeneracy, further splitting the J=15/2 manifold into a series of eight Kramers doublets. This CEF splitting pattern is highly dependent on the symmetry of the crystal field, with the monoclinic $C2/m$ structure of $ErCl_3$ imposing specific constraints on the energy-level separations. Experimentally, optical fluorescence studies have identified a 32 K gap between the ground-state doublet and first excited doublet, meaning that at temperatures below 32 K, $ErCl_3$ effectively behaves as a spin-1/2 system because only the

lowest doublet is thermally populated.

Although this effective spin-1/2 picture simplifies the low-temperature physics, the pseudospin-1/2 nature of the Er^{3+} moments is highly anisotropic, since their response to applied fields and interactions is constrained by the local CEF symmetry. Experimental evidence for this anisotropy comes from EPR studies on YCl_3 and $LuCl_3$, which report strongly direction-dependent g-values that reflect the underlying anisotropic wavefunctions of the ground-state doublet. Magnetization measurements on $ErCl_3$ also exhibit clear deviations from Curie-Weiss behavior, further indicating that CEF effects play a significant role in shaping its magnetic response.

This effective pseudospin-1/2 description is fundamental for understanding exchange interactions in $ErCl_3$, as it determines how the Er^{3+} moments couple within the honeycomb layers. Unlike a true isotropic spin-1/2, which follows conventional Heisenberg exchange, the pseudospin-1/2 moments in $ErCl_3$ transform under the local symmetries imposed by the crystal field, leading to anisotropic exchange interactions. This sets the stage for the next section, where we examine how these effective moments interact, and whether their coupling can be described within an extended Kitaev-Heisenberg framework.

5.3 Crystal Electric Field Effects

The crystal electric field (CEF) Hamiltonian in $ErCl_3$ governs the splitting of the spin-orbit coupled J=15/2 manifold into a series of Kramers doublets. The structure of these doublets determines the anisotropy of the magnetic moment, influences thermodynamic properties, and constrains the exchange interactions between Er^{3+} moments. A well-defined CEF model is essential for understanding the material's low-energy physics, yet experimentally resolving the full CEF level scheme remains challenging.

While the observed inelastic neutron scattering provides partial constraints, the limited number of observed transitions leaves ambiguities in determining the full CEF Hamiltonian.

Different sets of Stevens parameters B_l^m can reproduce the same observed neutron spectra while yielding significantly different predictions for thermodynamic properties such as magnetization and heat capacity. This degeneracy highlights a major limitation: the CEF levels inferred from neutron scattering alone do not uniquely determine the wavefunctions and thus cannot fully specify the material's low-temperature magnetic behavior. To refine the parameter space, we supplement neutron data with statistical mechanics and perturbation theory, using thermodynamic observables as additional constraints. Since magnetization and heat capacity depend on the thermal population of CEF levels, their temperature and field evolution provide a way to distinguish between competing CEF models. By incorporating these effects, we aim to build a more complete picture of the CEF-split states and their role in defining the effective spin degrees of freedom in $ErCl_3$.

To establish a theoretical model for the CEF levels, we begin by constructing the CEF Hamiltonian. Since the Er^{3+} ion in $ErCl_3$ resides at a site of C_2 point group symmetry, the crystal field potential can be expressed in terms of Stevens operators, allowing us to parameterize the level splittings and wavefunctions. Using Eq.2.12 and Table2.2, we define the CEF Hamiltonian $\mathcal{H}_{\text{CEF}}$ as follows

$$\begin{aligned}\mathcal{H}_{\text{CEF}} =& \sum_{l,m} B_l^m \hat{O}_l^m \\ =& B_2^0\hat{O}_2^0 + B_2^{-2}\hat{O}_2^{-2} + B_2^2\hat{O}_2^2 + B_4^0\hat{O}_4^0 + B_4^{-2}\hat{O}_4^{-2} + B_4^2\hat{O}_4^2 + B_4^{-4}\hat{O}_4^{-4} + B_4^4\hat{O}_4^4 \\ &+ B_6^0\hat{O}_6^0 + B_6^{-2}\hat{O}_6^{-2} + B_6^2\hat{O}_6^2 + B_6^{-4}\hat{O}_6^{-4} + B_6^4\hat{O}_6^4 + B_6^{-6}\hat{O}_6^{-6} + B_6^6\hat{O}_6^6\end{aligned} \tag{5.1}$$

where B_l^m are the Stevens parameters and $\hat{O}_l^m$ are the Stevens operators, discussed in Section 2.1.3. Solving for the eigenstates of this Hamiltonian analytically is cumbersome, so we use the PyCrystalField package [30], which numerically diagonalizes $\mathcal{H}_{\text{CEF}}$ and provides the energy eigenvalues and eigenvectors. The eigenstates are obtained numerically and can be expressed in two equivalent ways: in terms of the Stevens parameters B_l^m, or as a linear

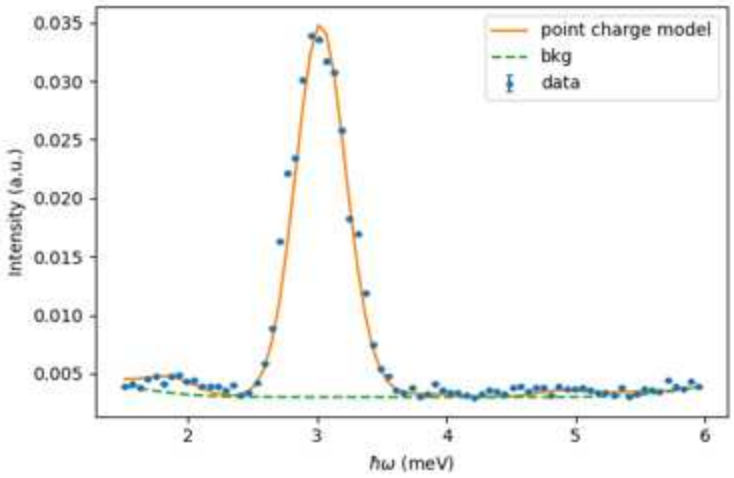

Figure 5.7: A point charge model fit to the experimental inelastic neutrons scattering data from the CAMEA experiment on $ErCl_3$.

combination of $|Jm_{Ji}\rangle$ basis states, with coefficients c_{ni}. The energy eigenstates can be written as

$$\mathcal{H}_{testCEF}\,|n\rangle = E_n\,|n\rangle \tag{5.2}$$

where $|n\rangle = \sum_i c_{ni}\,|Jm_{J_i}\rangle$. Since the crystal field Hamiltonian contains 15 free parameters B_l^m, its solution is not unique. However, it provides a useful starting point, which we can attempt to refine by constraining the allowed values of B_l^m using experimental data. The first such constraint comes from inelastic neutron scattering, where we observe low-lying CEF excitations in the powder-averaged neutron energy cut at T = 60 mK and H = 0 T, conditions where $ErCl_3$ is expected to be in its ground state. A fit to this data is shown in Fig. 5.7.

While the point charge model fit in Fig. 5.7 agrees well with the observed CEF excitations, it is important to recognize that fitting a few peaks using 15 free parameters is trivial and does not uniquely determine the Stevens coefficients. To further constrain $\{B_l^m\}$, we turn to additional thermodynamic observables: the temperature and field evolution of the neutron data and the magnetization deviation from Curie-Weiss behavior.

To determine how the CEF energy levels evolve with temperature, we use the Boltzmann distribution to obtain the thermal population of each eigenstate. The probability of occupying a state $|n\rangle$ is given by

$$P_n = \frac{1}{Z} e^{-\beta E_n} \tag{5.3}$$

where $\beta = \frac{1}{k_B T}$ and Z is the partition function

$$Z = \sum_n e^{-\beta E_n} \tag{5.4}$$

This framework allows us to compute thermal expectation values of the energy levels,

$$\langle E(T) \rangle = \sum_n P_n E_n \tag{5.5}$$

Again, this is computed using PyCrystalField, and the resulting finite-temperature population of the CEF states is shown in Fig. 5.8a. Having established the finite-temperature evolution of the CEF energy levels, we now turn to their response under an applied magnetic field.

For the expansion in applied magnetic field, we can perturb $\mathcal{H}_{\text{CEF}}$ with a Zeeman term $\mathcal{H}_Z$. PyCrystalField is not yet configured to accomodate such calculations, but the general form can be analytically written down as

$$\begin{aligned} \mathcal{H} &= \mathcal{H}_{\text{CEF}} + \mathcal{H}_Z \\ &= \sum_{l,m} B_l^m \hat{O}_l^m + \mu_0 \mu_B g_J \boldsymbol{H} \cdot \boldsymbol{J} \\ &= \sum_{l,m} B_l^m \hat{O}_l^m + \mu_0 \mu_B g_J H \hat{J}_z \quad , \quad \text{for } \boldsymbol{H} = H\hat{z}. \end{aligned} \tag{5.6}$$

where $\boldsymbol{H}$ is the applied magnetic field and $\boldsymbol{J}$ is the total angular momentum vector operator. We further specified the magnetic field as being applied along the $\hat{z}$-axis, corresponding to the experimental condition of the applied field along the crystallographic c-axis. If we let

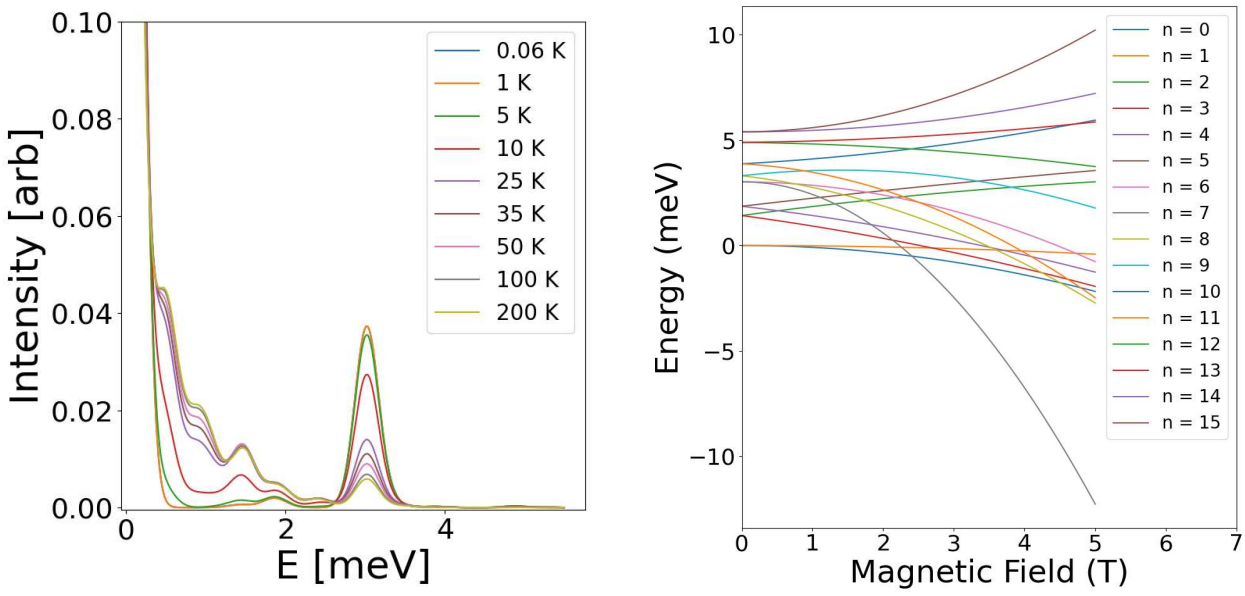

(a) (b)

Figure 5.8: Comparison of theoretical CEF energy level evolution under temperature and magnetic field variations. (a) Finite-temperature broadening of CEF energy levels, simulated using PyCrystalField, showing the redistribution of spectral weight with increasing temperature. (b) Zeeman splitting of CEF states under an applied magnetic field along the crystallographic c-axis, demonstrating the nonlinear evolution of energy levels as a function of field strength.

$A(H) = mu_0\mu_B g_J H$, then we can use standard perturbation theory to write the energy corrections (up to second order) due to the perturbation of the magnetic field as

$$\begin{aligned} E_n &= E_n^{(0)} + E_n^{(1)} + E_n^{(2)} \\ E_n &= E_n^{(0)} + \langle n^{(0)}| \mathcal{H}_Z |n^{(0)}\rangle + \sum_{m\neq n} \frac{|\langle n^{(0)}| \mathcal{H}_Z |m^{(0)}\rangle|^2}{E_n^{(0)} - E_m^{(0)}} \\ E_n &= E_n^{(0)} + A(H)\sum_i |c_{ni}^{(0)}|^2 m_{J_i} + |A(H)|^2 \sum_{m\neq n} \frac{\left|\sum_{i=1}^{2J+1} c_{ni}^{*(0)} m_{J_i} c_{mi}^{(0)}\right|^2}{E_n^{(0)} - E_m^{(0)}} \end{aligned} \tag{5.7}$$

where we have now written out the first two energy corrections in terms of $A(H) \sim H$ and the amplitude coefficients $c_{ni}^{(0)}$ of the $\mathcal{H}_{\text{CEF}}$ eigenstates—written in the basis of $|Jm_{J_i}\rangle$. The results of this perturbation are shown in Fig. 5.8b. This is valid in the weak field limit,

where $A(H) \ll E_n^{(0)}$. For strong fields, this must be done in the uncoupled $|LS\rangle$ basis. For intermediate fields, neither the weak- nor strong-field basis provides good quantum numbers, so the full Hamiltonian, including off-diagonal components of $\mathcal{H}_Z$, must be diagonalized. In practice, some approximations interpolate between the strong- and weak-field limits, but a rigorous treatment requires retaining all off-diagonal terms. For magnetization measurements at H=0.5 T, the weak-field limit provides a reasonable approximation. Thus given the set of Stevens parameters $\{B_l^m\}$, we can now expand how the energy levels will evolve as a function of temperature and applied magnetic field.

At this point, we have expanded the energy levels to depend on both temperature and applied field, $E_n(T, H)$. We can now use this result to analytically determine thermodynamic observables, such as magnetization and heat capacity. This is done by using thermodynamic relations. For magnetization, we have

$$M = -\frac{\partial F}{\partial H} \tag{5.8}$$

where the Helmholtz free energy F is given by

$$F = -k_B T \ln(Z) \tag{5.9}$$

thus

$$M(T, H) = \frac{1}{Z} \sum_n \left(-\frac{\partial E_n}{\partial H} \right) e^{-E_n/k_B T} \tag{5.10}$$

Similarly, with heat capacity C, we can write

$$\begin{aligned} C &= \frac{\partial \langle E \rangle}{\partial T} \\ \langle E \rangle &= \frac{1}{Z} \sum_n E_n e^{-E_n/k_B T} \\ C(T, H) &= \frac{1}{k_B T^2} \left(\langle E^2 \rangle - \langle E \rangle^2 \right) \end{aligned} \tag{5.11}$$

The field and temperature dependence of M(T,H) and C(T,H) naturally arises from the evolution of the CEF energy levels, E_n(T,H). Therefore, in principle, we can use the field and temperature evolution observed in inelastic neutron scattering and magnetization measurements to further constrain the allowed values of the Stevens parameters, $\{B_l^m\}$. Although these constraints significantly reduce the parameter space, degeneracies in fitting the spectral features persist. To resolve these ambiguities, additional experimental data would be highly beneficial. Specifically, inelastic neutron scattering over a broader and higher energy transfer range could provide access to additional CEF excitations, offering a more complete picture of the CEF level scheme. Additionally, field- and temperature-dependent heat capacity measurements would impose further constraints by directly probing the thermal population of these levels. The feasibility of these experimental approaches and their implications for refining the CEF model are discussed further in Section 6.2.

5.4 Exchange Interactions

The 120° antiferromagnetic structure observed in $ErCl_3$ presents a significant theoretical challenge, as its stabilization remains unexplained within conventional spin models. Neutron diffraction experiments have confirmed that below T_N=350 mK, the Er^{3+} moments form a noncollinear 120° order with a propagation vector of $\boldsymbol{k}$=(2/3,0,-1/12) [15]. However, this structure is incompatible with a purely Heisenberg description, which typically stabilizes collinear spin arrangements. This is in stark contrast to $YbCl_3$ a structurally similar rare-earth trichloride, which has been found to be an excellent realization of a 2D Heisenberg antiferromagnet with isotropic nearest-neighbor exchange [83, 82, 84]. The fact that $ErCl_3$ and $YbCl_3$ exhibit fundamentally different ground states—despite their structural similarities—suggests that the larger unquenched orbital angular momentum of Er^{3+} (J=15/2) compared to Yb^{3+} (J=7/2) plays a critical role in determining the nature of exchange interactions. Given the strong influence of spin-orbit coupling on anisotropy, what

exchange interactions beyond Heisenberg exchange could stabilize the 120° order in $ErCl_3$?

A purely Heisenberg description, where interactions are fully isotropic, cannot account for the 120° order. The conventional nearest-neighbor Heisenberg Hamiltonian

$$\mathcal{H} = J \sum_{\langle i,j \rangle} \boldsymbol{S}_i \cdot \boldsymbol{S}_j \tag{5.12}$$

favors collinear ground states such as Néel or stripe order. In contrast, the structure observed in $ErCl_3$ is noncollinear, indicating that additional anisotropic terms must be present. One possible way to introduce anisotropy within an otherwise Heisenberg-like model is to incorporate further-neighbor exchange interactions. Extending the Heisenberg hamiltonian to include second-nearest-neighbor (J_2) and third-nearest-neighbor (J_3) interactions can modify ground state selection by introducing additional frustration.

$$\mathcal{H} = J_1 \sum_{\langle i,j \rangle} \boldsymbol{S}_i \cdot \boldsymbol{S}_j + J_2 \sum_{\langle\langle i,j \rangle\rangle} \boldsymbol{S}_i \cdot \boldsymbol{S}_j + J_3 \sum_{\langle\langle\langle i,j \rangle\rangle\rangle} \boldsymbol{S}_i \cdot \boldsymbol{S}_j \tag{5.13}$$

In triangular and kagome lattices, frustration from these further-neighbor interactions can stabilize 120° order as the ground state [16]. However, on the honeycomb lattice, this mechanism does not lead to 120° order, as the connectivity of the lattice does not provide the same geometric frustration that enables such states in triangular-based systems. Instead, for honeycomb systems, the $J_1 - J_2 - J_3$ model tends to favor collinear states or spiral phases depending on parameter values [94, 95]. This is explicitly illustrated in the phase diagram for the $J_1 - J_2 - J_3$ model on the honeycomb lattice, shown in Fig. 5.9, where no region corresponding to 120° order appears.

The failure of the extended Heisenberg model to stabilize 120° order in $ErCl_3$ suggests that an alternative mechanism must be responsible. Given that this type of order has also been observed in materials such as $NaNi_2BiO_{6-\delta}$ and α-Li_2IrO_3—which are now being investigated as potential realizations of Kitaev physics [96, 97]— anisotropic, bond-dependent interactions emerge as the most likely explanation for $ErCl_3$'s unconventional ground state.

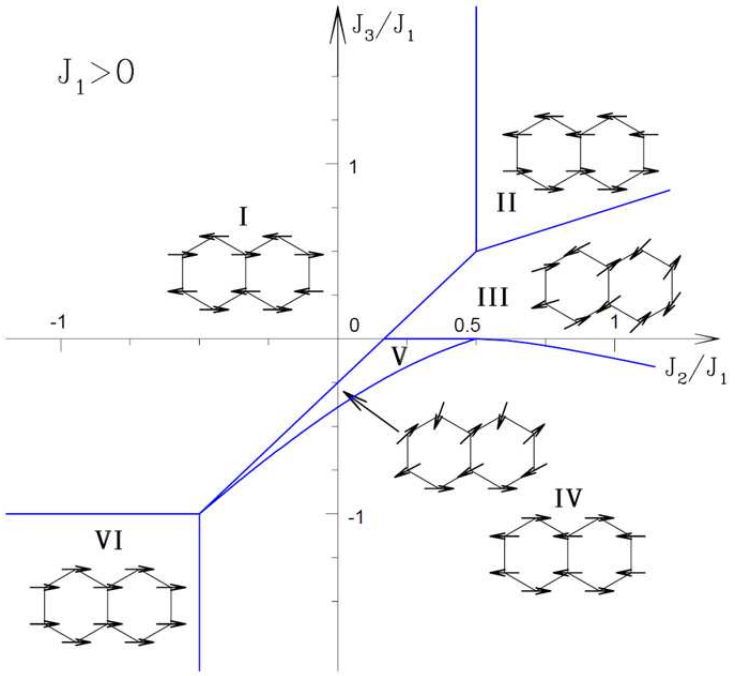

Figure 5.9: Phase diagram of the $J_1 - J_2 - J_3$ Heisenberg model on the honeycomb lattice, adapted from [16]. The absence of a 120° magnetic phase suggests that further-neighbor isotropic exchange alone cannot explain the experimentally observed order in $ErCl_3$.

A starting point for considering such interactions is the Kitaev model, originally introduced as an exactly solvable spin model on the honeycomb lattice. The defining feature of this model is its bond-dependent interactions, where the spin components coupled depend on the direction of the bond

$$\mathcal{H} = K \sum_{\langle i,j \rangle_\gamma} S_i^\gamma S_j^\gamma \tag{5.14}$$

Each bond ($\gamma = x, y, z$) enforces an Ising-like interaction along only one spin component, which suppresses conventional exchange pathways and leads to a highly entangled quantum spin liquid ground state. This model was discussed in broad strokes in Section 2.1.4, where its relevance to spin-orbit-coupled systems was outlined. However, while the Kitaev model provides a route to exotic magnetic phenomena, it does not support long-range magnetic order. If Kitaev interactions were dominant in $ErCl_3$, one would expect a disordered quantum spin liquid rather than the experimentally observed 120° structure.

A natural extension is the Heisenberg-Kitaev (HK) model, which incorporates both isotropic Heisenberg exchange and bond-dependent Kitaev interactions

$$\mathcal{H}_{testHK} = J \sum_{\langle i,j \rangle} \boldsymbol{S}_i \cdot \boldsymbol{S}_j + K \sum_{\langle i,j \rangle_\gamma} S_i^\gamma S_j^\gamma \tag{5.15}$$

This model has been extensively studied as a minimal framework for spin-orbit-coupled honeycomb magnets. The competition between Heisenberg and Kitaev terms produces a rich phase diagram, including stripe, zigzag, and Néel ordered phases, as well as spin liquid regimes, depending on the relative strength of J and K [98]. However, the 120° structure observed in $ErCl_3$ does not appear as a stable phase anywhere in the HK model's predicted phase diagram. This suggests that while bond-dependent interactions are likely important, the Kitaev term alone—even when combined with conventional Heisenberg exchange—does not explain the experimentally observed order.

Another possible explanation for the 120° order in $ErCl_3$ comes from the Heisenberg-Kitaev-Γ (K-Γ-H) model, which includes an additional symmetric off-diagonal exchange term

$$\mathcal{H} = \sum_{\langle ij \rangle \in \alpha\beta(\gamma)} [J \boldsymbol{S}_i \cdot \boldsymbol{S}_j + K S_i^\gamma S_j^\gamma + \Gamma \left(S_i^\alpha S_j^\beta + S_i^\beta S_j^\alpha \right)] \tag{5.16}$$

This model has been explored in the context of other honeycomb magnets, such as $NaNi_2BiO_{6-\delta}$ and α-Li_2IrO_3, where Kitaev and Γ interactions have been proposed as key drivers of noncollinear magnetic states [96, 97]. Similar to those systems, $ErCl_3$ features a strong spin-orbit-coupled moment on a honeycomb lattice, making it a natural candidate for anisotropic exchange interactions.

The Γ term represents an off-diagonal symmetric anisotropic exchange that couples different spin components on each bond. This interaction arises naturally in spin-orbit-coupled systems where the exchange paths involve significant orbital overlap between neighboring magnetic ions. In rare-earth systems like $ErCl_3$, the Γ term is particularly relevant because it can be understood as a truncated dipole-dipole interaction. Unlike conventional dipole-

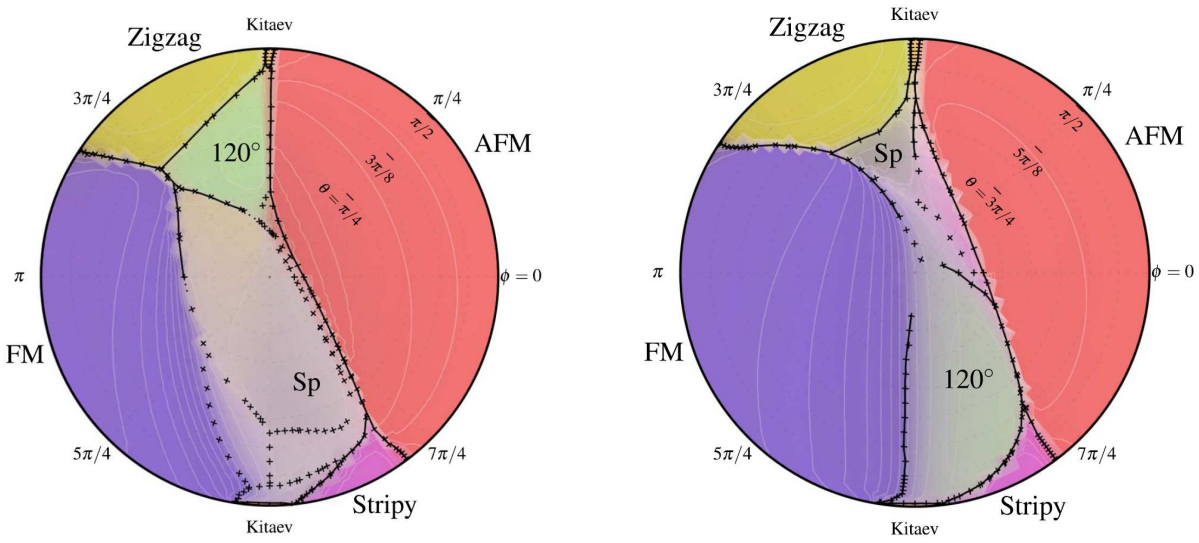

Figure 5.10: Phase diagram of the K-Γ-H model on the honeycomb lattice, adapted from [17]. The phase space of this model is visualized as a spherical projection, where the three exchange parameters—Kitaev (K), Heisenberg (J), and off-diagonal Γ—define points on the surface. The north and south poles correspond to purely Kitaev interactions with $K > 0$ and $K < 0$, respectively. The right and left hemispheres represent dominant Heisenberg exchange with $J > 0$ and $J < 0$, while the radial direction encodes the magnitude and sign of Γ, with the equatorial plane representing $\Gamma = 0$. Unlike the pure Heisenberg or Heisenberg-Kitaev models, this model includes regions where 120° order appears as a stable ground state, suggesting that additional anisotropic exchange interactions may play a role in $ErCl_3$.

dipole interactions, which decay as $1/r^3$, the Γ term effectively captures the short-range component of these interactions while respecting the symmetry constraints imposed by the crystal lattice. Since Er^{3+} has an unquenched orbital moment and strongly interacts with neighboring Er^{3+} ions via ligand-mediated superexchange, the presence of bond-dependent dipolar-like interactions is entirely reasonable.

Recent theoretical work has shown that the K-Γ-H model supports noncollinear magnetic phases, including 120° order, in certain regions of its phase diagram, as illustrated in Fig. 5.10 [17]. The competition between isotropic Heisenberg exchange, Kitaev bond-dependent interactions, and the additional frustration introduced by the Γ term provides a natural route to stabilizing the experimentally observed structure in $ErCl_3$.

While the K-Γ-H model presents a compelling framework for understanding the 120° order in $ErCl_3$, it belongs to a broader class of compass models, which have been developed to describe bond-dependent exchange interactions in strongly spin-orbit coupled systems. Many of these models, including the Kitaev and Γ interactions, have microscopic justifications based on spin-orbit coupling and crystal field effects, while others remain more phenomenological, constructed to stabilize specific magnetic orders [40]. As theoretical developments continue, more general compass-like interactions could provide alternative perspectives on $ErCl_3$'s exchange interactions, offering new directions for future modeling efforts.

5.5 Discussion

The results presented in this chapter highlight both the progress made in understanding $ErCl_3$ and the challenges that remain. The inelastic neutron scattering and thermodynamic measurements provide new insights into the crystal field environment and exchange interactions, yet they leave key questions unresolved. A primary focus was the effort to constrain the crystal field Hamiltonian, where we attempted to determine the Stevens parameters B_l^m from experimental data. Given the limited number of observed transitions in neutron scattering and the degeneracy of possible fits, a fully reliable determination remains out of reach. However, despite this inherent unconstrainability, the fits obtained using PyCrystalField were reasonably consistent with the available data. The temperature evolution of the energy level populations, estimated from the thermal expectation values, showed reasonable agreement with the inelastic neutron spectra at 40 K and 60 mK. Features such as the lower-energy shoulder structures and the persistence of peaks near 1.8 meV and 3 meV suggest that the inferred CEF scheme is at least a reasonable approximation. This agreement is illustrated in Fig. 5.11, where the computed thermal expectation values are compared directly with the experimental energy cuts, highlighting the extent to which the modeled level scheme captures the observed transitions. While these results suggest that the general energy scale

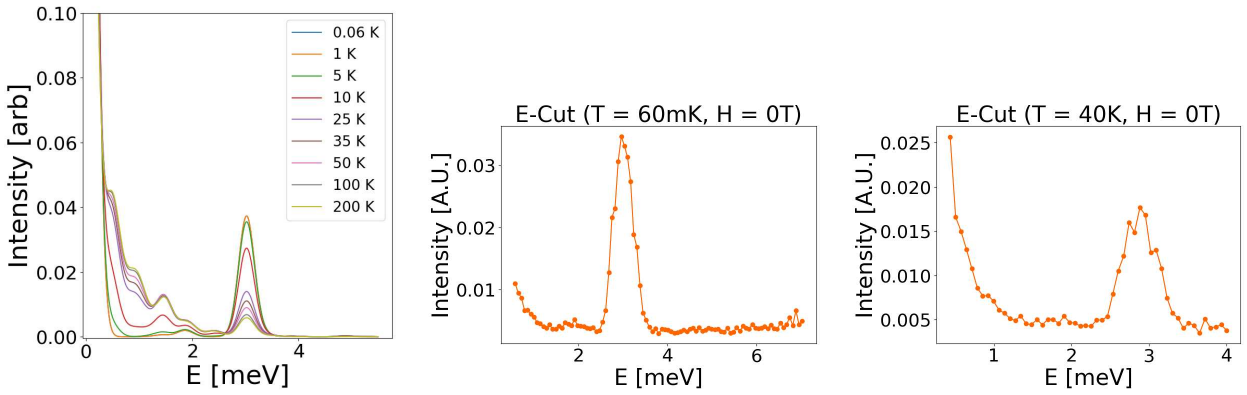

(a) (b) (c)

Figure 5.11: Comparison of the computed thermal population of crystal field levels (a) with experimental neutron energy cuts at 60 mK (b) and 40 K (c). The thermal evolution of the energy level populations, inferred from the computed expectation values, shows qualitative agreement with the experimental data in terms of spectral features and intensity trends, particularly in the persistence of peaks near 1.8 meV and 3 meV, as well as the emergence of lower-energy (E <1 meV) shoulder features at higher temperatures. The intensity scales are normalized independently to highlight spectral trends and facilitate direct comparison of relative peak positions and widths.

of the CEF excitations is well represented, the ambiguities in determining the full set of B_l^m parameters remain, reinforcing the necessity of additional experimental constraints.

While these results provide a meaningful starting point, the lack of higher-energy neutron data limits the refinement of the CEF Hamiltonian. The strongest test of the model would come from measuring additional CEF transitions at higher energy transfer, which would further constrain the parameter space. Similarly, field-dependent neutron scattering would offer a direct probe of how the wavefunctions evolve under external perturbations, allowing for a more stringent verification of the model. Without these additional constraints, any parameter set obtained remains one of many possible solutions. Nevertheless, the qualitative agreement between the thermal expansion of energy levels and the neutron data suggests that the overall structure of the CEF levels is at least partially captured.

The exchange interactions responsible for stabilizing the 120° order remain equally difficult to determine. The absence of resolvable spin wave dispersions in neutron spectroscopy prevents a direct extraction of interaction parameters, leaving us reliant on indirect con-

straints. By ruling out the Heisenberg and extended Heisenberg models, as well as the pure Kitaev and Heisenberg-Kitaev models, we argue that anisotropic, bond-dependent interactions are the most viable explanation for the magnetic order observed in $ErCl_3$. The Heisenberg-Kitaev-Γ (K-Γ-H) model, which includes an additional symmetric off-diagonal Γ term, is the only well-established theoretical framework known to stabilize 120° order on the honeycomb lattice within currently studied interactions. Given the strong spin-orbit coupling of Er^{3+} and the unquenched orbital moment, the presence of such bond-dependent interactions is entirely reasonable, particularly if the Γ term is interpreted as the short-range component of dipole-dipole interactions.

This interpretation aligns with other candidate Kitaev materials such as $NaNi_2BiO_{6-\delta}$ and α-Li_2IrO_3, where noncollinear magnetic order has been attributed to Kitaev and Γ interactions. The similarities in their magnetic structures suggest a broader relevance of bond-dependent anisotropic interactions in spin-orbit-coupled honeycomb magnets. However, the precise form of the exchange Hamiltonian in $ErCl_3$ remains an open question. The K-Γ-H model provides a plausible mechanism, but further theoretical and experimental work is needed to determine whether additional interactions contribute to stabilizing the observed order.

Ultimately, the results of this study emphasize both the promise and the limitations of current experimental techniques. While our data provide compelling evidence for significant anisotropic exchange, they remain insufficient to fully resolve the microscopic Hamiltonian. The most direct and unambiguous way to extract the exchange parameters is a neutron scattering measurement in the field-polarized phase. Such an experiment would resolve the spin wave dispersions, allowing a rigorous quantitative determination of interaction strengths via linear spin wave theory (LSWT). Without this measurement, the exchange interactions cannot be reliably extracted, leaving their precise form speculative. A successful measurement would require ensuring proper sample alignment—avoiding the misorientation issues that plagued the previous experiment—and, perhaps just as critically, avoiding interference from

Swiss customs officers. With the field-polarized dispersions properly resolved, the exchange interactions could finally be quantitatively determined using linear spin wave theory (LSWT), achieving the primary goal of this study. Beyond this, extending neutron spectroscopy to higher energy transfers, performing in-field neutron scattering to probe wavefunction evolution, and conducting additional thermodynamic measurements—particularly field- and temperature-dependent heat capacity—would further constrain the CEF scheme and refine the understanding of anisotropic interactions. These efforts would significantly advance our knowledge of $ErCl_3$ and its potential role as a platform for bond-dependent anisotropic magnetism. Determining whether $ErCl_3$ truly realizes the K-Γ-H model, or whether additional interactions are at play, will be crucial in understanding the broader role of bond-dependent anisotropic exchange in rare-earth honeycomb magnets.

Chapter 6

Conclusion

6.1 Summary

The study of rare-earth honeycomb magnets has provided new insights into the fundamental interactions that govern their quantum magnetic behavior. Through a combination of neutron scattering, magnetization, and thermodynamic measurements, this dissertation has explored the role of spin-orbit coupling, crystal field effects, and exchange anisotropy in shaping the ground states of these materials. A particular focus has been placed on understanding the nature of bond-dependent exchange interactions and their potential to stabilize exotic quantum phases, such as quantum spin liquids. The findings presented here contribute to the broader effort of identifying and characterizing materials with highly anisotropic interactions, bringing us closer to realizing experimental platforms for novel quantum states of matter.

The investigation of $Yb_2Si_2O_7$ has revealed its behavior as a quantum dimer magnet with a field-induced phase transition, exhibiting characteristics of triplon condensation. Magnetization measurements confirm a highly anisotropic response, with distinct saturation behaviors along different crystallographic directions. Neutron scattering experiments provide strong evidence for the presence of a field-induced phase transition, in agreement with theoretical expectations. However, a key finding is the absence of clear staggered magnetic order within the predicted Bose-Einstein condensate phase, contrary to the expectations of a simple two-sublattice model. This discrepancy suggests that additional factors, such as quantum fluctuations or an alternative order parameter, may be influencing the magnetic

structure of $Yb_2Si_2O_7$. Further refinements in theoretical modeling are required to fully understand the interplay between exchange interactions and anisotropic perturbations in this material.

The study of $ErCl_3$ has led to several major advancements. First, we optimized the synthesis of $ErCl_3$ single crystals, refining growth conditions to produce high-purity samples suitable for neutron scattering and thermodynamic measurements. Given the extreme air sensitivity of $ErCl_3$, we also developed robust air-free methodologies for sample handling and preparation, ensuring that measurements were conducted on pristine, unreacted crystals. These techniques represent a significant methodological advancement that can be broadly applied to other air-sensitive materials, extending beyond rare-earth halides to a wide range of quantum materials where environmental degradation poses a challenge. Our magnetization measurements revealed clear magnetic anisotropy, demonstrating that $ErCl_3$ deviates from an isotropic Heisenberg model and exhibits strong exchange anisotropy. By combining these measurements with neutron scattering, we were able to place significant constraints on the crystal field parameters governing the system. Typically, determining crystal field parameters from experimental data alone presents a challenge due to the degeneracy of possible fits. However, by leveraging theoretical treatments alongside inelastic neutron scattering, we systematically refined the parameter space, showing how the interplay between spin-orbit coupling and exchange interactions shapes the low-energy magnetic excitations. This approach provides a more precise and experimentally grounded framework for modeling $ErCl_3$'s magnetic behavior, reducing ambiguity in parameter selection and further refining our understanding of the system's Hamiltonian. Importantly, by comparing experimental data with theoretical models, we established that the only viable explanations for $ErCl_3$'s magnetism involve the presence of Kitaev interactions. This finding positions $ErCl_3$ as one of the few known rare-earth materials where Kitaev-like physics is directly relevant, making it an important platform for future investigations into bond-dependent anisotropic exchange and its role in stabilizing exotic magnetic phases. The combination of experimental

constraints and theoretical modeling developed in this work highlights how a multi-faceted approach can be used to systematically refine key parameters, providing a template for future studies of strongly spin-orbit-coupled materials.

While this dissertation has significantly advanced the understanding of rare-earth quantum magnets, it also highlights the complexity of these materials and the challenges inherent in fully characterizing their interactions. The interplay between exchange anisotropy, spin-orbit coupling, and geometric frustration continues to offer rich avenues for exploration, both experimentally and theoretically. The discoveries presented here provide a strong foundation for future research, demonstrating that rare-earth honeycomb magnets are a promising platform for investigating novel magnetic states and deepening our understanding of strongly correlated quantum systems.

6.2 Future Work

Further investigations into $Yb_2Si_2O_7$ are also necessary to refine our understanding of its quantum magnetism. One critical avenue of research involves high-resolution neutron scattering studies under applied magnetic fields to better characterize the field-induced phase transition and the nature of the triplon condensate. The absence of clear staggered magnetic order in the predicted Bose-Einstein condensate phase suggests that additional interactions or quantum fluctuations may be influencing the condensate state. By performing neutron scattering with improved resolution and higher applied fields, it may be possible to determine whether hidden order or unaccounted anisotropic interactions are at play.

Another important direction is to explore the potential role of spin-lattice coupling in $Yb_2Si_2O_7$. If lattice distortions or phonon interactions contribute to the observed deviations from theoretical expectations, complementary experiments such as Raman spectroscopy or thermal expansion measurements could provide key insights. These studies would help clarify whether structural effects are influencing the exchange interactions or the stability of the

field-induced phase.

Theoretical refinements are also needed to fully describe the exchange interactions governing $Yb_2Si_2O_7$. The deviations from expected magnetic order suggest that current models may be oversimplified. A more detailed theoretical treatment that incorporates longer-range exchange interactions, anisotropic perturbations, or additional frustration mechanisms could help bridge the gap between experiment and theory. Further computational modeling and comparison with experimental data will be crucial in constructing a more complete description of the system's Hamiltonian.

Finally, external tuning parameters such as chemical substitution or pressure could provide new insights into the quantum phase diagram of $Yb_2Si_2O_7$. Given its proximity to a quantum critical point, modifying the lattice geometry through chemical substitution (e.g., replacing Si with Ge) or applying pressure could push the system into different magnetic or nonmagnetic phases. Such studies could help determine whether frustration or competing interactions are responsible for the observed anomalies and whether similar systems might host more exotic quantum phases. By pursuing these experimental and theoretical directions, future work on $Yb_2Si_2O_7$ could provide a deeper understanding of quantum dimer magnets and their potential for realizing unconventional quantum states.

One of the most impactful next steps for $ErCl_3$ would be a successful field-polarized inelastic neutron scattering experiment with properly aligned crystals. This would allow for a direct quantification of Kitaev interactions by measuring spin wave dispersions in the high-field polarized state. The previous attempt was hindered by practical challenges, but a new experiment with improved crystal alignment and logistics would provide definitive evidence for the extent of bond-dependent interactions. Given that $ErCl_3$ has already shown signs of Kitaev interactions, this experiment could establish its place in the broader landscape of quantum magnetism.

Additional thermodynamic and spectroscopic experiments would help solidify the understanding of $ErCl_3$'s exchange interactions. Temperature- and field-dependent heat capacity

measurements could reveal more about the system's low-energy excitations and potential entropic signatures of fractionalization. Extending inelastic neutron scattering measurements to broader energy ranges would provide a more complete determination of the crystal field parameters, ensuring that higher-energy excitations are accounted for in theoretical models. Raman spectroscopy would serve as an ideal complementary technique, probing additional aspects of the spin and phonon dynamics that may be inaccessible via neutron-based methods.

Beyond $ErCl_3$, the rare-earth trihalide family presents a promising avenue for discovering new quantum magnetic states. $ErBr_3$ and ErI_3, in particular, offer intriguing possibilities due to the enhanced spin-orbit coupling and larger ligand ionic radii, which could further amplify bond-dependent exchange anisotropies. Investigating these materials with the same rigorous experimental approach could reveal whether they exhibit stronger Kitaev interactions or even more exotic quantum magnetic behavior. Understanding how the halide chemistry influences exchange interactions will be crucial for identifying materials that push the boundaries of bond-dependent magnetism.

Once the exchange parameters of $ErCl_3$ are quantitatively established, it will be possible to place it precisely on the Kitaev-Γ-Heisenberg phase diagram. This will provide a framework for understanding its relationship to theoretically predicted phases and guide strategies for tuning it toward a more quantum spin liquid-like state. External perturbations such as chemical substitution, applied pressure, or controlled disorder could be explored as potential routes to suppress magnetic order and stabilize a proximate Kitaev quantum spin liquid. Identifying such tuning mechanisms could open the door to new experimental realizations of highly entangled quantum matter.

Bibliography

[1] A. J. Freeman and R. E. Watson. Theoretical Investigation of Some Magnetic and Spectroscopic Properties of Rare-Earth Ions. *Physical Review*, 127(6):2058, 1962.

[2] V. A. G. Rivera, F. A. Ferri, and E. Marega Jr. Localized Surface Plasmon Resonances: Noble Metal Nanoparticle Interaction with Rare-Earth Ions. *Plasmonics - Principles and Applications*, 1(11):283–312, 2012.

[3] G. L. Hester. *Quantum Magnetism in the Rare-Earth Pyrosilicates*. PhD thesis, Colorado State University, 2021.

[4] S. Rufo, J. R. de Sousa, and J. A. Plascak. Exchange Frustration Effect due to Anisotropies on the Spin-1/2 J_1 - J_1' - J_2 Model. *Physica A: Statistical Mechanics and its Applications*, 518:349–362, 2019.

[5] C. Kittel. *Introduction to Solid State Physics*. Wiley, eighth edition, 2021.

[6] *Magnetic Property Measurement System - MPMS 3 User's Manual*. Quantum Design, San Diego, CA, 15th ed. edition, 2016.

[7] *iQuantum MPMS3 Hardware Guide*. Quantum Design Japan, Tokyo, Japan, rev 1.1.06 edition, 2020. Model # IQM02-001-00.

[8] *Quantum Design PPMS Dilution Refrigerator User's Manual*. Quantum Design, San Diego, CA, rev a6 edition, 2018. Part Number 1091-100.

[9] D. R. Yahne. *Exotic Phenomena in Rare-Earth Based Geometrically Frustrated Magnets*. PhD thesis, Colorado State University, 2022.

[10] D. L. Price and F. Fernandez-Alonso. An Introduction to Neutron Scattering. In *Experimental Methods in the Physical Sciences*, volume 44, pages 1–136. Elsevier, 2013.

[11] G. Hester, H. S. Nair, T. Reeder, D. R. Yahne, T. N. DeLazzer, L. Berges, D. Ziat, J. R. Neilson, A. A. Aczel, G. Sala, J. A. Quilliam, and K. A. Ross. Novel Strongly Spin-Orbit Coupled Quantum Dimer Magnet: $Yb_2Si_2O_7$. *Physical Review Letters*, 123(2):027201, 2019.

[12] M. O. Flynn, T. E. Baker, S. Jindal, and R. R. P. Singh. Two Phases Inside the Bose Condensation Dome of $Yb_2Si_2O_7$. *Physical Review Letters*, 126(6):067201, 2021.

[13] G. Garton, M. T. Hutchings, R. Shore, and W. P. Wolf. Paramagnetic Resonance of Rare-Earth Ions in YCl_3 and $LuCl_3$. *The Journal of Chemical Physics*, 41(7):1970–1974, 1964.

[14] J. W. Rakestraw and G. H. Dieke. Spectra and Energy Levels of Er^{3+} in YCl_3. *The Journal of Chemical Physics*, 42(3):873–878, 1965.

[15] K. W. Krämer, H. U. Güdel, P. Fischer, F. Fauth, M. T. Fernandez-Diaz, and T. Hauß. Triangular Antiferromagnetic Order in the Honeycomb Layer Lattice of. *The European Physical Journal B - Condensed Matter and Complex Systems*, 18(1):39–47, 2000.

[16] J. B. Fouet, P. Sindzingre, and C. Lhuillier. An Investigation of the Quantum J_1-J_2-J_3 Model on the Honeycomb Lattice. *The European Physical Journal B - Condensed Matter and Complex Systems*, 20:241–254, 2001.

[17] J. G. Rau, E. K.-H. Lee, and H.-Y. Kee. Generic Spin Model for the Honeycomb Iridates Beyond the Kitaev Limit. *Physical Review Letters*, 112(7):077204, 2014.

[18] J. H. Van Vleck. *The Theory of Electric and Magnetic Susceptibilities*. Oxford University Press, 1932.

[19] D. R. Yahne, B. Placke, R. Schäfer, O. Benton, R. Moessner, M. Powell, J. W. Kolis, C. M. Pasco, A. F. May, M. D. Frontzek, and K. A. Ross. Dipolar Spin Ice Regime

Proximate to an All-in-All-out Néel Ground State in the Dipolar-Octupolar Pyrochlore $Ce_2Sn_2O_7$. *Physical Review X*, 14(1):011005, 2024.

[20] D. J. Griffiths and D. F. Schroeter. *Introduction to Quantum Mechanics*. Cambridge University Press, 2019.

[21] C. Cohen-Tannoudji, B. Diu, and F. Laloë. *Quantum Mechanics, Volume 1*, volume 1. Wiley-VCH, 1986.

[22] J. B. Goodenough. *Magnetism and the Chemical Bond*. Interscience Publishers, New York, 1963.

[23] J. Kanamori. Superexchange Interaction and Symmetry Properties of Electron Orbitals. *Journal of Physics and Chemistry of Solids*, 10(2-3):87–98, 1959.

[24] L. Balents. Spin Liquids in Frustrated Magnets. *Nature*, 464(7286):199–208, 2010.

[25] A. Abragam and B. Bleaney. *Electron Paramagnetic Resonance of Transition Ions*. OUP Oxford, 2012.

[26] J. Jensen and A. R. Mackintosh. *Rare Earth Magnetism: Structures and Excitations*. Oxford University Press, 1991.

[27] K. W. H. Stevens. Matrix Elements and Operator Equivalents Connected with the Magnetic Properties of Rare Earth Ions. *Proceedings of the Physical Society. Section A*, 65(3):209, 1952.

[28] M. T. Hutchings. Point-Charge Calculations of Energy Levels of Magnetic Ions in Crystalline Electric Fields. In *Solid State Physics*, volume 16, pages 227–273. Elsevier, 1964.

[29] J. J. Sakurai and J. Napolitano. *Modern Quantum Mechanics*. Cambridge University Press, 2020.

[30] A. Scheie. PyCrystalField: Software for Calculation, Analysis and Fitting of Crystal Electric Field Hamiltonians. *Journal of Applied Crystallography*, 54(1):356–362, 2021.

[31] E. Bauer and M. Rotter. Magnetism of Complex Metallic Alloys: Crystalline Electric Field Effects. In *Properties and Applications of Complex Intermetallics*, pages 183–248. World Scientific, 2010.

[32] U. Walter. Crystal-Field Splitting in Icosahedral Symmetry. *Physical Review B*, 36(5):2504, 1987.

[33] K. R. Lea, M. J. M. Leask, and W. P. Wolf. The Raising of Angular Momentum Degeneracy of f-Electron Terms by Cubic Crystal Fields. *Journal of Physics and Chemistry of Solids*, 23(10):1381–1405, 1962.

[34] Z. Dun, X. Bai, M. B. Stone, H. Zhou, and M. Mourigal. Effective Point-Charge Analysis of Crystal Fields: Application to Rare-Earth Pyrochlores and Tripod Kagome Magnets $R_3Mg_2Sb_3O_{14}$. *Physical Review Research*, 3(2):023012, 2021.

[35] G. Jackeli and G. Khaliullin. Mott Insulators in the Strong Spin-Orbit Coupling Limit: From Heisenberg to a Quantum Compass and Kitaev Models. *Physical Review Letters*, 102(1):017205, 2009.

[36] L. Savary and L. Balents. Quantum Spin Liquids: A Review. *Reports on Progress in Physics*, 80(1):016502, 2016.

[37] I. Dzyaloshinsky. A Thermodynamic Theory of "Weak" Ferromagnetism of Antiferromagnetics. *Journal of Physics and Chemistry of Solids*, 4(4):241–255, 1958.

[38] T. Moriya. Anisotropic Superexchange Interaction and Weak Ferromagnetism. *Physical Review*, 120(1):91, 1960.

[39] T. Yildirim, A. B. Harris, A. Aharony, and O. Entin-Wohlman. Anisotropic Spin Hamiltonians due to Spin-Orbit and Coulomb Exchange Interactions. *Physical Review B*, 52(14):10239, 1995.

[40] Z. Nussinov and J. van den Brink. Compass Models: Theory and Physical Motivations. *Reviews of Modern Physics*, 87(1):1–59, 2015.

[41] S. M. Winter, A. A. Tsirlin, M. Daghofer, J. van den Brink, Y. Singh, P. Gegenwart, and R. Valentí. Models and Materials for Generalized Kitaev Magnetism. *Journal of Physics: Condensed Matter*, 29(49):493002, 2017.

[42] T. Lancaster and S. J. Blundell. *Quantum Field Theory for the Gifted Amateur*. OUP Oxford, 2014.

[43] P. W. Anderson. Resonating Valence Bonds: A New Kind of Insulator? *Materials Research Bulletin*, 8(2):153–160, 1973.

[44] P. W. Anderson. The Resonating Valence Bond State in La_2CuO_4 and Superconductivity. *Science*, 235(4793):1196–1198, 1987.

[45] J. Knolle and R. Moessner. A Field Guide to Spin Liquids. *Annual Review of Condensed Matter Physics*, 10(1):451–472, 2019.

[46] A. Banerjee, C. A. Bridges, J.-Q. Yan, A. A. Aczel, L. Li, M. B. Stone, G. E. Granroth, M. D. Lumsden, Y. Yiu, J. Knolle, D. L. Kovrizhin, S. Bhattacharjee, R. Moessner, D. A. Tennant, D. G. Mandrus, and S. E. Nagler. Proximate Kitaev Quantum Spin Liquid Behaviour in a Honeycomb Magnet. *Nature Materials*, 15(7):733–740, 2016.

[47] A. Banerjee, J. Yan, J. Knolle, C. A. Bridges, M. B. Stone, M. D. Lumsden, D. G. Mandrus, D. A. Tennant, R. Moessner, and S. E. Nagler. Neutron Scattering in the Proximate Quantum Spin Liquid α-$RuCl_3$. *Science*, 356(6342):1055–1059, 2017.

[48] J. Knolle, D. L. Kovrizhin, J. T. Chalker, and R. Moessner. Dynamics of a Two-Dimensional Quantum Spin Liquid: Signatures of Emergent Majorana Fermions and Fluxes. *Physical Review Letters*, 112(20):207203, 2014.

[49] Y. Kubota, H. Tanaka, T. Ono, Y. Narumi, and K. Kindo. Successive Magnetic Phase Transitions in α-$RuCl_3$: XY-like Frustrated Magnet on the Honeycomb Lattice. *Physical Review B*, 91(9):094422, 2015.

[50] S.-H. Baek, S.-H. Do, K.-Y. Choi, Y. S. Kwon, A. U. B. Wolter, S. Nishimoto, J. van den Brink, and B. Büchner. Evidence for a Field-Induced Quantum Spin Liquid in α-$RuCl_3$. *Physical Review Letters*, 119(3):037201, 2017.

[51] R. D. Johnson, S. C. Williams, A. A. Haghighirad, J. Singleton, V. Zapf, P. Manuel, I. I. Mazin, Y. Li, H. O. Jeschke, and R. Valentí. Monoclinic Crystal Structure of α-$RuCl_3$ and the Zigzag Antiferromagnetic Ground State. *Physical Review B*, 92(23):235119, 2015.

[52] L. J. Sandilands, Y. Tian, K. W. Plumb, Y.-J. Kim, and K. S. Burch. Scattering Continuum and Possible Fractionalized Excitations in α-$RuCl_3$. *Physical Review Letters*, 114(14):147201, 2015.

[53] Y. Kasahara, T. Ohnishi, Y. Mizukami, O. Tanaka, S. Ma, K. Sugii, N. Kurita, H. Tanaka, J. Nasu, Y. Motome, T. Shibauchi, and Y. Matsuda. Majorana Quantization and Half-Integer Thermal Quantum Hall Effect in a Kitaev Spin Liquid. *Nature*, 559(7713):227–231, 2018.

[54] I. A. Leahy, C. A. Pocs, P. E. Siegfried, D. Graf, S.-H. Do, K.-Y. Choi, B. Normand, and M. Lee. Anomalous Thermal Conductivity and Magnetic Torque Response in the Honeycomb Magnet α-$RuCl_3$. *Physical Review Letters*, 118(18):187203, 2017.

[55] C. A. Pocs, J. Xing, E. S. Choi, A. S. Sefat, M. Hermele, and M. Lee. Generic Magnetic Field Dependence of Thermal Conductivity in Effective Spin-1/2 Magnetic Insula-

tors via Hybridization of Acoustic Phonons and Spin-Flip Excitations. *arXiv preprint*, arXiv:2401.01407, 2024.

[56] M. Ciomaga Hatnean, O. A. Petrenko, M. R. Lees, T. E. Orton, and G. Balakrishnan. Optical Floating Zone Crystal Growth of Rare-Earth Disilicates, $R_2Si_2O_7$ (R=Er, Ho, and Tm). *Crystal Growth & Design*, 20(10):6636–6648, 2020.

[57] M. Binnewies, R. Glaum, M. Schmidt, and P. Schmidt. *Chemical Vapor Transport Reactions*. Walter de Gruyter, 2012.

[58] A. R. West. *Solid State Chemistry and Its Applications*. John Wiley & Sons, 2022.

[59] *CLIP User Manual*. Olaf J. Schumann, 2009. Software Manual.

[60] N. W. Ashcroft and N. D. Mermin. *Solid State Physics*. Saunders College Publishing, 1976.

[61] D. V. Schroeder. *An Introduction to Thermal Physics*. Oxford University Press, 2020.

[62] F. Reif. *Fundamentals of Statistical and Thermal Physics*. Waveland Press, 2009.

[63] H. B. Callen. *Thermodynamics and an Introduction to Thermostatistics*. John Wiley & Sons, 1991.

[64] R. K. Pathria and P. D. Beale. *Statistical Mechanics*. Elsevier, 3rd edition, 2011.

[65] R. J. Thorn. On the Origin of the λ-type Transition in Heat Capacity. *The Journal of Chemical Thermodynamics*, 34(7):973–985, 2002.

[66] J. Cardy. *Scaling and Renormalization in Statistical Physics*, volume 5. Cambridge University Press, 1996.

[67] D. J. Amit and V. Martín-Mayor. *Field Theory, the Renormalization Group, and Critical Phenomena: Graphs to Computers*. World Scientific Publishing Company, 2005.

[68] S. Sachdev. *Quantum Phase Transitions*. Cambridge University Press, 2011.

[69] J. Zinn-Justin. *Quantum Field Theory and Critical Phenomena*, volume 171. Oxford University Press, 2021.

[70] H. E. Stanley. *Phase Transitions and Critical Phenomena*, volume 7. Clarendon Press, Oxford, 1971.

[71] *Physical Property Measurement System: Heat Capacity Option User's Manual*. Quantum Design, San Diego, CA, rev m7 edition, 2017. Model # 1085-150.

[72] S. W. Lovesey. *Theory of Neutron Scattering from Condensed Matter*. Clarendon Press, Oxford, 1984.

[73] G. L. Squires. *Introduction to the Theory of Thermal Neutron Scattering*. Courier Corporation, 1996.

[74] A. T. Boothroyd. *Principles of Neutron Scattering from Condensed Matter*. Oxford University Press, 2020.

[75] W. H. Zurek. Decoherence, Einselection, and the Quantum Origins of the Classical. *Reviews of Modern Physics*, 75(3):715, 2003.

[76] V. Zapf, M. Jaime, and C. D. Batista. Bose-Einstein Condensation in Quantum Magnets. *Reviews of Modern Physics*, 86(2):563, 2014.

[77] A. Kitaev. Anyons in an Exactly Solved Model and Beyond. *Annals of Physics*, 321(1):2–111, 2006.

[78] H. Takagi, T. Takayama, G. Jackeli, G. Khaliullin, and S. E. Nagler. Concept and Realization of Kitaev Quantum Spin Liquids. *Nature Reviews Physics*, 1(4):264–280, 2019.

[79] J. G. Rau and M. J. P. Gingras. Frustration and Anisotropic Exchange in Ytterbium Magnets with Edge-Shared Octahedra. *Physical Review B*, 98(5):054408, 2018.

[80] Z.-X. Luo and G. Chen. Honeycomb Rare-Earth Magnets with Anisotropic Exchange Interactions. *SciPost Physics Core*, 3(1):004, 2020.

[81] Q. Luo, J. Zhao, and X. Wang. Interplay of Kitaev Interaction and Off-diagonal Exchanges: Exotic Phases and Quantum Phase Diagrams. *Chinese Physics Letters*, 2024.

[82] J. Xing, E. Feng, Y. Liu, E. Emmanouilidou, C. Hu, J. Liu, D. Graf, A. P. Ramirez, G. Chen, H. Cao, and N. Ni. Néel-type Antiferromagnetic Order and Magnetic Field–Temperature Phase Diagram in the Spin-1/2 Rare-Earth Honeycomb Compound $YbCl_3$. *Physical Review B*, 102(1):014427, 2020.

[83] G. Sala, M. B. Stone, B. K. Rai, A. F. May, D. S. Parker, G. B. Halász, Y. Q. Cheng, G. Ehlers, V. O. Garlea, Q. Zhang, and D. Mandrus. Crystal Field Splitting, Local Anisotropy, and Low-Energy Excitations in the Quantum Magnet $YbCl_3$. *Physical Review B*, 100(18):180406, 2019.

[84] G. Sala, M. B. Stone, B. K. Rai, A. F. May, P. Laurell, V. O. Garlea, N. P. Butch, M. D. Lumsden, G. Ehlers, G. Pokharel, R. S. Fishman, and D. Mandrus. Van Hove Singularity in the Magnon Spectrum of the Antiferromagnetic Quantum Honeycomb Lattice. *Nature Communications*, 12(1):171, 2021.

[85] K. W. Krämer, H. U. Güdel, B. Roessli, P. Fischer, A. Dönni, N. Wada, F. Fauth, M. T. Fernandez-Diaz, and T. Hauß. Noncollinear Two- and Three-Dimensional Magnetic Ordering in the Honeycomb Lattices of ErX_3 (X=Cl, Br, I). *Physical Review B*, 60(6):R3724, 1999.

[86] K. W. Krämer, H. U. Güdel, B. Roessli, P. Fischer, A. Dönni, N. Wada, F. Fauth, M. T. Fernandez-Diaz, and T. Hauß. Magnetic Ordering in the Erbium Honeycomb Lattices of ErX_3 (X=Cl, Br, I). *Physica B: Condensed Matter*, 276:674–675, 2000.

[87] D. R. Lide. *CRC Handbook of Chemistry and Physics*, volume 85. CRC Press, 2004.

[88] I. D. Zakiryanova, I. V. Korzun, E. G. Vovkotrub, and B. D. Antonov. A Comprehensive Study of the Thermal Behavior of Rare Earth Chloride Hydrates: Resolving Contradictions. *Electrochemical Materials and Technologies*, 3(1):20243028, 2024.

[89] S. Cotton. *Lanthanide and Actinide Chemistry*. John Wiley & Sons, 2024.

[90] G. Friemel, M. Ohl, J. T. Park, B. Keimer, and D. S. Inosov. Coaligning Arrays of Air-Sensitive Single Crystals for Inelastic Neutron Scattering Experiments. In *Journal of Physics: Conference Series*, volume 449. IOP Publishing, 2013.

[91] F. Groitl, D. Graf, J. O. Birk, M. Markó, M. Bartkowiak, U. Filges, C. Niedermayer, C. Rüegg, and H. M. Rønnow. CAMEA—A Novel Multiplexing Analyzer for Neutron Spectroscopy. *Review of Scientific Instruments*, 87(3), 2016.

[92] J. Lass, H. Jacobsen, K. M. L. Krighaar, D. Graf, F. Groitl, F. Herzog, M. Yamada, C. Kägi, R. A. Müller, R. Bürge, and H. M. Rønnow. Commissioning of the Novel Continuous Angle Multi-Energy Analysis Spectrometer at the Paul Scherrer Institut. *Review of Scientific Instruments*, 94(2), 2023.

[93] D. H. Templeton and G. F. Carter. The Crystal Structures of Yttrium Trichloride and Similar Compounds. *The Journal of Physical Chemistry*, 58(11):940–944, 1954.

[94] E. Rastelli, A. Tassi, and L. Reatto. Non-Simple Magnetic Order for Simple Hamiltonians. *Physica B+ C*, 97(1):1–24, 1979.

[95] D. C. Cabra, C. A. Lamas, and H. D. Rosales. Quantum Disordered Phase on the Frustrated Honeycomb Lattice. *Phys. Rev. B*, 83(9):094506, 2011.

[96] A. Scheie, K. Ross, P. P. Stavropoulos, E. Seibel, J. A. Rodriguez-Rivera, J. A. Tang, Y. Li, H.-Y. Kee, R. J. Cava, and C. Broholm. Counterrotating Magnetic Order in the Honeycomb Layers of $NaNi_2BiO_{6-\delta}$. *Physical Review B*, 100(21):214421, 2019.

[97] S. C. Williams, R. D. Johnson, F. Freund, S. Choi, A. Jesche, I. Kimchi, S. Manni, A. Bombardi, P. Manuel, P. Gegenwart, and R. Coldea. Incommensurate Counterrotating Magnetic Order Stabilized by Kitaev Interactions in the Layered Honeycomb α-Li_2IrO_3. *Physical Review B*, 93(19):195158, 2016.

[98] J. Chaloupka, G. Jackeli, and G. Khaliullin. Kitaev-Heisenberg Model on a Honeycomb Lattice: Possible Exotic Phases in Iridium Oxides A_2IrO_3. *Physical Review Letters*, 105(2):027204, 2010.

Appendix A

Custom Instrumentation and Designs

This appendix presents the technical drawings, blueprints, and schematics of all custom-built components developed for this project.

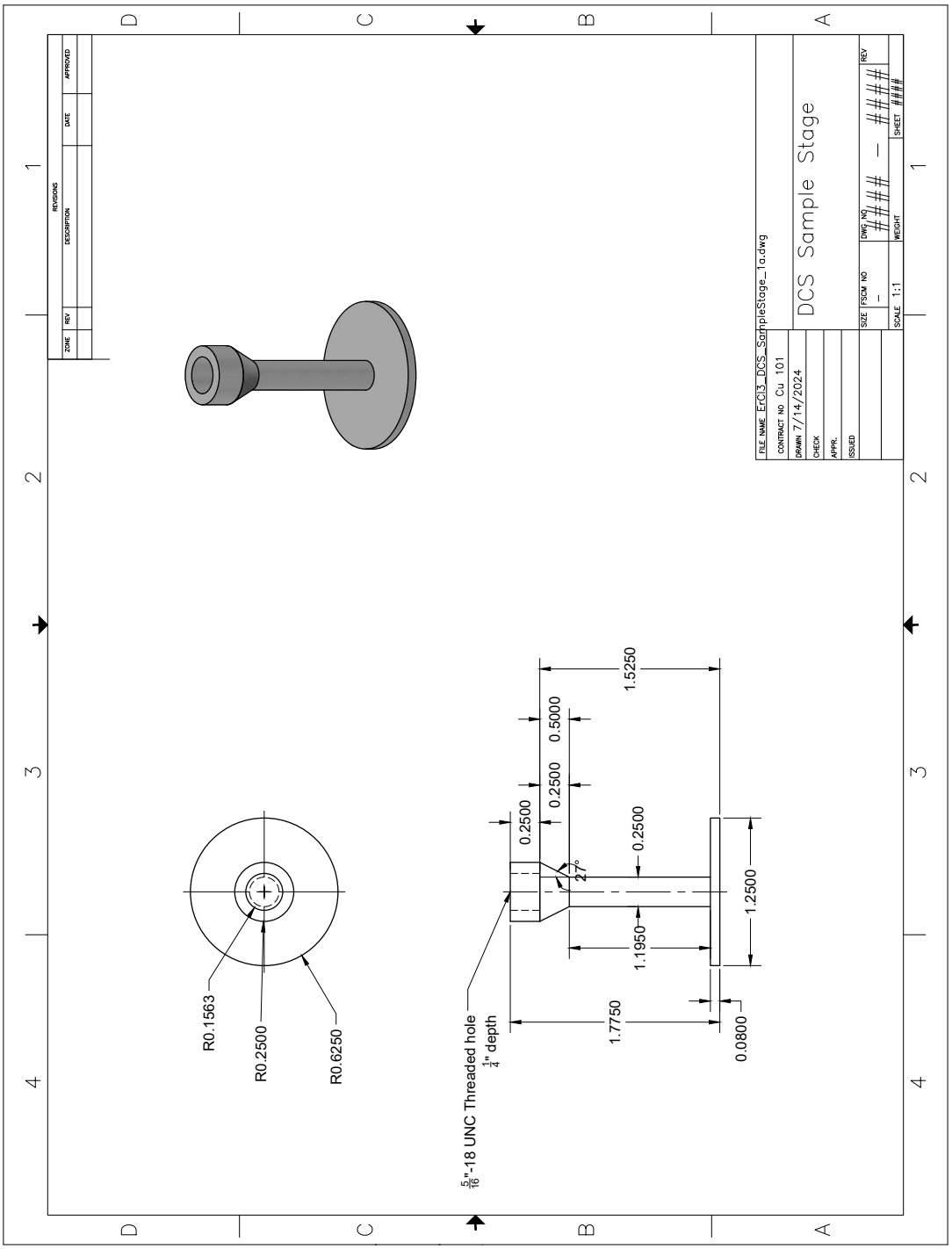

Figure A.1: DCS Sample Stage. Custom designed to integrate with DCS TOF instrument on the NCNR beamline at NIST. Fabricated from Copper 101 (Oxygen-Free). Mates with DCS Stub Blank Flange (Fig. A.2) by sliding into fixed slot. Fixed in place when by DCS Spacer (Fig. A.3) and KF 50 Blank Flange (with window) (Fig. A.9).

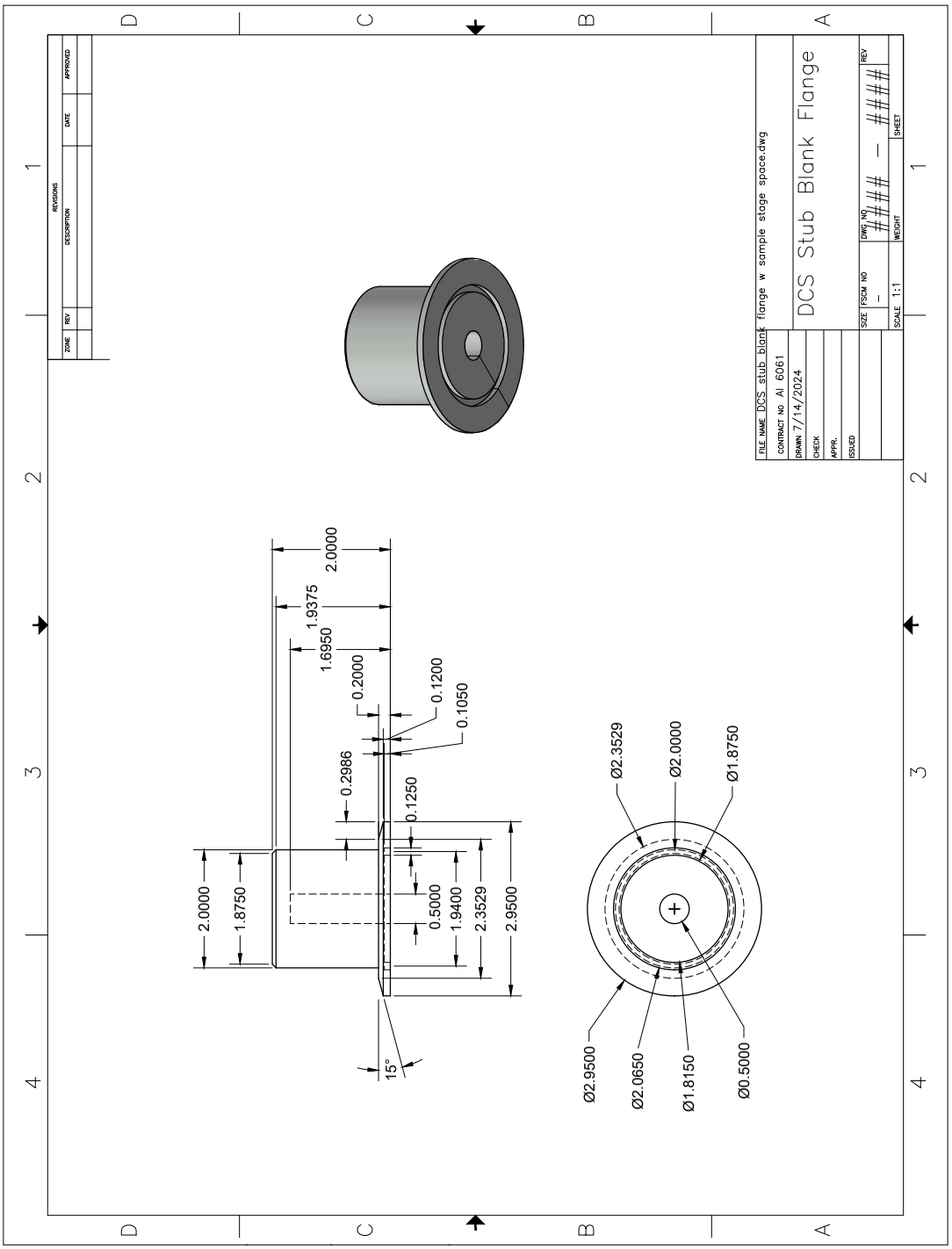

Figure A.2: DCS Stub Blank Flange w/ space for DCS Sample Stage. Fabricated from Aluminum 6061, starting from commercially bought KF50 stub blank flange. Custom designed to house the DCS Sample Stage (Fig. A.1) during air-free Laue orientation.

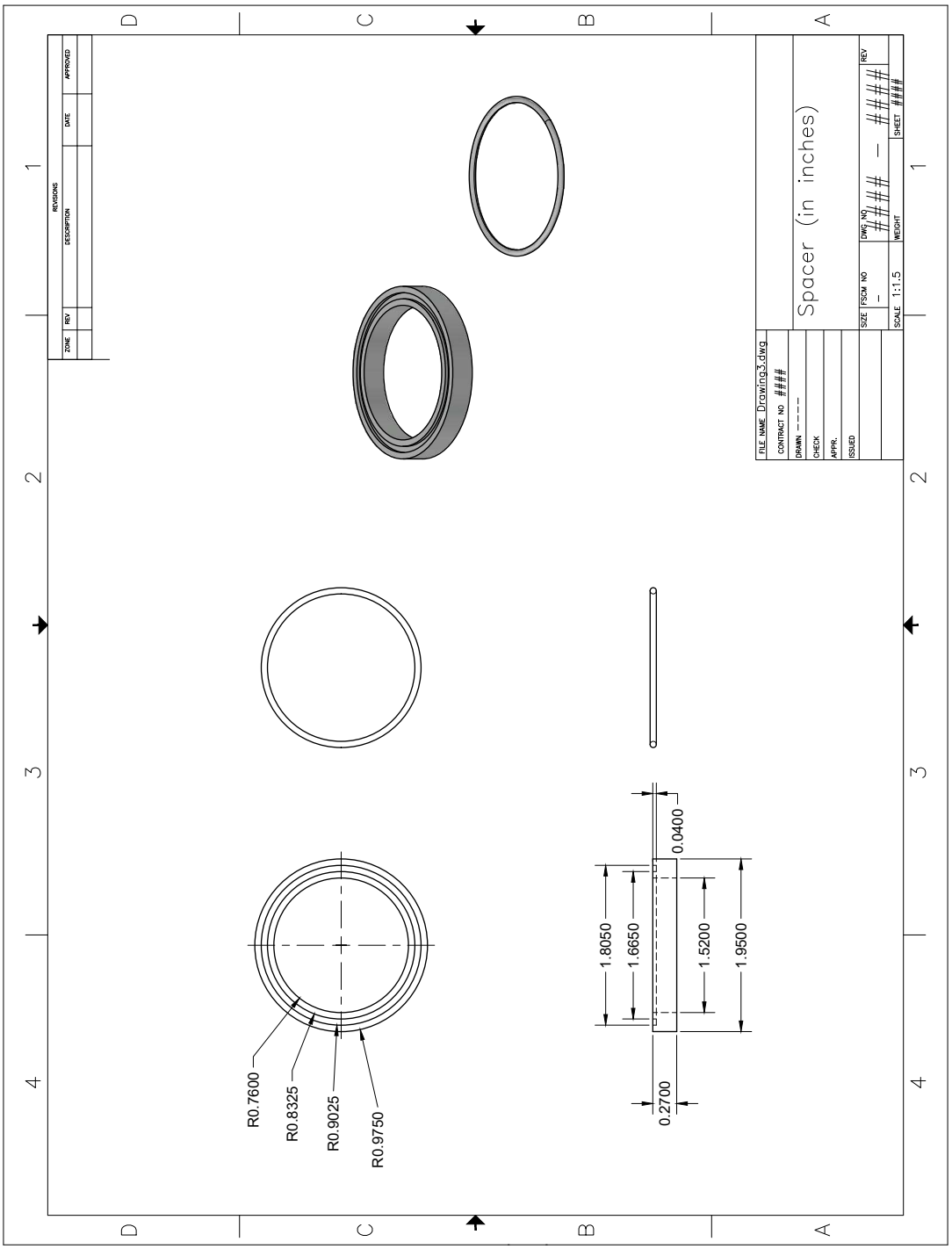

Figure A.3: DCS Spacer. Fabricated from Aluminum 6061. Custom designed to pinch an elastic window between itself, the DCS Sample Stage (Fig. A.1) and the KF 50 Blank Flange (with window) (Fig. A.9) during air-free Laue orientation.

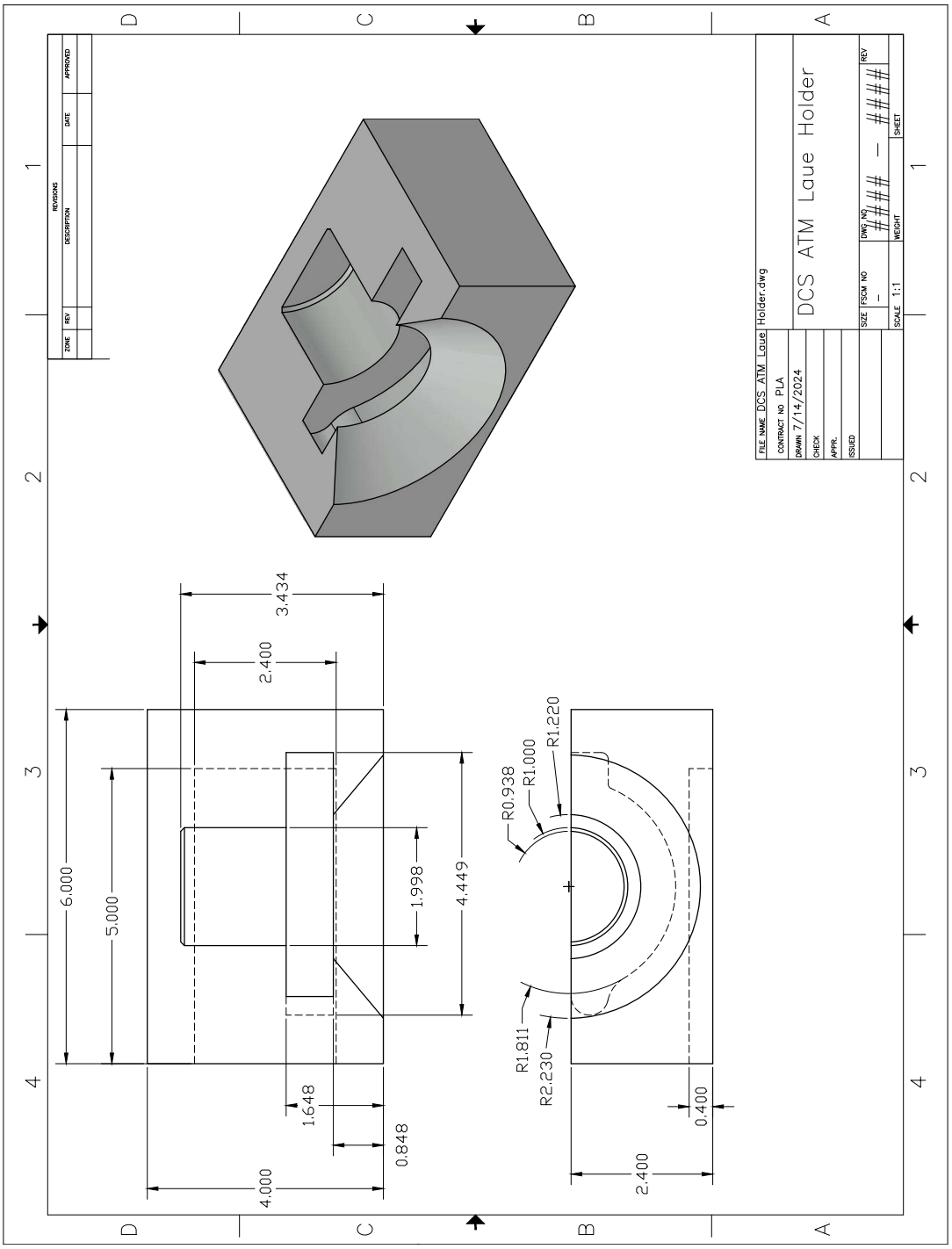

Figure A.4: DCS ATM—Laue Holder. Integrates with three axis goniometer used in Photonic Science Laue X-ray Diffractometer. 3D-Printed in PLA (polylactic acid). Custom designed for the DCS Stub Blank Flange (Fig. A.2), DCS Sample Stage (Fig. A.1), DCS Spacer (Fig. A.3) and KF 50 Blank Flange (with window) (Fig. A.9) combination. Allows for reproducible placement of air-sensitive samples in Laue X-ray cabinet.

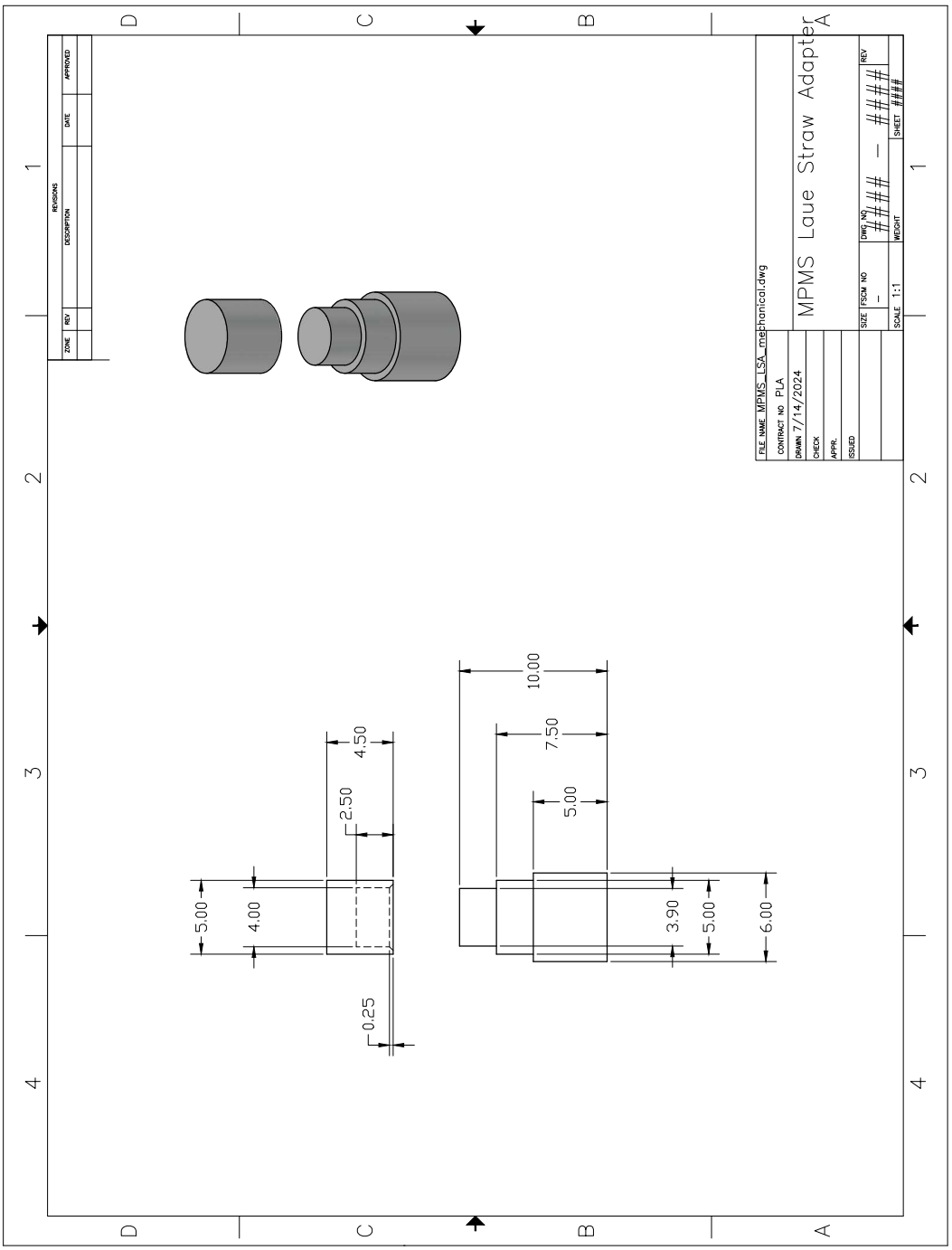

Figure A.5: MPMS3 Laue Straw Adapter (LSA) with Cap. 3D-printed from PLA (polylactic acid). Designed for both the air-free Laue orientation of single crystals and integration into the MPMS3 ^{3}He Option via mating with standard straw. Mates with LSA to ATM adapter (Fig. A.6), which then fits snugly in the DCS Stub Blank Flange (Fig. A.2) to facilitate air-free Laue X-ray orientation of single crystals. Angle of top surface can easily be modified to accommodate any arbitrary crystal orientation within the MPMS3 system.

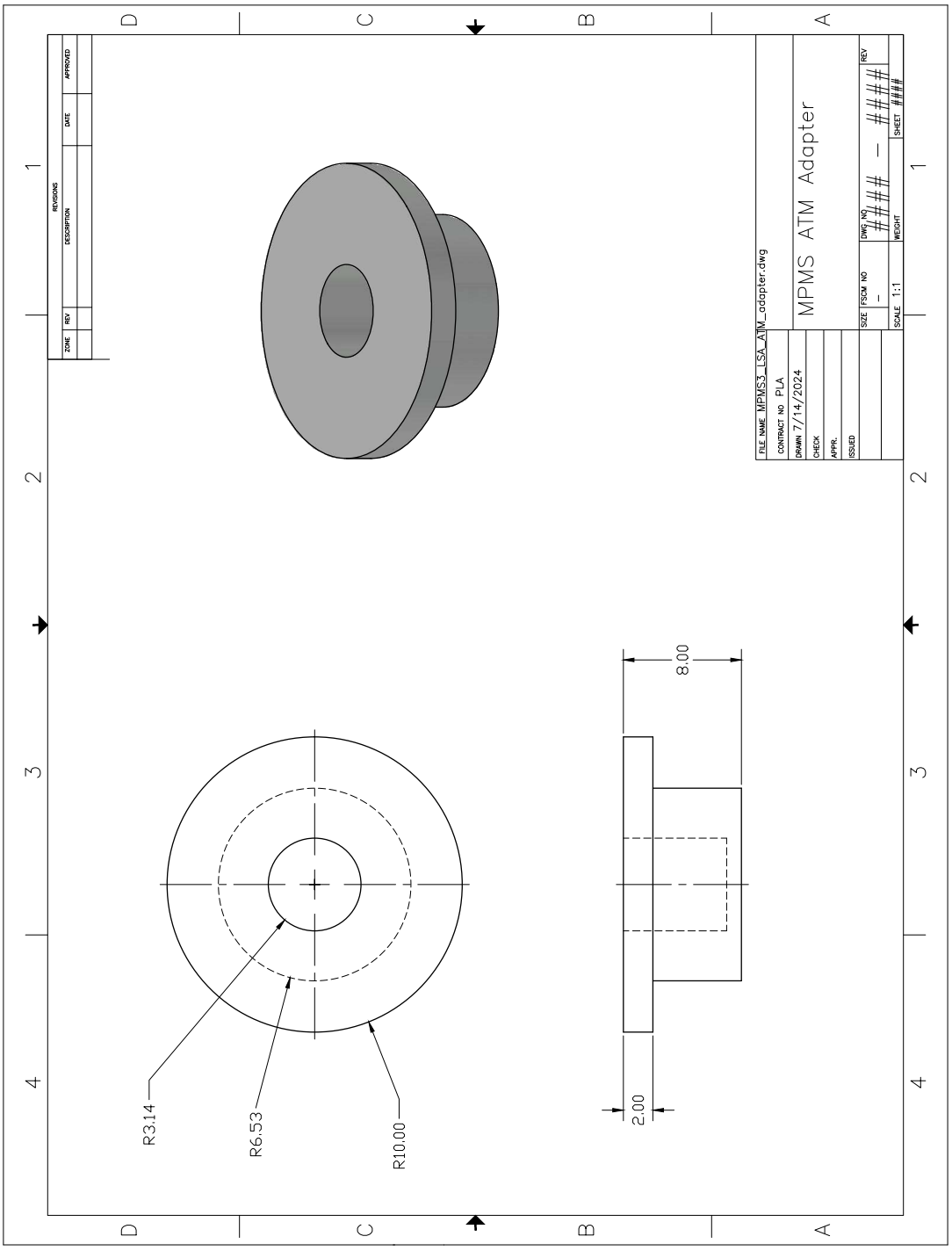

Figure A.6: MPMS3 Laue Straw Adapter (LSA) to Air Tight Module (ATM) adapter. 3D-Printed from PLA (polylactic acid). Designed to mate with the DCS Stub Blank Flange (Fig. A.2) and the MPMS3 LSA (Fig. A.5) to facilitate air-free Laue X-ray orientation of single crystals.

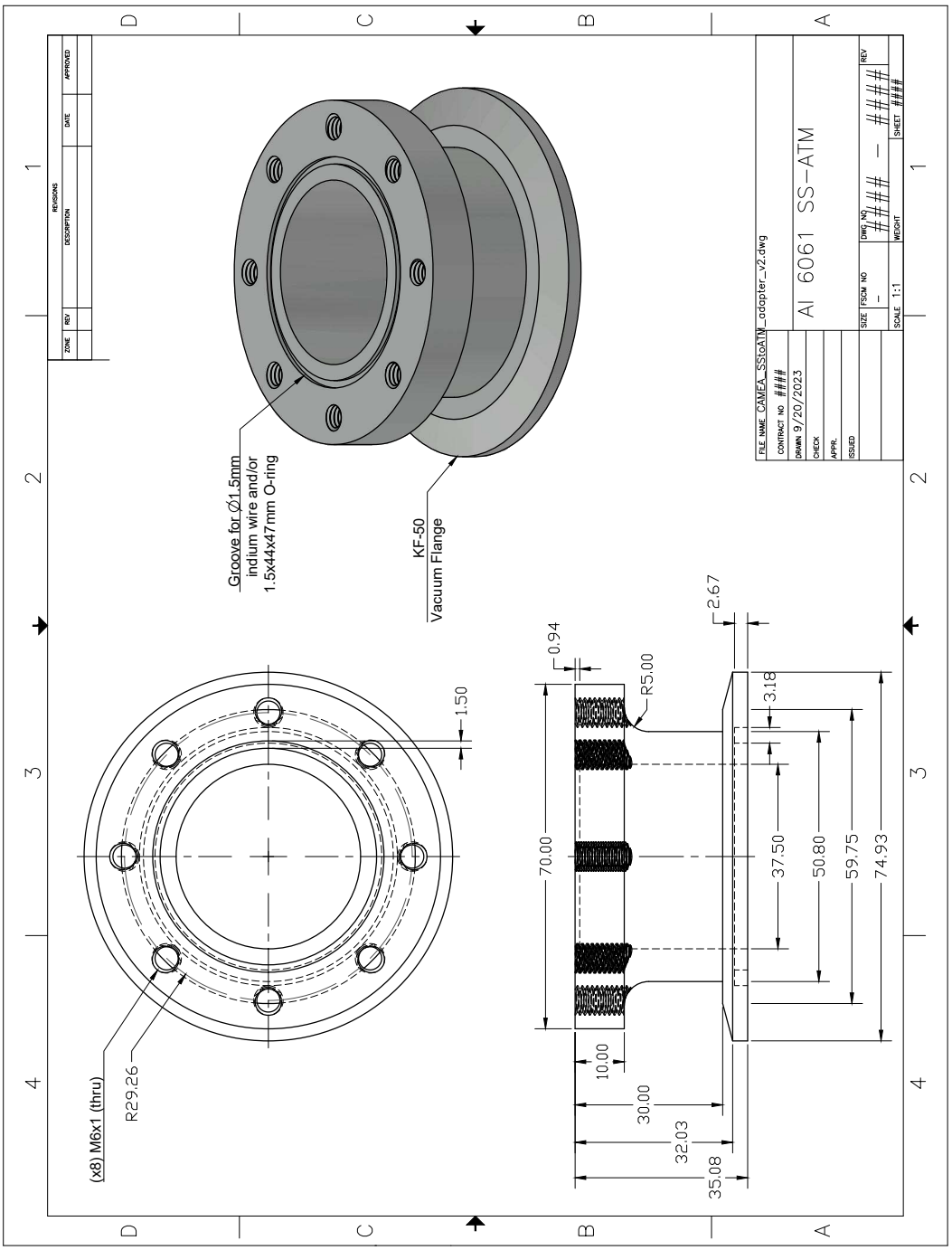

Figure A.7: Part 1/5: CAMEA ATM—Sample Stage to ATM adapter. Blueprint of custom adaptor designed to work with standard KF50 clamps and custom sample stage used for collecting Laue images of air-sensitive crystals. On one side, this part utilizes eight M6x1 screws and ∅1.5mm indium wire, or 1.5×44×47mm O-ring, to mate with the custom CAMEA sample stage Fig. A.8. The other side utilizes standard KF50 clamps to mate with the KF50 Blank Flange with removed window (Fig. A.9) to secure a transparent elastic film.

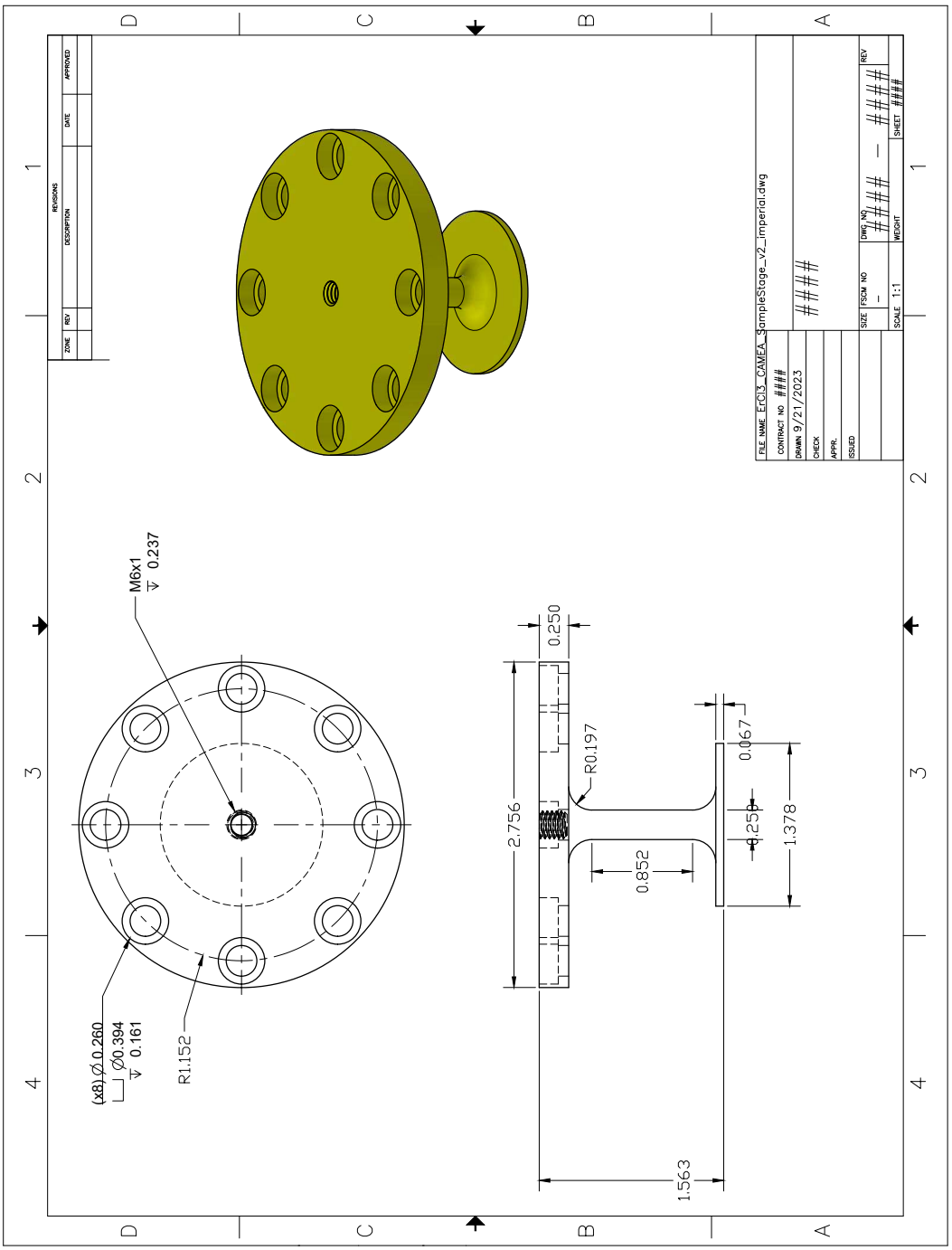

Figure A.8: Part 2/5: CAMEA ATM—Sample Stage. Blueprint of custom designed sample stage used for the $ErCl_3$ CAMEA experiment. Mates with Part 1/5: CAMEA ATM—Sample Stage to ATM adapter (Fig. A.7). Used to mount and co-align single crystals of $ErCl_3$ for the CAMEA experiment. This part could be directly exchanged to mount with either Part 4/5: CAMEA ATM—Clear Transportation Module (Fig. A.10) or Part 5/5: CAMEA ATM—Copper Can (Fig. A.11).

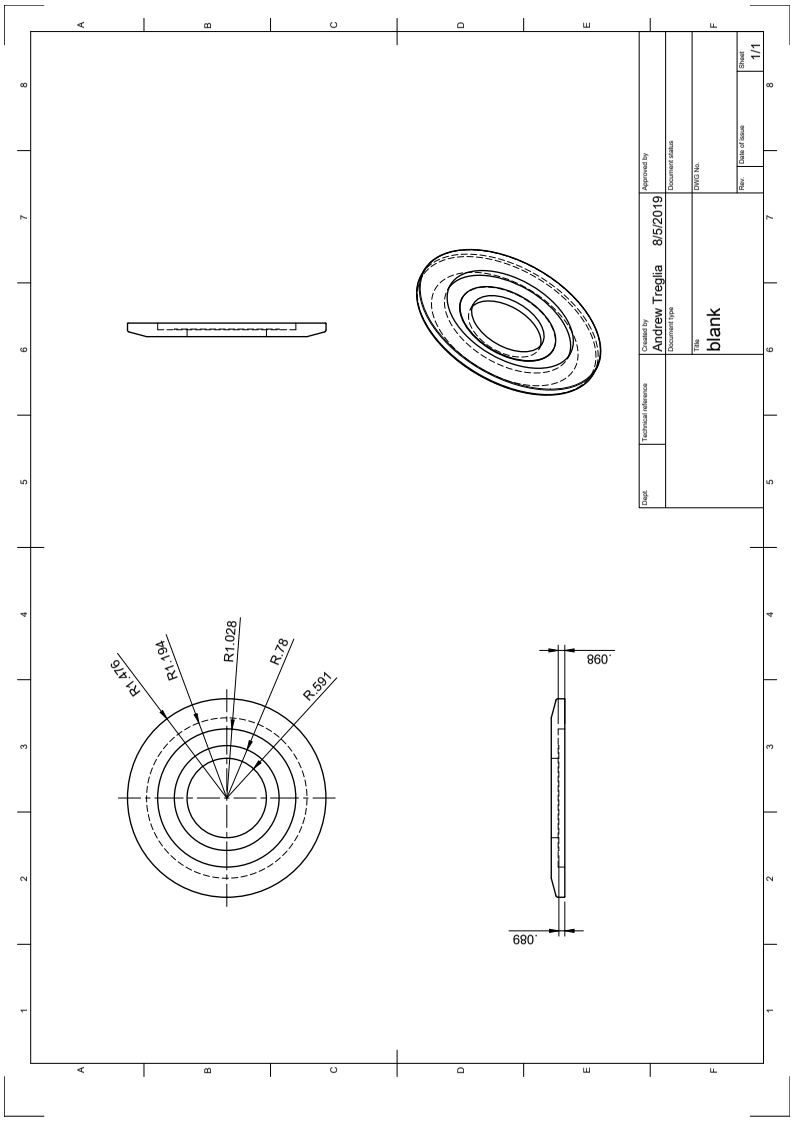

Figure A.9: Part 3/5: CAMEA ATM—KF50 Blank Flange. Blueprint of custom KF50 Blank Flange with removed window. Mates with Part 1/5: CAMEA ATM—Sample Stage to ATM adapter (Fig. A.7) via standard KF50 clamp. This is a modification of a standard KF50 Blank Flange with a window removed to allow a transparent elastic film to be secured for air-free Laue imaging and sample reorientation.

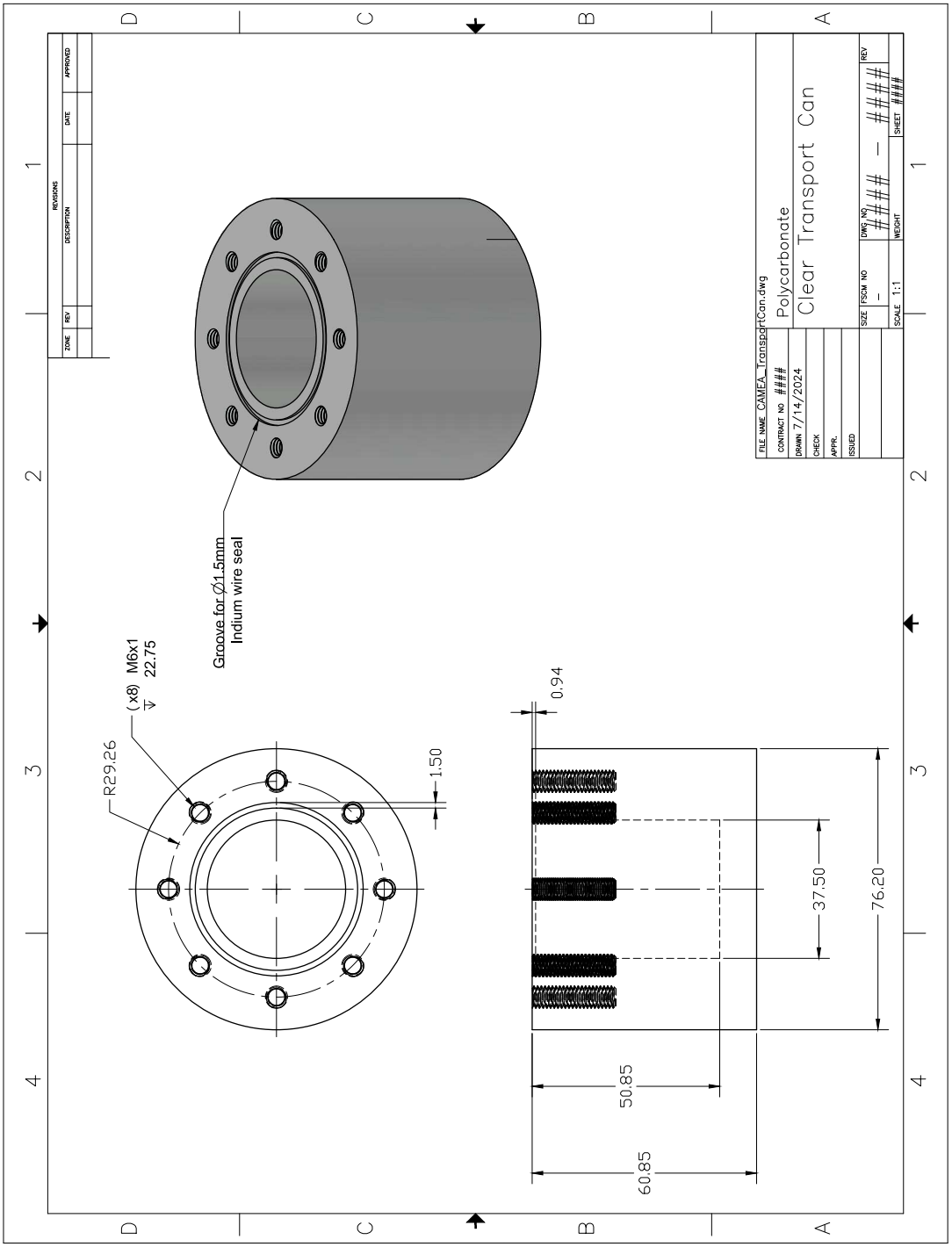

Figure A.10: Part 4/5: CAMEA ATM—Clear Transportation Module. Blueprint of custom transportation module. Mates with Part 1/5: CAMEA ATM—Sample Stage to ATM adapter (Fig. A.7) via 8 M6×1 screws. This is a custom design fabricated from polycorbonate and polished clear to facilitate a safe, air-free, international customs "proof" container for transport of aligned samples through airport security.

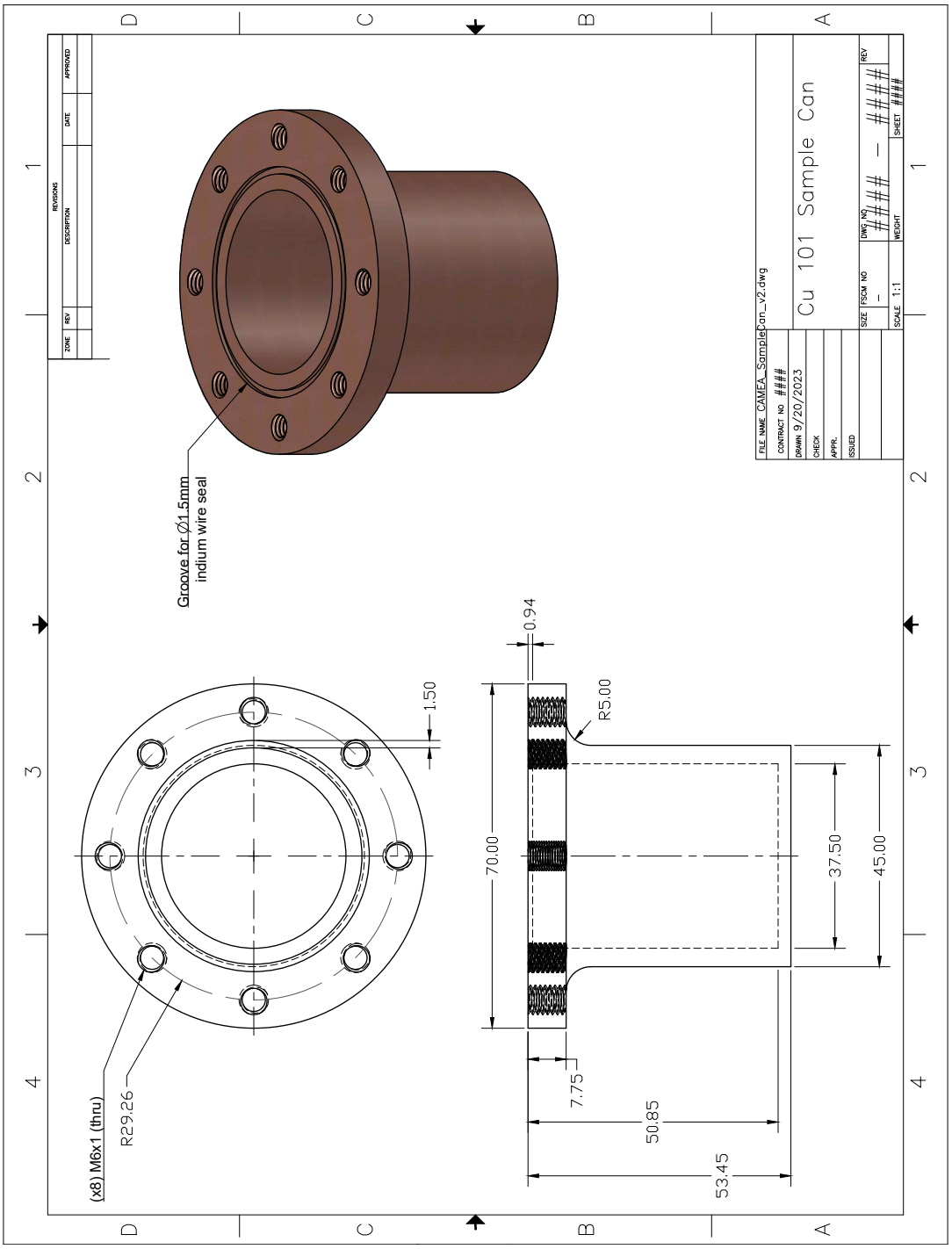

Figure A.11: Part 5/5: CAMEA ATM—Copper Sample Can. Blueprint of custom Copper can. Mates with Part 1/5: CAMEA ATM—Sample Stage to ATM adapter (Fig. A.7) via eight M6×16 screws and ∅1.5mm indium wire, or 1.5×44×47mm O-ring. This is a custom design fabricated from Copper-101 (oxygen-free) for the use of the CAMEA experiment, in accordance with CAMEA specs and constraints.

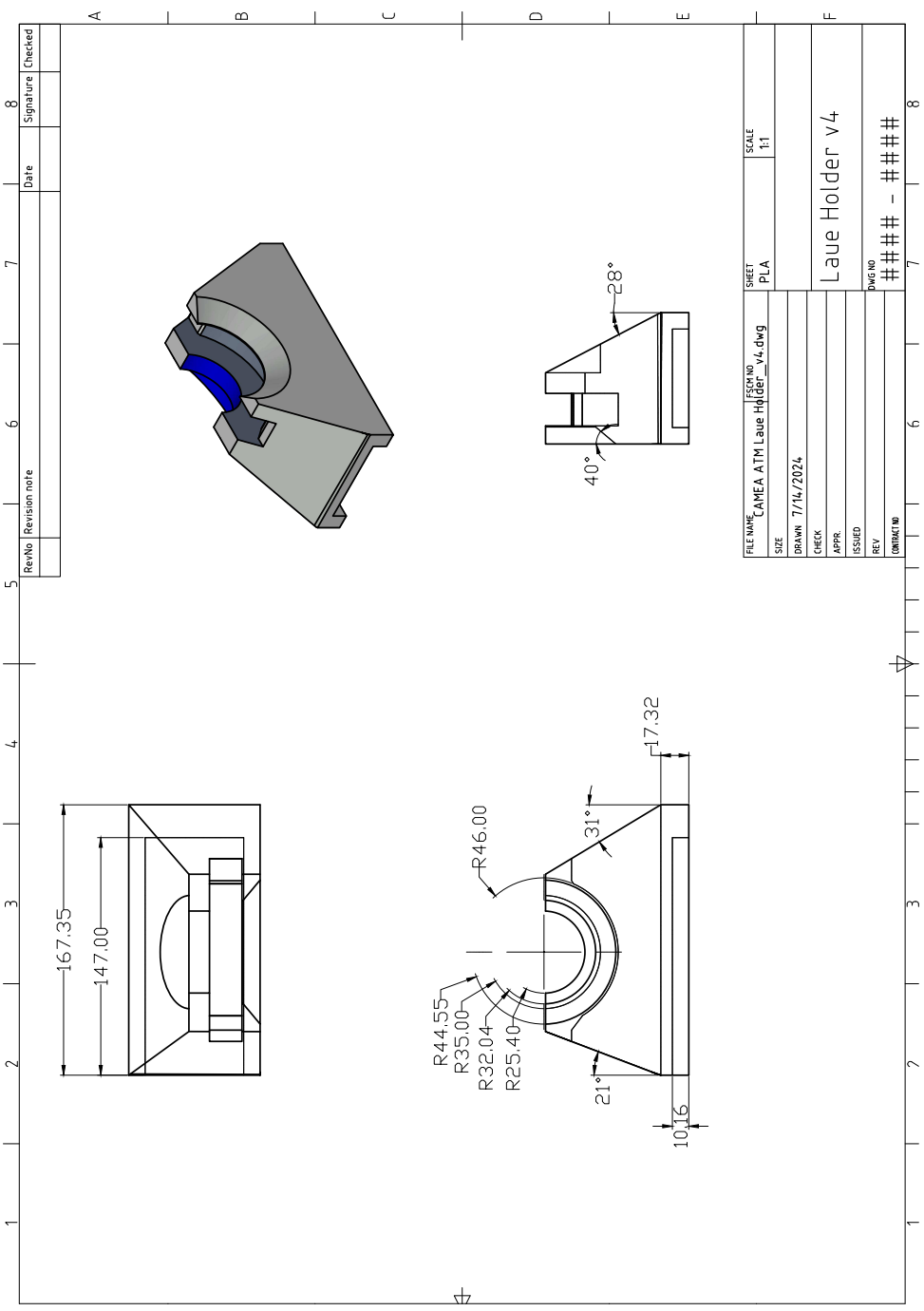

Figure A.12: CAMEA ATM—Laue Holder v4. Integrates with three axis goniometer used in Photonic Science Laue X-ray Diffractometer. 3D-Printed in PLA (polylactic acid). Custom designed for the CAMEA ATM—Sample Stage to ATM adapter (Fig. A.7) and CAMEA ATM—Sample Stage (Fig. A.8) combination. Allows for reproducible placement of air-sensitive samples in Laue X-ray cabinet.